

# Simulation and Design of Traveling-Wave Tubes with Folded-Waveguide Delay Lines

Vom Promotionsausschuss der  
Technischen Universität Hamburg-Harburg  
zur Erlangung des akademischen Grades  
Doktor-Ingenieur (Dr.-Ing.)

genehmigte Dissertation

von  
SASCHA MEYNE

aus  
Dannenberg (Elbe)

**2016**

First Examiner: Prof. Dr.-Ing. Arne F. Jacob  
Second Examiner: Prof. Dr.-Ing. John Jelonnek  
Chair of Examination Board: Prof. Dr.-Ing. Gerhard Bauch  
  
Date of Thesis Defense: November 26<sup>th</sup>, 2016

# Acknowledgment

This work would not have been possible without the support of many people and I would like to take the opportunity to thank them. First of all, I thank Prof. Dr.-Ing. Arne F. Jacob for giving me the opportunity to work on a very interesting and challenging topic at his institute and for his trust in my abilities. I also thank Prof. Dr.-Ing. John Jelonnek for the preparation of the second expertise and Prof. Dr.-Ing. Gerhard Bauch for chairing the examination committee.

This work was performed in collaboration with the French company Thales. I would like to thank Dr.-Ing. Philip Birtel for his professional and organizational support during my thesis. I would like to express my sincerest thanks to Monsieur Jean-François David who was my mentor regarding vacuum electronics. Additionally, I extend my thanks to him and his family for cordially inviting me into their home during my business trips to the French Thales site in Vélizy. I also thank Dr. Siegfried Voigt from the DLR Space Administration for the smooth organization of the research project that served as the foundation of my thesis.

I would like to thank my colleague and former student Djamschid Safi for supporting me in my research and for thoroughly proofreading my thesis. Furthermore, I wish to thank my other bachelor and master students Markus Krenz and Moritz Hägermann who contributed to my work. Many thanks also to my colleagues at the Institute of High Frequency Technology for the pleasant working atmosphere and for the support in day-to-day routine.

Special thanks go to my wife Nora who supported and encouraged me above all. Last but not least, I would like to thank my parents who made my studies possible in the first place and who encouraged me to do whatever I liked.

# Contents

<b>1</b>	<b>Introduction</b>	<b>1</b>
1.1	Folded-Waveguide Traveling-Wave Tubes . . . . .	1
1.2	Outline of the Thesis . . . . .	2
<b>2</b>	<b>Basics of Traveling-Wave Tubes</b>	<b>3</b>
2.1	Components of Traveling-Wave Tubes . . . . .	3
2.1.1	Electron Gun . . . . .	3
2.1.2	Magnetic Focusing . . . . .	4
2.1.3	Delay Line . . . . .	5
2.1.4	Collector . . . . .	8
2.2	Pierce Theory . . . . .	8
2.2.1	Circuit Equations . . . . .	9
2.2.2	Space-Charge Waves on Electron Beams . . . . .	10
2.2.3	Interaction . . . . .	11
2.3	Nonlinear Interaction . . . . .	13
2.4	The Software Package <i>KlysTOP</i> . . . . .	14
<b>3</b>	<b>Folded-Waveguide Delay Lines</b>	<b>15</b>
3.1	General Topology . . . . .	16
3.2	Eigenmode Simulation . . . . .	16
3.2.1	Characterization . . . . .	18
3.2.2	Parameter Studies . . . . .	19
3.3	Equivalent Circuit Representation . . . . .	27
3.3.1	Dispersion of the Equivalent Circuit Model . . . . .	29
3.3.2	Abstract Coupler and Sever Model . . . . .	30
3.3.3	Nonlinear Curve Fitting . . . . .	31
3.3.4	Correction of Electric Field Shape . . . . .	34
3.3.5	Synthesis of Electric Field Shape . . . . .	37
3.4	Fabrication and Characterization of Folded-Waveguide Delay Lines	39
3.4.1	Fabrication . . . . .	40
3.4.2	Resonant Measurement . . . . .	42
3.4.3	Measurement of Complex Propagation Constant . . . . .	44

## Contents

<b>4</b>	<b>Matching for Cold and Hot Operation</b>	<b>48</b>
4.1	Dispersion of the Coupled System . . . . .	48
4.2	Influence of Matching for Hot Operation . . . . .	51
4.2.1	Stability . . . . .	52
4.2.2	Large-Signal Behavior . . . . .	54
4.3	Sever Topology for Hot Operation . . . . .	55
<b>5</b>	<b>General Interaction Simulation</b>	<b>59</b>
5.1	Nonlinear Multidimensional Root Problem . . . . .	59
5.2	Formulation of <i>KlysTOP</i> Algorithm . . . . .	60
5.3	Newton-Raphson Method . . . . .	61
5.4	Broyden's (Good) Method . . . . .	61
5.5	Initialization Procedures . . . . .	62
5.5.1	Unity Initialization . . . . .	62
5.5.2	Initialization from Small-Signal Model . . . . .	63
5.5.3	Initialization from Large-Signal Computation . . . . .	63
5.6	Convergence Analysis . . . . .	63
5.6.1	Small-Signal Convergence . . . . .	65
5.6.2	Large-Signal Convergence . . . . .	67
5.7	Space-Charge Iterations . . . . .	72
<b>6</b>	<b>Folded-Waveguide Interaction Simulation</b>	<b>75</b>
6.1	Interaction Convergence . . . . .	76
6.2	Comparison of Interaction Results . . . . .	79
<b>7</b>	<b>Conclusion</b>	<b>81</b>

# List of Acronyms

<b>1D, 2D, 2.5D, 3D</b>	One-, two-, two-and-a-half-, three-dimensional
<b>B-FW</b>	Basic folded waveguide
<b>BBM</b>	Broyden's bad method
<b>BGM</b>	Broyden's good method
<b>CC</b>	Coupled cavity
<b>CC-TWT</b>	Coupled-cavity traveling-wave tube
<b>DC</b>	Direct current
<b>EC</b>	Equivalent circuit
<b>EDM</b>	Electrical discharge machining
<b>EM</b>	Electromagnetic
<b>FW</b>	Folded waveguide
<b>FW-TWT</b>	Folded-waveguide traveling-wave tube
<b>MVED</b>	Microwave vacuum electronic device
<b>NC-FW</b>	Nose-cone loaded folded waveguide
<b>PEC</b>	Perfect electric conductor
<b>PIC</b>	Particle in cell
<b>PPM</b>	Periodic permanent magnet
<b>Radar</b>	Radio detection and ranging
<b>RF</b>	Radio frequency
<b>RMS</b>	Root mean square
<b>RW</b>	Rectangular waveguide
<b>SSE</b>	Solid-state electronics
<b>SW</b>	Serpentine waveguide
<b>TL</b>	Transmission line
<b>TWT</b>	Traveling-wave tube
<b>VNA</b>	Vector network analyzer

# 1 Introduction

Microwave vacuum electronic devices (MVEDs) are highly efficient network elements for radio frequency (RF) applications. A modulated flow of electrons amplifies, modifies, or induces electromagnetic (EM) energy to achieve a specific functionality. MVEDs are inherently more efficient compared to solid-state electronics (SSE), because electrons propagate through vacuum in place of bulk material.

Especially in radar and space applications MVEDs are the dominant technology. High-power capabilities as well as high reliability and resilience against radiation and temperature variation make them difficult to replace, especially at high frequencies [1].

## 1.1 Folded-Waveguide Traveling-Wave Tubes

Traveling-wave tubes (TWTs) are widely used power amplifiers for the above mentioned applications. Electrons are emitted from a heated cathode, focused to a beam of cylindrical shape, and injected into the interaction area. An RF delay line guiding an EM wave establishes interaction with the electron beam by synchronizing the phase velocity of the wave to the electron velocity. The electron beam then becomes modulated with the incoming RF operating frequency and forms bunches. The electron beam in turn induces a wave at the same frequency on the delay line, thus leading to exponential growth of the RF signal. When the wave is coupled out, the spent electron beam enters a collector with one or multiple stages where the electrons are decelerated and finally hit the electrodes converting their residual energy into heat. The voltages of the collector stages largely affect the efficiency of the amplifier. The concept of voltage-depressed collectors is one of the major advantages of vacuum over solid-state devices.

Different delay line concepts have been used in the past [2]. While the helical delay line excels at broadband applications, it is limited in output power since it is galvanically disconnected from the outer hull. Because of that, effective heat removal concepts are difficult to realize. Coupled-cavity (CC) delay lines, on the other hand, are narrowband but generally achieve much higher output powers since they are made of bulk metal.

Moving to higher frequencies requires to reduce characteristic geometric parameters, thus increasing the probability of intercepted electrons with ensuing heat

development. The increased RF loss at higher frequencies additionally leads to undesired heat. Therefore, bulk-metal delay lines are favorable in terms of thermal management. However, a large bandwidth is also desirable. A trade-off solution is the folded-waveguide (FW) delay line [3]. FW delay lines are currently under investigation for radiation sources above K-band due to their ease of fabrication and potential high-power capabilities [4–10]. Aside from many advantages, this type of delay line suffers from relatively weak interaction with the electron beam, thus limiting the amplification per unit length and the maximum achievable efficiency.

As the fabrication of TWTs is very time consuming and costly, it is desirable to predict a tube’s performance prior to its assembly. However, modeling the beam-wave interaction in a TWT is very complex. It involves the simultaneous solution of Maxwell’s and Poisson’s equations as well as of the 3D Lorentz force equation for the electron motion subject to external EM fields. Certain assumptions can simplify the calculation, but under large-signal excitation the electron beam can to this day only be modeled by tracking the electron paths through the interaction area. This is a very time- and computation-intensive process. The efficient modeling and numerical calculation of the beam-wave interaction is investigated in current research.

## 1.2 Outline of the Thesis

The main topics of this thesis are the design, modeling, and efficient interaction simulation of FW-TWTs. Structural variations are analyzed to mitigate some of the drawbacks inherent to conventional FW structures. Delay lines featuring these concepts are then realized and their feasibility is assessed by measuring their cold characteristics, i.e., without electron beam. Proper models are implemented into an existing beam-wave interaction software to predict the performance of amplifiers with FW delay lines. As those devices are electrically longer compared to other established TWTs, the interaction simulation is computationally more demanding. New algorithms are therefore implemented and tested to make the computations more efficient.

This thesis is organized as follows. Chapter 2 summarizes the necessary fundamentals of TWTs. Chapter 3 then focuses on FW delay lines and how they can be characterized and modeled. Additionally, the fabrication and cold measurements of a modified FW delay line are briefly outlined and discussed. The difference between a delay line under cold, i.e., without an electron beam, and hot operating conditions, i.e., one interacting with an electron beam, is analyzed in Chapter 4. An algorithmic concept to accelerate the beam-wave interaction prediction is proposed in Chapter 5. The thesis ends with the interaction simulation of an optimized FW-TWT and the verification of the previously presented models.

# 2 Basics of Traveling-Wave Tubes

## 2.1 Components of Traveling-Wave Tubes

The main components of a TWT will be described briefly in the order in which the electrons pass through the tube, i.e., from emission in the cathode to absorption in the collector. A schematic of a generic FW-TWT in Figure 2.1 serves as an overview.

### 2.1.1 Electron Gun

The generation of free electrons is achieved by means of an electron gun at the beginning of the tube (yellow area in Figure 2.1). A more detailed view of an electron gun is depicted in Figure 2.2. The electron gun is used to generate an electron beam of adequate power and lateral extension. A cathode of near-spherical surface provides electrons through thermal or field emission [11]. The capability of the cathode to emit electrons is limited by the cathode material. Therefore, the cathode radius has to be several times larger than the desired beam radius in order to achieve a sufficiently large beam current as well as a long lifetime of the cathode [1]. A high voltage  $V_0$  at the anode accelerates the electrons after they have been emitted from the cathode surface. They converge to a pencil-shaped beam and enter the magnetic field of the focusing system.

The electron beam provides the energy source for the amplification process. Its resilience against perturbations is very important for the performance and tunability

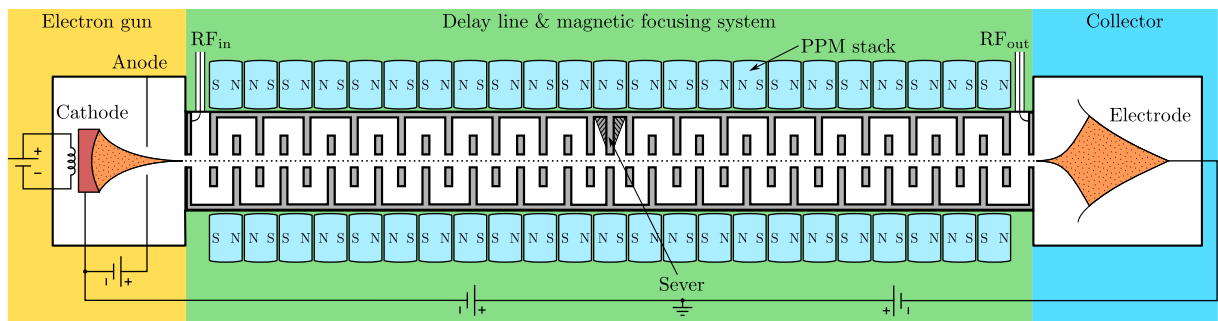


Figure 2.1: Schematic of a generic folded-waveguide traveling-wave tube with two sections.

## 2 Basics of Traveling-Wave Tubes

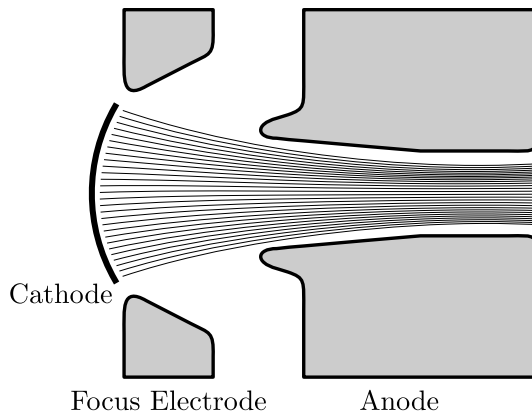


Figure 2.2: Electron gun with trajectories indicated.

of the vacuum tube. The DC beam current  $I_0$  and accelerating voltage  $V_0$  limit the maximum achievable output power of the TWT. The beam efficiency is calculated from

$$\eta_{\text{beam}} = \frac{P_{\text{out}}}{V_0 I_0}, \quad (2.1)$$

where  $P_{\text{out}}$  is the achieved RF output power.  $\eta_{\text{beam}}$  cannot be arbitrarily large, because electrons would otherwise be modulated so strongly that the magnetic focusing field is not sufficient any more. As a result the electron beam would break apart, leading to undesired intercepted electrons. Another limiting effect is the maximum axial electric field generated by the delay line. It has to be large enough to keep the bunches from dispersing due to space-charge forces. Therefore, the delay line topology inherently limits the maximum achievable  $\eta_{\text{beam}}$ .

### 2.1.2 Magnetic Focusing

As mentioned in the previous section, the electrons are focused by an externally applied magnetic field. Otherwise the beam would diverge due to the space-charge forces of the electrons. A constant axial magnetic field prevents the beam from diverging [11]. Considering the movement vector of an electron subjected to a constant magnetic field, it follows that a rotational movement is necessary for the electrons to be focused. The electron trajectories are therefore best described by helical paths.

The constant magnetic field can be provided by a solenoid. However, the magnetic field then strongly interacts with other components in the vicinity of the tube. The external magnetic field can be suppressed by shielding the device magnetically. This is often not an option, because it adds a lot of weight and volume to the device. This aspect is especially important for satellite communication where low weight is crucial.

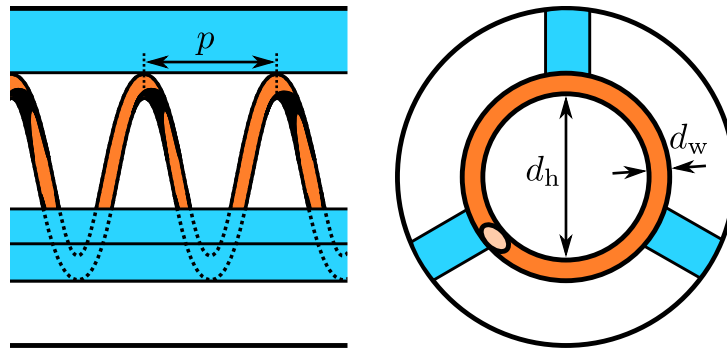


Figure 2.3: A round-wire helix. Support rods are indicated in blue.

A more light-weight solution for magnetic focusing is a periodic permanent magnet (PPM) configuration. Figure 2.1 indicates such a configuration in the area shaded in green. Annular permanent magnets are arranged in alternating polarity to set up a spatially varying magnetic field. If the period of the magnetic field is sufficiently short, the electrons effectively experience a constant magnetic field, the magnitude of which is equal to the root mean square (RMS) of the PPM field.

### 2.1.3 Delay Line

The delay line mainly dictates the RF performance by its inherent bandwidth and coupling strength to the electron beam. The area in green in Figure 2.1 contains the interaction space with the actual delay line. The energy exchange between the electrons and the RF signal relies on the interaction of those two, and thus depends on how strongly they are coupled. Additionally, both need to have approximately the same axial (phase) velocity. Figuratively, the electrons have to experience the same phase of the EM wave along the delay line such that they are continuously subjected to the same RF field. Since EM waves in conventional waveguides have phase velocities in the order of the speed of light  $c_0$ , or even larger, they must be slowed down to ensure synchronous operation. The electron velocity  $v_e$  depends on  $V_0$  and typically lies in the range of  $v_e/c_0 \approx 0.1 \dots 0.4$  depending on the application. In the following three typical delay line topologies are briefly described.

#### Helix

The helical delay line is a flat or round wire wound around the electron beam axis. Figure 2.3 shows a principle drawing of a round-wire helix. The delay of an EM wave is determined by the pitch  $p$  and inner diameter  $d_h$  of the helix [11]. The latter is fixed in the vacuum tube by means of dielectric support rods. The helix has poor thermal properties, because the dielectric rods have a low thermal conductivity compared to metal. Additionally, the areas of contact between helix and rods, as

## 2 Basics of Traveling-Wave Tubes

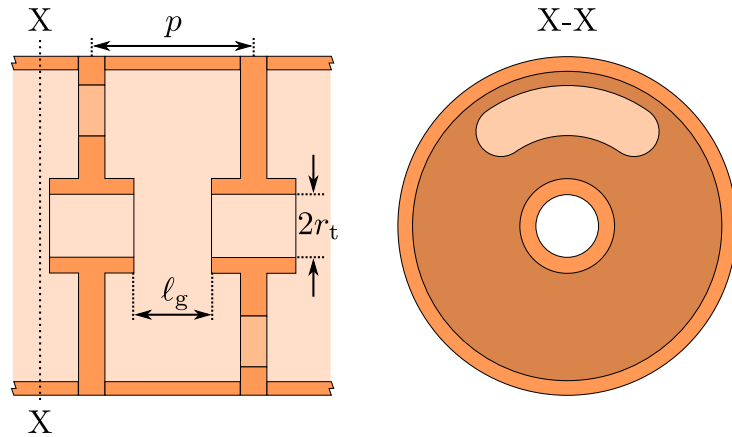


Figure 2.4: Longitudinal and cross section of a typical coupled-cavity delay line.

well as between rods and metal hull, significantly increase the thermal resistance. Intercepted electrons and RF losses along the delay line lead to heat that needs to be removed in order to avoid integral damage to the device.

The helix is a very broadband delay line on which propagation down to DC is possible. Helices are often used in medium-power applications such as telecommunications, both on the ground and in space, and they exhibit relative bandwidths of up to more than two octaves for low-power tubes [11]. Most TWTs used in communication applications achieve usable bandwidths of about 20%, but at a comparatively much larger output power [12].

### Coupled Cavities

A typical CC delay line is depicted in Figure 2.4. The electron beam propagates inside an electron beam tunnel of radius  $r_t$  and interacts with the EM fields inside the cavities at gaps of length  $l_g$ . The EM wave, on the other hand, propagates via coupling slots in the cavity walls from one cavity to the next. Figuratively, the EM wave is slowed down by the CC delay line, because the fields inside the cavity have to build up before they can couple to the next cavity. CC delay lines are much more narrowband than helices. They operate in the vicinity of the resonant frequency of the closed individual cavity. Typical cold bandwidths are around 15% to 25%. This type of delay line consists of bulk metal and thus has much larger thermal conductivity. It is typically used in high-power applications such as Radar (radio detection and ranging).

### Folded/Serpentine Waveguide

An exemplary serpentine waveguide (SW) is depicted in Figure 2.5. It consists of a rectangular waveguide wound in a meander-like manner about the electron

## 2 Basics of Traveling-Wave Tubes

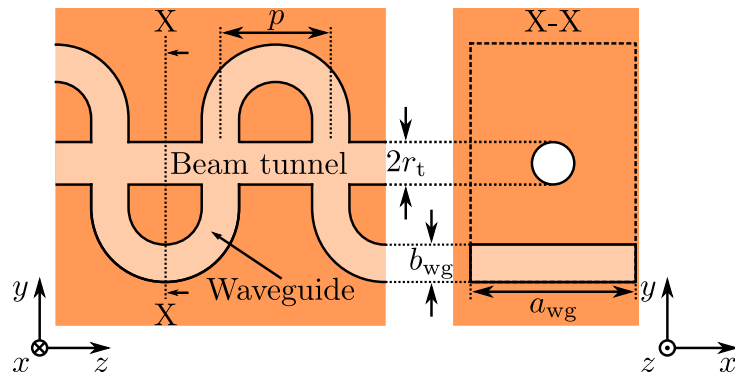


Figure 2.5: Longitudinal and cross section of a serpentine-waveguide delay line.

beam axis. The waveguide is operated at the fundamental  $H_{10}$ -mode such that the electron beam interacts with the transverse E-field of that mode. In contrast to an SW, a folded waveguide (FW) has  $90^\circ$  corners. Both SW and FW delay lines are more broadband than their CC counterparts, but far less than helices. However, since they can be easily manufactured from bulk metal, they have power handling capabilities similar to CC lines [3]. Therefore, they are currently under strong investigation for TWT amplifiers above  $K_a$ -band, and even in the sub-THz range [13, 14].

### Additional Delay Line Components

Each of the above mentioned delay lines needs two additional components in order to function in a TWT. The first important item are couplers necessary to inject (extract) EM energy into (from) the delay line. An ideal coupler transmits all incoming power to the connected device at all frequencies.

This is, of course, not realizable and therefore couplers introduce reflections. Oscillations may occur due to the gain of the tube, if the reflected signals between such discontinuities superpose constructively. To reduce the loop gain, and thus the danger of so-called TWT oscillations, the reflections of couplers should be as low as possible. Additionally, the tube can be subdivided into multiple sections, thus lowering the requirements for the couplers. This is achieved by introducing severs which are strongly attenuating elements sometimes combined with an actual disruption of the delay line [11]. Severs generally exhibit lower reflections than couplers. They are therefore a good means to suppress oscillations in high-gain devices.

### 2.1.4 Collector

After the interaction region the bunched electron beam enters the collector which is indicated by the blue area in Figure 2.1. The magnetic focusing is progressively reduced such that the beam begins to diverge. The collector consists of one or more electrodes with potentials lower than the accelerating voltage. This way the electrons are decelerated. They are collected in groups by different electrodes depending on the collector potentials and the electron velocities. Ideally, the electrons hit the electrodes with no residual velocity. This is not the case for a real collector, and therefore the electrons hit the respective electrodes with finite kinetic energy which is then converted into heat. A well-designed collector has stage voltages covering most of the electron velocity spectrum and thus minimizes the amount of generated heat. The voltages of the collector stages reduce the net power supplied to the tube [11, p. 398]. The possibility to employ collectors is one of the main advantages of MVEDs over SSE, since these components greatly increase the overall device efficiency.

## 2.2 Pierce Theory

The amplification process in a TWT is a complex mechanism as it involves two systems that are coupled: the EM wave on the delay line and the particles of the electron beam. The theory of EM waves as well as particle physics are needed to describe TWT operation.

The following section is subdivided into three parts. The first is concerned with modeling the EM waves along the delay line, while the second describes the electron beam. The third then takes into account the interaction of these two systems for synchronous operation. The presented derivation is also known as the Pierce theory and gives much insight into the physics of TWTs. It is named after John R. Pierce who first described the interaction in a TWT in a closed form [15]. The following derivations are adapted from [11] and are given here for the sake of completeness, since the conclusions drawn from this theory become important for subsequent chapters.

In the following all field quantities implicitly depend on time  $t$  and axial distance  $z$  as  $\exp(j(\omega t - \beta z))$  with angular frequency  $\omega$  and propagation constant  $\beta$ . Therefore, it follows that

$$\frac{\partial}{\partial t} = j\omega, \text{ and} \quad (2.2)$$

$$\frac{\partial}{\partial z} = -j\beta. \quad (2.3)$$

## 2 Basics of Traveling-Wave Tubes

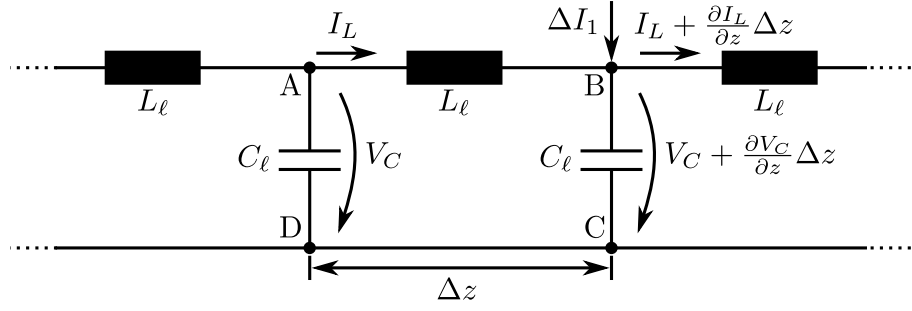


Figure 2.6: Transmission-line model of delay lines.

### 2.2.1 Circuit Equations

The delay line can be described by means of a transmission line (TL). An incremental element of length  $\Delta z$  exhibits the inductance  $L_\ell$  and the capacitance  $C_\ell$  per unit length. An adequate equivalent circuit (EC) is shown in Figure 2.6. An additional RF current  $\Delta I_1$  is induced at point B due to the presence of the electron beam. Applying Kirchhoff's current law in this point and Kirchhoff's voltage law around the closed loop ABCD with  $\Delta z \rightarrow 0$ , respectively, the differential equations

$$\frac{dV_C}{dz} = -j\omega L_\ell \cdot I_L, \text{ and} \quad (2.4)$$

$$\frac{dI_L}{dz} = \frac{dI_1}{dz} - j\omega C_\ell \cdot V_C \quad (2.5)$$

are obtained. Using Equation (2.3) and substituting  $I_L$  from Equation (2.5) into Equation (2.4) leads to

$$V_C = \frac{\omega\beta L_\ell}{\beta^2 - \omega^2 L_\ell C_\ell} I_1. \quad (2.6)$$

Assuming further that the electron beam travels close to the TL, the axial electric field  $E_z$  acting on the electrons can be calculated as

$$E_z = -\frac{dV_C}{dz} = j\beta V_C = \frac{j\omega\beta^2 L_\ell}{\beta^2 - \omega^2 L_\ell C_\ell} I_1. \quad (2.7)$$

Introducing the cold propagation constant  $\beta_c$  and the circuit impedance  $Z_c$

$$\beta_c = \frac{\omega}{v_p} = \omega\sqrt{L_\ell C_\ell} \quad \text{and} \quad Z_c = \sqrt{\frac{L_\ell}{C_\ell}}, \quad (2.8)$$

respectively, the electric field acting on the electron beam becomes

$$E_z = j \frac{\beta^2 \beta_c Z_c}{\beta^2 - \beta_c^2} I_1. \quad (2.9)$$

### 2.2.2 Space-Charge Waves on Electron Beams

In order to determine the propagation characteristics of EM waves along an electron beam, at first an infinite beam in transverse direction is considered. The propagation then follows from the solution of the wave equation with a source term stemming from the flow of negative charges. Since the transverse dimensions of the electron beam are assumed to be infinite, the following one-dimensional (1D) wave equation for the axial electric field  $E_z$  is obtained [11]

$$\frac{\partial^2}{\partial z^2} E_z + k^2 E_z = -j\omega\mu_0 J_1 - \frac{1}{\epsilon_0} \frac{\partial}{\partial z} \rho_1, \quad (2.10)$$

where  $k = \omega/c_0$  is the free-space wavenumber with  $c_0$  denoting the speed of light,  $\rho_1$  and  $J_1$  are the space-charge and current density modulation, respectively, and  $\mu_0$  and  $\epsilon_0$  are the vacuum permeability and permittivity, respectively. Applying Equation (2.3) to Equation (2.10) leads to

$$(\beta^2 - k^2)E_z = j\omega\mu_0 J_1 - \frac{j\beta}{\epsilon_0} \rho_1. \quad (2.11)$$

The total current density  $J$  is the product of the space-charge density  $\rho$  and the electron velocity  $u$ , i.e.,  $J = \rho u$ . Both  $\rho$  and  $u$  are assumed to have a DC and an RF component, therefore

$$\rho = \rho_0 + \rho_1 \cdot e^{j\omega t} \quad \text{and} \quad (2.12)$$

$$u = u_0 + u_1 \cdot e^{j\omega t}, \quad (2.13)$$

where subscripts 0 and 1 denote DC and RF quantities, respectively. The product of two RF quantities can be neglected, if their amplitudes are much smaller than the respective DC values. The current density modulation  $J_1$  then becomes

$$J_1 \approx \rho_0 u_1 + \rho_1 u_0. \quad (2.14)$$

Applying the continuity equation to the electron current density

$$\nabla \cdot \mathbf{J} + \frac{\partial \rho}{\partial t} = 0 \quad \text{or} \quad -j\beta J_1 = -j\omega \rho_1 \quad (2.15)$$

it follows from Equation (2.14) that

$$J_1 = \frac{\rho_0}{1 - \frac{\beta u_0}{\omega}} u_1. \quad (2.16)$$

The equation of motion for the electrons subject to an axial electric field  $E_z$  is given by

$$\frac{du}{dt} = \frac{\partial}{\partial t} u_1 + u_0 \frac{\partial}{\partial z} u_1 = (j\omega - j\beta u_0) \cdot u_1 = -\eta_e E_z, \quad (2.17)$$

## 2 Basics of Traveling-Wave Tubes

where  $\eta_e$  is the electron charge-to-mass ratio. Combining Equations (2.16) and (2.17) leads to

$$J_1 = j \frac{\omega \rho_0 \eta_e}{(\omega - \beta u_0)^2} E_z = j \omega \epsilon_0 \frac{\omega_p^2}{(\omega - \beta u_0)^2} E_z, \quad (2.18)$$

where the plasma frequency  $\omega_p^2 = (\eta_e \rho_0) / \epsilon_0$  has been introduced. It is convenient to replace  $\rho_0$  and  $u_0^2$  by  $J_0 / u_0$  and  $2\eta_e V_0$ , respectively. Additionally, the current densities can be replaced by the corresponding currents, since a one-dimensional problem is considered here, i.e.,

$$I_1 = \frac{j \beta_e I_0}{2V_0(\beta_e - \beta)^2} E_z, \quad (2.19)$$

where  $\beta_e = \omega / u_0$  is the electronic propagation constant.

If the transverse dimensions of the electron beam are finite, the above derivation still holds. However, the plasma frequency  $\omega_p$  has to be replaced by the reduced plasma frequency  $\omega_q$  according to

$$\omega_q = F \cdot \omega_p, \quad (2.20)$$

where  $F$  is the plasma reduction factor. It depends on the shape and size of the electron beam and of the metallic beam tunnel in which it travels [11].

### 2.2.3 Interaction

With the EM waves on the delay line and the space-charge waves of the electron beam individually described, they are now combined to take interaction into account. Therefore, Equations (2.9) and (2.19) have to be fulfilled simultaneously. Interaction between the systems mainly depends on synchronism, i.e., only those parts of the EM wave interact with the beam that have approximately the same axial phase velocity as the velocity of the electrons. The synchronous operation is briefly discussed here, because it gives crucial insights into the topic and will be helpful for later discussions. For asynchronous operation and more involved considerations like the influence of loss and noise, the reader is kindly referred to [11].

Combining Equations (2.9) and (2.19) results in the so-called determinantal equation

$$1 = \frac{\beta_e I_0}{2V_0(\beta_e - \beta)^2} \frac{\beta^2 \beta_c Z_c}{(\beta_c^2 - \beta^2)}. \quad (2.21)$$

Pierce further introduces the gain parameter  $C$  given by

$$C^3 = \frac{Z_c I_0}{4V_0} \quad (2.22)$$

which is usually a very small quantity, with typical values between  $10^{-2}$  and  $10^{-1}$ .

## 2 Basics of Traveling-Wave Tubes

Equation (2.21) is a fourth-order polynomial whose solutions yield the four propagation constants of the eigenmodes of the coupled system. Assuming forward-traveling modes, the coupled propagation constant  $\beta$  can be written under the assumption of synchronous waves, i.e.,  $\beta_e = \beta_c$ , as

$$\beta = \beta_e + \xi, \quad (2.23)$$

where it is further supposed that  $\beta$  differs only by a small amount  $\xi$  from  $\beta_e$ . Introducing this into Equation (2.21) leads to

$$\frac{\beta_e^2(\beta_e^2 + 2\beta_e\xi + \xi^2)}{\xi^2(2\beta_e\xi + \xi^2)}2C^3 + 1 = 0. \quad (2.24)$$

Since  $\xi$  is a very small quantity compared to  $\beta_e$ ,  $\xi^2$  can be neglected in comparison to  $\beta_e\xi$  in the denominator. The same holds for  $\beta_e\xi$  and  $\xi^2$  compared to  $\beta_e^2$  in the numerator. With these approximations Equation (2.24) can be directly solved for  $\xi$  to obtain

$$\xi = \sqrt[3]{-1}\beta_e C. \quad (2.25)$$

The three complex roots are then

$$\xi_1 = \left(\frac{1}{2} + j\frac{\sqrt{3}}{2}\right)\beta_e C, \quad (2.26)$$

$$\xi_2 = \left(\frac{1}{2} - j\frac{\sqrt{3}}{2}\right)\beta_e C, \text{ and} \quad (2.27)$$

$$\xi_3 = -\beta_e C, \quad (2.28)$$

and the respective propagation constants follow from Equation (2.23).

Remembering now that all waves are assumed to propagate according to  $\exp(j(\omega t - \beta z))$ , it becomes apparent that

1. all three modes travel in forward direction, since  $C$  is a small quantity,
2. two waves travel at the same speed, one growing and the other decreasing exponentially, and
3. one wave travels faster than the others and has a constant amplitude.

The fourth wave can be obtained by assuming a backward-traveling wave with a velocity close to that of the circuit wave in absence of the beam. The result is another fast wave with constant amplitude traveling in backward direction.

These considerations are important for Chapter 4 where coupled dispersion diagrams are calculated to determine the characteristic impedances of the coupled modes in order to minimize reflections at couplers and severs under hot operating conditions.

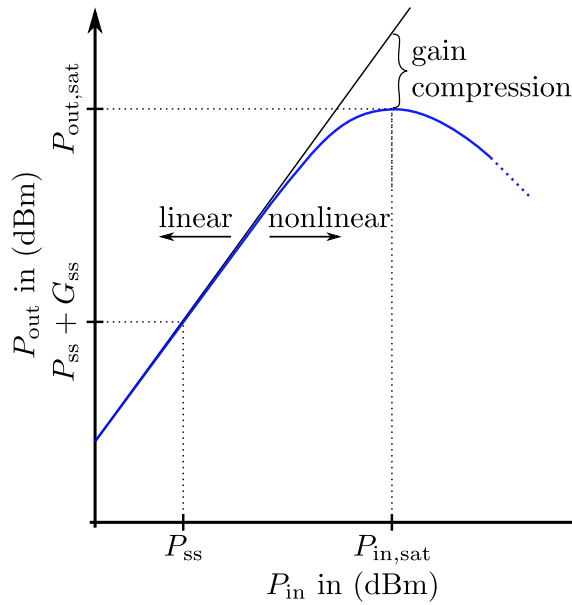


Figure 2.7: An exemplary drive curve of a nonlinear amplifier.

## 2.3 Nonlinear Interaction

For large-signal interaction the discrete nature of electrons as well as the forces between them have to be considered. With growing modulation the electrons start to bunch, because some electrons become slower and some faster than the average beam velocity. Additionally, kinetic energy is extracted by the delay line which in turn leads to a general decrease in electron velocity.

The generated bunches form regions of high space-charge field. The modulated electron beam then exhibits strong harmonics and acts as a nonlinear energy source. The electron bunches can only be sustained, if the axial electric field of the circuit is strong enough. The output power starts to saturate at some point, because the bunches tend to spread again and energy is transferred from the circuit to the beam instead of the other way around. A generic drive curve for amplifiers is depicted in Figure 2.7. For small input powers the output power increases linearly as indicated by the “linear” regime. Input and output power are then linked by a constant amplification  $G_{\text{ss}}$ . For higher input powers this gain decreases, i.e., compresses. The global maximum of the output power  $P_{\text{out}}$  is denoted as saturated output power  $P_{\text{out,sat}}$  with the respective input power being  $P_{\text{in,sat}}$ . Nonlinear effects in overdrive, i.e., for  $P_{\text{in}}$  greater than  $P_{\text{in,sat}}$ , may lead to deviations from the drive curve in Figure 2.7.

## 2.4 The Software Package *KlysTOP*

A brief explanation shall be given why specialized software is necessary even in times of high-performance computers. Also, background information is provided about the interaction simulation tool *KlysTOP* that is used in this thesis.

Several general-purpose three-dimensional (3D) full-wave tools exist today to predict the performance of TWTs, for example *CST Particle Studio*<sup>1</sup> or *MAGIC*<sup>2</sup>. Most of these tools compute the interaction in time domain. Today's computers do not have the appropriate capacity to manage such calculations in a time frame which allows efficient design cycles using these software packages. Their dominant field of use is the exploration of new concepts as well as the verification of measurement or simulation results.

For design purposes, however, it is more adequate to use specialized software tools. These can handle only a specific type of device or only work properly given certain prerequisites. The simulation time can be reduced from several hours to mere seconds per frequency point of interest. Specialized software can be further categorized into large-signal and small-signal tools. The latter are very fast but can only predict gain and not output power. Many small-signal codes implement the Pierce theory outlined earlier in this chapter. Large-signal tools, on the other hand, take nonlinear effects into account and can be just as accurate as their full-wave counterparts, depending on the properties of the underlying models.

*KlysTOP* is such a specialized software with both a small- and a large-signal implementation. Its name stems from the French expression “**K**lystron et **T**ube à **O**nde **P**rogressive” and means “klystron and traveling-wave tube”. In *KlysTOP* each cell of the delay line is described by an EC and an axial length, called pitch. The EC represents one or more modes of the delay line, while the pitch ensures that the spatial distribution of the circuit field is correctly reproduced which is important for the electrons inside the drift tube. The electron beam is modeled by Pierce's theory (small-signal version) or by discrete particles moving through a computational mesh and subjected to circuit and space-charge fields (large-signal version). The latter will be further discussed in this thesis, because a major contribution to the code has been accomplished in the course of this work.

---

<sup>1</sup><https://www.cst.com/products/cstps/>

<sup>2</sup><http://www.mrcwdc.com/Magic/>

### 3 Folded-Waveguide Delay Lines

In order to introduce a common notation, a brief overview over rectangular waveguides (RW) with a focus on the fundamental H<sub>10</sub>-mode is given before going into the details of FW delay lines and the modeling in general and in *KlysTOP*.

An RW consists of a dielectric filling, most commonly air, fully enclosed by metallic walls. A sketch of an RW is shown in Figure 3.1. In the following the RW is supposed to be evacuated. Its guiding properties can be derived analytically by solving the Helmholtz wave equation using separation of variables [16]. The derivations are not presented here. Only the main guiding principles and characteristics important for later considerations are summarized.

The propagation constant and characteristic impedance of the fundamental H<sub>10</sub>-mode are dictated by the width  $a_{\text{wg}}$  of the RW. The transverse electric field possesses only a  $y$ -component with constant amplitude in  $y$ -direction and a half-sine distribution in  $x$ -direction. The cutoff frequency  $f_c$  of this mode is

$$f_c = \frac{c_0}{2a_{\text{wg}}}, \quad (3.1)$$

where  $c_0 = (\mu_0\varepsilon_0)^{-1/2}$  is the speed of light. At frequency  $f = \omega/2\pi$  the propagation constant and characteristic impedance of the H<sub>10</sub>-mode are

$$\beta_{\text{wg}} = k \sqrt{1 - \left(\frac{f_c}{f}\right)^2} \quad (3.2)$$

and

$$Z_{\text{wg}} = \frac{Z}{\sqrt{1 - \left(\frac{f_c}{f}\right)^2}}, \quad (3.3)$$

respectively. The free-space wavenumber is denoted by  $k = \omega/c_0$  and the respective wave impedance is  $Z = (\mu_0/\varepsilon_0)^{1/2}$ . In the lossless case, the propagation constant  $\beta_{\text{wg}}$  is imaginary below  $f_c$  (evanescent damping), purely real above (propagation) and tends towards  $k$  for very high frequencies, i.e., the wave then propagates at the same speed as in free space.

### 3 Folded-Waveguide Delay Lines

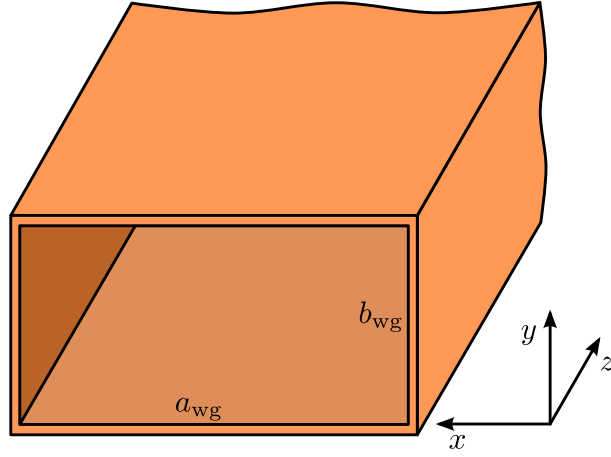


Figure 3.1: A rectangular waveguide.

## 3.1 General Topology

When used as a delay line, the waveguide is in general folded about the electron beam axis. The folds can be realized as  $90^\circ$  corners (FW) or as smooth bends (SW). In both cases the bends are located in the E-plane of the  $H_{10}$ -mode. Figure 3.2 shows an FW delay line. A unit cell of length  $p$  is indicated. A circular tunnel for the electron beam is located on the broad walls of the vertical waveguide sections. The electric field of the fundamental  $H_{10}$ -mode is axial as the waveguide crosses the beam path and points in opposite directions after each folding, thus incorporating an additional phase shift of  $\pi$  per unit cell.

As a rule of thumb, the phase velocity  $v_{\text{ph}}$  in axial direction far away from the cutoff frequency achieved by an FW delay line can be approximated by

$$\frac{v_{\text{ph}}}{c_0} \approx \frac{1}{1 + L_s/p + b_s/p}, \quad (3.4)$$

where  $L_s$  is the length of the vertical waveguide section,  $b_s$  is the waveguide height in the connecting slot, and  $p$  is the pitch. Equation (3.4) simply results from the different path lengths of beam and waveguide. The geometry parameters given in Figure 3.2 can be used to tune the delay line characteristics. Possible quantities to characterize delay lines are discussed in Section 3.2.1, while a parameter study is conducted in Section 3.2.2.

## 3.2 Eigenmode Simulation

Delay lines for TWTs are commonly characterized in the cold case, i.e., without influence of an electron beam. This still takes into account the presence of the electron beam tunnel, which can significantly affect the performance of the line.

### 3 Folded-Waveguide Delay Lines

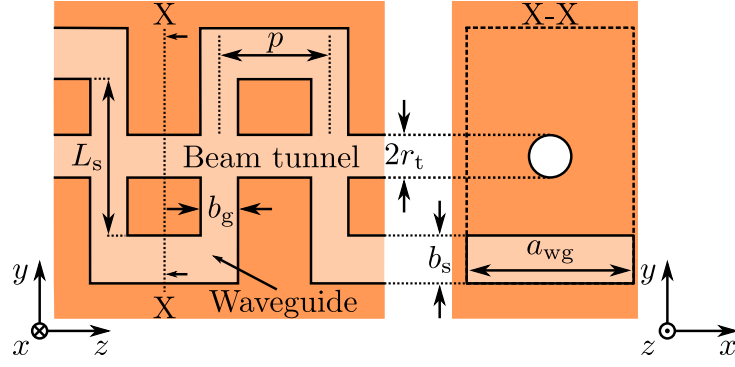


Figure 3.2: Longitudinal and cross section of a folded-waveguide delay line.

The propagation characteristics of EM waves on the delay line can be obtained from eigenmode simulation. A single unit cell of the periodic delay line is modeled and metallic parts are assumed to be a perfect electric conductor (PEC). The dispersion diagram of the line is obtained by imposing a periodic boundary condition in  $z$ -direction on the transverse fields. These are forced to differ in one plane from the ones in the next plane by a phase factor. For the transverse electric field this reads

$$\mathbf{E}_{\text{tan}}(x, y, z)|_{z=z_1+p} = \mathbf{E}_{\text{tan}}(x, y, z)|_{z=z_1} \cdot e^{-j\phi}, \quad (3.5)$$

where  $\phi$  is the phase advance of the respective mode with transverse complex field  $\mathbf{E}_{\text{tan}}(x, y, z)$  and  $z_1$  is an arbitrarily defined axial position. The phase advance  $\phi$  is related to the propagation constant  $\beta$  of the eigenmode and the length of the unit cell  $p$  via

$$\phi = \beta \cdot p. \quad (3.6)$$

The fields fulfilling Equation (3.5) are a sum of spatial harmonics, or space harmonics, according to Floquet's theorem [16]. Each harmonic differs from the other by an integer multiple of  $2\pi$  in phase. The  $n$ th space harmonic has the propagation constant

$$\beta_n = \beta_0 + \frac{2\pi n}{p} \quad (3.7)$$

with  $n \in \mathbb{Z}$  and  $\beta_0$  being the propagation constant of a space harmonic arbitrarily defined as the fundamental mode ( $n = 0$ ). In general, the overall field solution is a superposition of an infinite number of space harmonics. This means that the dispersion diagram only has to be computed for any continuous  $2\pi$  interval, because the results for all phase advances  $\phi$  are a  $2\pi$ -periodic function. This yields

$$\beta_n = \frac{\phi_0 + 2\pi n}{p} \quad (3.8)$$

### 3 Folded-Waveguide Delay Lines

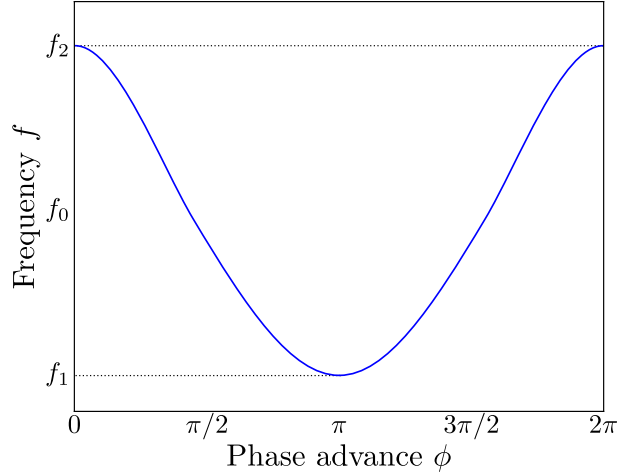


Figure 3.3: An exemplary first Brillouin zone of a dispersion curve.

with  $\phi_0 \in [0, 2\pi)$  and  $n \in \mathbb{Z}$ . All space harmonics have the same group velocity

$$v_{\text{gr}} = \frac{\partial \omega}{\partial \beta}, \quad (3.9)$$

but a different phase velocity

$$v_{\text{ph}} = \frac{\omega}{\beta}. \quad (3.10)$$

The latter is the important quantity for the synchronism condition in a TWT. Only one space harmonic of the periodic delay line is synchronous with the electrons in the beam.

A sample dispersion curve is depicted in Figure 3.3. The passband extends from the lower cutoff frequency  $f_1$  to the upper cutoff frequency  $f_2$  with a forward- and a backward-traveling wave as indicated by the slope of the band, i.e., with a positive and negative group velocity, respectively. At the band edges the group velocity tends to zero. This results in standing waves, i.e., no power is transported. Outside the passband waves cannot propagate. They are exponentially damped. The rate of attenuation increases with spectral distance to the passband.

#### 3.2.1 Characterization

Eigenmode simulation can be used to qualify delay lines. Two quantities are used in the following, namely the phase velocity  $v_{\text{ph}}$  and the coupling impedance  $R_c$  of the fundamental forward wave.

The phase velocity was already defined in Equation (3.10). A constant or minimally varying phase velocity is desirable. This is the case when the group velocity is constant, i.e., when the dispersion curve is linear.

### 3 Folded-Waveguide Delay Lines

The coupling impedance of a certain space harmonic and modal field distribution relates the amplitude of the space harmonic to the transported power along the delay line. It is thus a measure of the energy stored in this particular space harmonic. For a TWT the field strength in axial direction is important for beam-wave interaction. Therefore, the coupling impedance is defined as [11]

$$R_{c,n} = \frac{|E_n|^2}{2\beta_n^2 P}, \quad (3.11)$$

with  $E_n$  being the complex axial E-field amplitude of the  $n$ th space harmonic defined by

$$E_n = \frac{1}{p} \int_{-p/2}^{p/2} E_z(z) \cdot e^{j\beta_n z} dz, \quad (3.12)$$

where  $E_z(z)$  is the axial electric field and  $\beta_n$  is the propagation constant given by Equation (3.8). The total power  $P$  transported on the delay line is given by

$$P = \frac{1}{2} \iint_{A_w} \Re(S_z) dx dy, \quad (3.13)$$

where  $A_w$  is an arbitrary cross section through the unit cell,  $S_z$  the  $z$ -component of the Poynting vector, and  $\Re(S_z)$  its real part.

As already mentioned above, the space harmonics have different phase velocities. Only one of them is synchronous with the electrons in a TWT. The harmonic amplitudes  $|E_n|$  decrease with mode order  $n$ . Due to this fact it is desirable to design a delay line to be synchronous with the fundamental harmonic for strong interaction. The coupling impedance  $R_{c,0}$  of the fundamental space harmonic is denoted in the following by  $R_c$  for the sake of conciseness.

#### 3.2.2 Parameter Studies

Efforts were made in the past to shape the EM properties of FW delay lines [17–20]. In this section a parametrized conventional FW delay line is systematically analyzed.

A relatively good design of an FW delay line for application in Q-band is used as a starting point for the parameter study. The detailed geometry is given in Table 3.1. The indicated geometrical parameters are shown in Figure 3.2. They are varied about their nominal value to analyze the impact on the characteristic quantities given in Section 3.2.1. Additionally, a non-conventional topology intended to increase the coupling impedance is studied. Simulation is performed using the eigenmode solver of Ansys EM<sup>3</sup>.

<sup>3</sup><http://www.ansys.com/en/Products/Electronics>

### 3 Folded-Waveguide Delay Lines

Table 3.1: Parameter ranges in (mm).

	$p$	$r_t$	$L_s$	$a_{\text{wg}}$	$b_s$	$b_g$	$L_b$	$s_b$
Nominal	1.1	0.35	2.0	3.8	0.9	0.55	0.0	0.9
Min	0.85	0.1	1.75	3.2	0.65	0.3	0.0	–
Max	1.35	0.6	2.25	4.4	1.15	0.8	0.20	–
$\Delta$	0.05	0.05	0.05	0.05	0.05	0.05	0.025	–

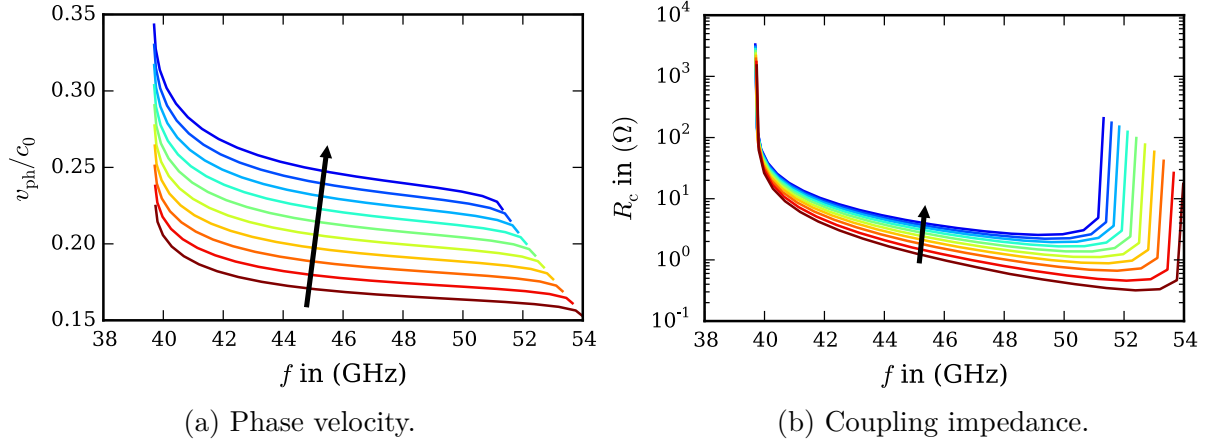


Figure 3.4: Influence of pitch  $p$ .

Several studies similar to those presented in the following, but with different geometries, have been conducted in the frame of this thesis. The tendencies observed during these studies were the same for each case. This suggests that the following investigations give fundamental trends for the analyzed delay line topology.

#### Pitch $p$

Varying the pitch is the standard way of tapering TWT delay lines, i.e., to change the phase velocity in axial direction. Figure 3.4 summarizes the results for such a variation in steps of  $50 \mu\text{m}$ . Figure 3.4(a) shows the phase velocity from which the dispersion and the passband can be deduced. The lower cutoff frequency of the first mode is invariant with regard to the pitch. The upper cutoff frequency, however, changes since it depends on the electrical length between discontinuities, i.e., the electron beam holes and the bends. For a constant gap height  $b_g$  a pitch variation results in different lengths of the waveguide section parallel to the beam axis. Aside from these effects it can be clearly observed that the pitch changes the phase velocity almost linearly. The proportionality for this sweep is approximately 1% of  $c_0$  for every step of  $50 \mu\text{m}$ .

### 3 Folded-Waveguide Delay Lines

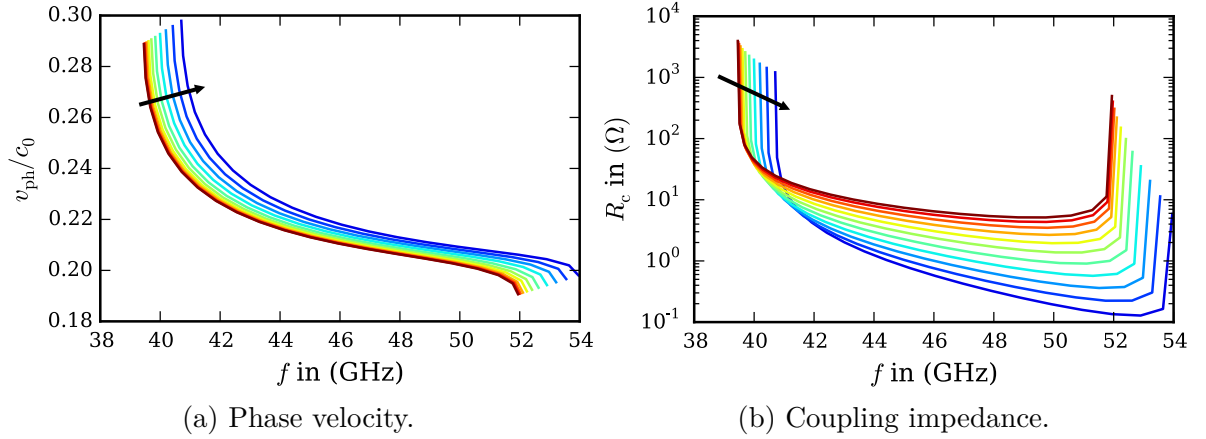


Figure 3.5: Influence of beam tunnel radius  $r_t$ .

The impact on the coupling impedance can be seen in Figure 3.4(b). The larger the pitch, the higher the coupling impedance becomes. Keeping in mind the logarithmic scale of the ordinate, the impact is tremendous. Unfortunately, towards the end of a tube the pitch has to be decreased for the wave to stay synchronous with the electron beam. This results in a lower coupling impedance which impairs the performance of the tube. The lower the coupling impedance, the weaker the axial electric field is. A strong field is needed to counteract the space-charge forces of the electron bunches. However, a higher coupling impedance closer to the input is also beneficial as it increases the gain per unit length and thus allows for shorter devices.

#### Beam Tunnel Radius $r_t$

The beam hole diameter is a parameter to be chosen carefully. It should be as large as necessary and as small as possible. A wide beam tunnel allows for a higher beam current, because the beam radius can be larger, thus leading to smaller space-charge forces. However, a wide beam tunnel affects the electrical performance of the delay line more strongly, which is shown in the following.

Regarding Figure 3.5(a) it can be seen that the beam hole radius influences both cutoff frequencies of the fundamental propagating mode. As a consequence the phase velocity also changes, but the effect is not as pronounced as for the pitch. The relative bandwidth is only slightly higher for smaller beam hole radii, because the absolute bandwidth stays approximately constant.

The impact on the electric field on the axis is much stronger compared to the dispersive effects. A smaller beam tunnel turns out to be beneficial for the coupling impedance. This is easily explained when considering the field distortions at the edges of the beam hole. These distortions lead to locally stored energy and large field

### 3 Folded-Waveguide Delay Lines

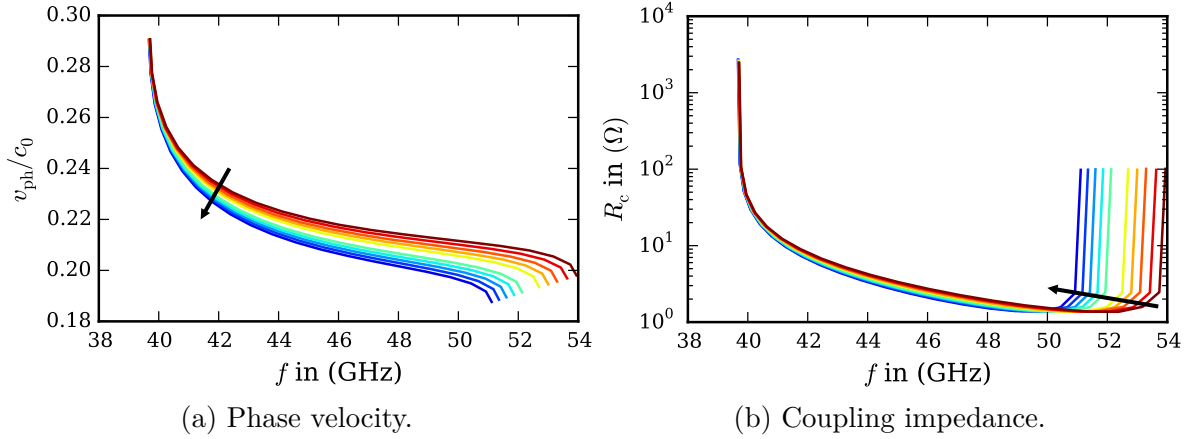


Figure 3.6: Influence of straight waveguide section  $L_s$ .

amplitudes, thus increasing the axial electric field. This observation tips the scales in favor of a small beam tunnel. It should be as small as possible while still being able to handle the required electron beam current. However, the smaller the beam radius for a given beam current the larger the space-charge forces, so this advantage could be diminished when these effects are taken into account. Consequently, the choice of a proper beam tunnel size constitutes an important trade-off.

#### Waveguide Length $L_s$

The length of the waveguide section traversing the beam axis mainly influences the phase velocity. To ensure mechanical stability of the slow-wave structure (SWS) a certain minimum length is required.

Figure 3.6(a) depicts the influence of  $L_s$  on the phase velocity. The lower cutoff is insensitive to this parameter, but the upper cutoff is changed, because the electrical length between discontinuities changes. Inside the passband the phase velocity changes nonlinearly with  $L_s$ , since the lower cutoff stays constant. Close to this frequency, the dispersion is strongest and therefore the effect of this parameter becomes more pronounced at higher frequencies.

The variation of the coupling impedance with  $L_s$  is illustrated in Figure 3.6(b). Here the effects are rather small, the shift of the upper cutoff frequency being the most obvious. However, it can also be seen that the coupling impedance inside the passband is slightly higher for smaller  $L_s$ . The electric field is higher relative to the total EM energy when this waveguide section is smaller, because the overall volume is smaller. Figuratively, the wave traveling on the delay line “sees” the beam axis more often and therefore the coupling impedance increases.

### 3 Folded-Waveguide Delay Lines

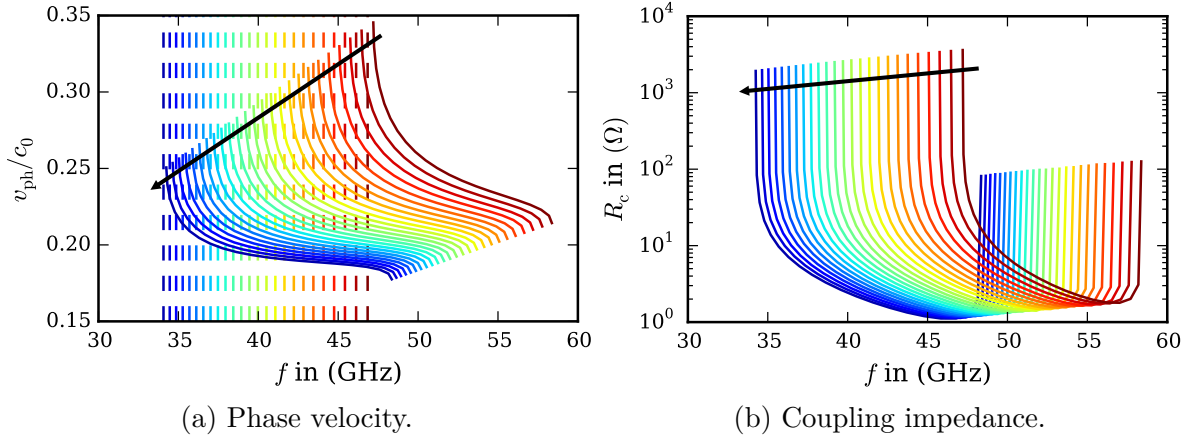


Figure 3.7: Influence of waveguide width  $a_{wg}$ .

#### Delay Line Width $a_{wg}$

The width  $a_{wg}$  dictates the lower cutoff of a straight waveguide. Therefore, this parameter is also the most important one for FW delay lines. However, as the waveguide is not straight, evanescent coupling between discontinuities can occur which may shift the lower cutoff frequency slightly.

The phase velocity for a variation of  $a_{wg}$  is shown in Figure 3.7(a). For convenience the lower cutoff frequencies of the respective straight waveguide  $H_{10}$ -modes are indicated by dashed vertical lines. They are strongly correlated with the lower cutoff of the FW delay line. For very large values of  $a_{wg}$  the cutoff frequency is very low and the phase velocity is approximately constant over a large bandwidth. On the other hand, for very narrow waveguides the lower cutoff frequency is shifted towards higher frequencies and the phase velocity becomes strongly dispersive.

The waveguide width has only a small impact on the coupling impedance  $R_c$ . Apart from the shift in frequency, the impedance curves are very similar. Nevertheless,  $R_c$  is slightly higher for narrower delay lines, because the field energy is more concentrated at the location of the electron beam.

#### Slot Height $b_s$

Varying the height  $b_s$  of the waveguide section parallel to the beam tunnel leads to the dispersion curves shown in Figure 3.8(a). The smallest slot height corresponds to approximately the waveguide height  $b_g$  at the beam tunnel. This case constitutes the smallest discontinuity for the local  $H_{10}$ -mode along the waveguide path. The transverse field shape does not change as strongly as in the other cases. The upper cutoff frequency is shifted when the local reflections at the bends are increased.

### 3 Folded-Waveguide Delay Lines

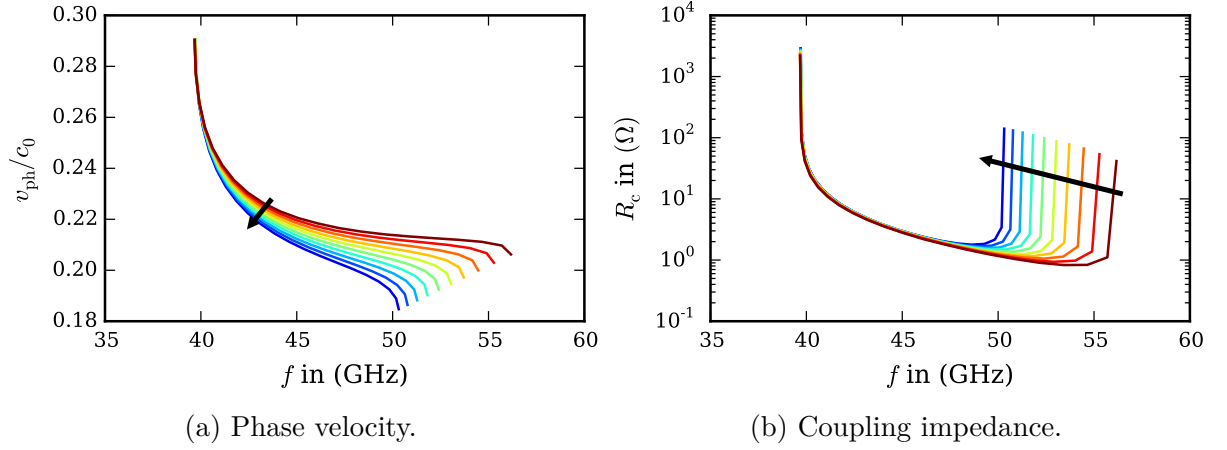


Figure 3.8: Influence of connecting slot height  $b_s$ .

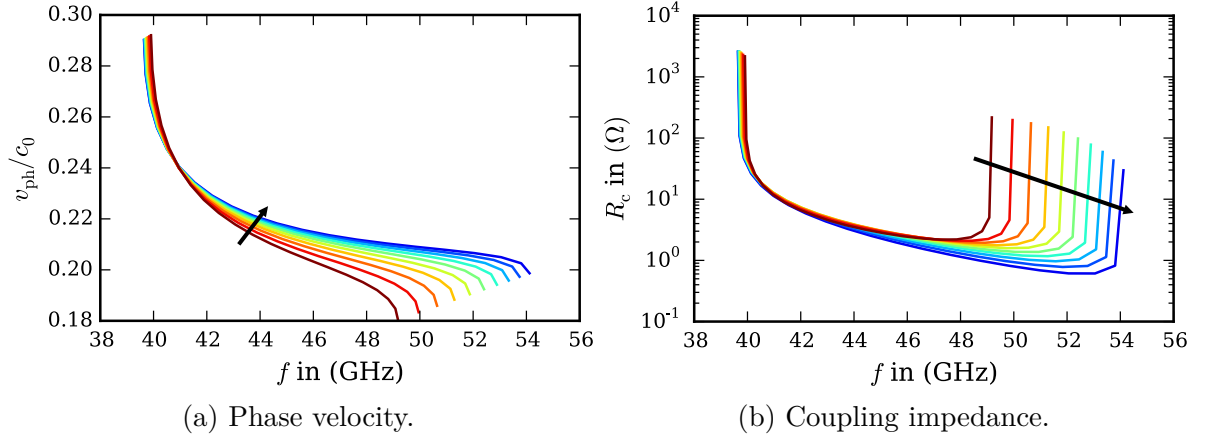


Figure 3.9: Influence of gap height  $b_g$ .

Thus, very large or very small ratios  $b_s/b_g$  yield a more narrowband behavior with strongly pronounced dispersion.

Changing  $b_s$  affects the coupling impedance only marginally, because the change is at a place far away from where it is determined. This is clearly observed in Figure 3.8(b). Indeed, all curves are identical at the lower cutoff and only start to deviate toward the upper cutoff frequency.

#### Waveguide Height $b_g$

The height  $b_g$  of the vertical waveguide section has an effect similar to the previously studied parameter  $b_s$ . The largest simulated value of  $b_g$  is closest to the nominal value of  $b_s$  which leads to the least dispersive and most broadband characteristic as can be seen in Figure 3.9. The lower cutoff is only marginally affected by a variation

### 3 Folded-Waveguide Delay Lines

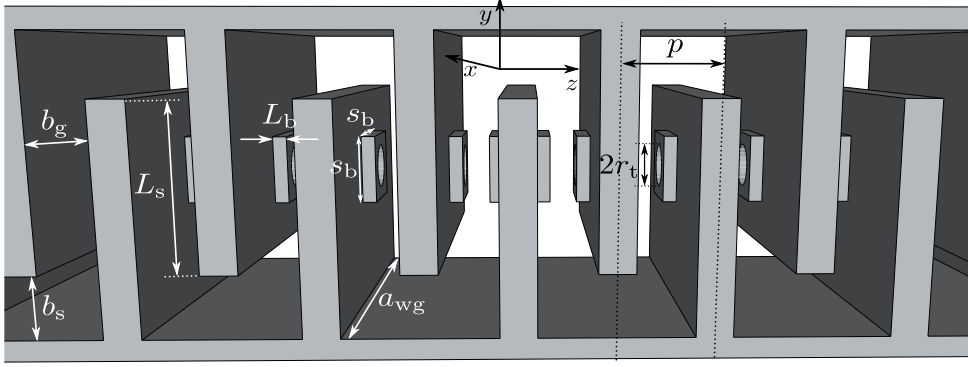


Figure 3.10: Geometrical parameters of a folded waveguide with nose cones. Side walls are transparent.

of  $b_g$ , while the upper cutoff frequency is shifted due to a change in coupling strength between the bend discontinuities. The effect on the interaction impedance  $R_c$  is similar, but more pronounced compared to the previous case. This parameter can be used to control the shape of the electric field to some degree. However, the bandwidth is substantially decreased in the process.

#### Nose-Cone Loaded Folded Waveguide

One major drawback of FW delay lines is their relatively weak coupling to the electron beam, manifesting in a low coupling impedance  $R_c$ . This reduces the maximum achievable beam efficiency [11]. It is therefore advantageous to shape or enhance the electric field on the axis to increase the coupling impedance of the fundamental space harmonic with only minor influence on the bandwidth.

Following the ideas from superconducting accelerator cavities [21] and the findings of the previous section, a nose cone is introduced as indicated in Figure 3.10. The nose cone functions as an extension of the beam tunnel into the vertical waveguide section. It has length  $L_b$  and its outer cross section is a square with side length  $s_b$ , while the beam tunnel still has a circular cross section. The nose cones allow to shape the electric field to enhance the content of the fundamental space harmonic. Additionally, the magnitude of the total electric field is increased due to local field distortions introduced by the nose cones.

Figure 3.11(a) illustrates the influence of the nose cone length  $L_b$  on the phase velocity. For this analysis  $L_b$  is increased in steps of  $25 \mu\text{m}$ . As expected, the phase velocity is least dispersive without nose cone, i.e.,  $L_b = 0$ . Introducing a nose cone shifts the lower cutoff to longer wavelengths and results in more pronounced dispersion. While the absolute bandwidth is decreased for longer nose cones, the relative bandwidth is only marginally affected (in the range of a few percent). The

### 3 Folded-Waveguide Delay Lines

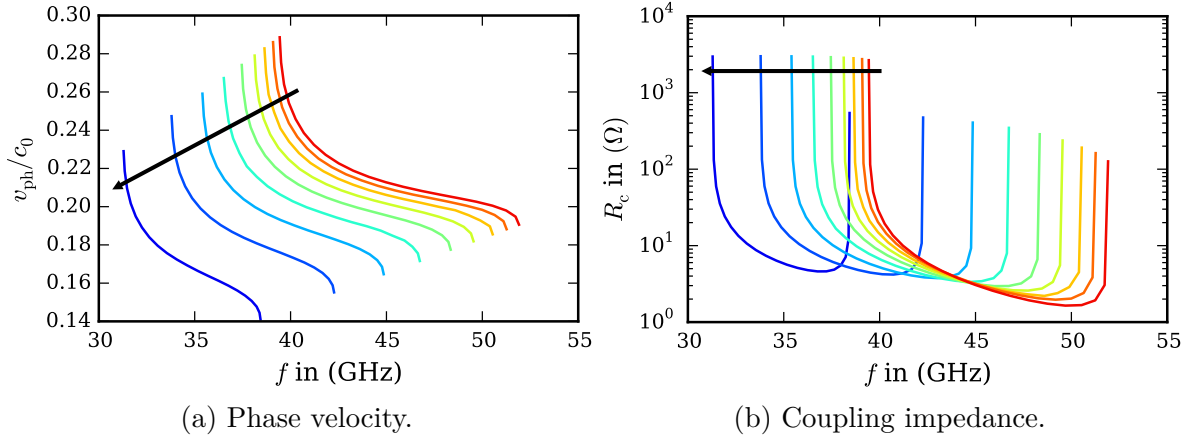


Figure 3.11: Influence of nose cone length  $L_b$ .

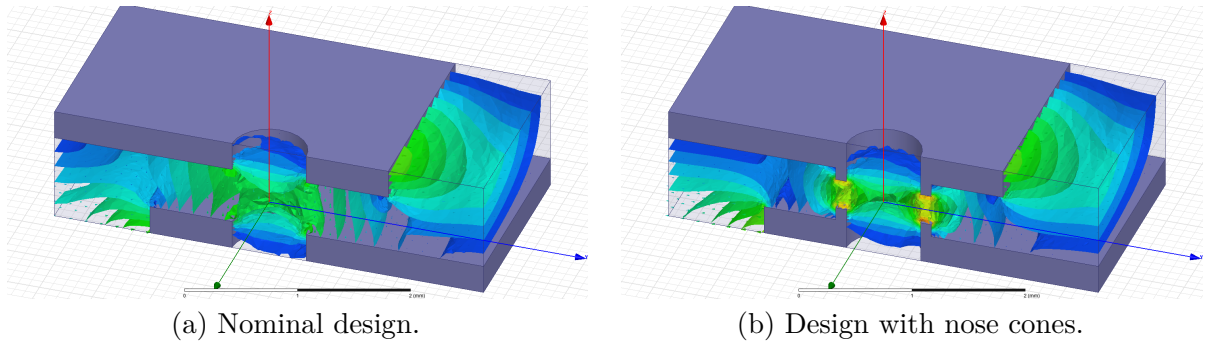


Figure 3.12: Comparison of electric field with and without nose cone. Color scales are equal for both figures.

shift to lower frequencies can be counteracted by scaling the geometry to the desired frequency band.

Figure 3.11(b) shows the impact on the coupling impedance. The minimum of the coupling impedance is increased by a factor of two to three. However, the effect saturates and is also limited by the waveguide height  $b_g$  at the beam tunnel. The maximum achievable beam efficiency  $\eta_{beam}$  is proportional to the cubic root of the coupling impedance [11, p.299]. The observed increase of the coupling impedance by a factor of two thus results in a 26 % larger maximum efficiency. Considering thermal and power management on a satellite, this increase has tremendous implications for a communication system. This modification makes the FW line a lot more attractive for high-efficiency applications.

A comparison between the electric field of FW delay lines with and without nose cone is shown in Figure 3.12. The isosurfaces indicate equal field strength where blue and red correspond to low and high field values, respectively. The fields of the

### 3 Folded-Waveguide Delay Lines

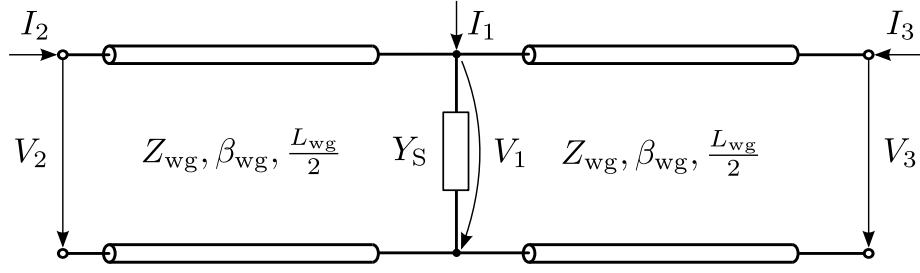


Figure 3.13: Equivalent-circuit model of folded-waveguide unit cell.

nominal design in Figure 3.12(a) shows the usual field distribution of FW delay lines. Around the beam tunnel the fields are distorted and non-axial field components are excited that do not contribute to beam-wave interaction. Apart from corner effects, the field strength is more or less the same along the waveguide. The fields in Figure 3.12(b) of a nose-cone loaded design exhibit larger field amplitudes around the beam tunnel. The fields are more focused there, leading to the earlier observed enhancement of the coupling impedance.

## 3.3 Equivalent Circuit Representation

For beam-wave interaction simulation using *Klystron* it is necessary to implement an EC model for FW delay lines. Antonsen provided a simple and accurate model for FW lines that describes the lowest propagating mode using five parameters [22]. Although the model is relatively simple, the lower part of the second propagating mode is also modeled quite accurately. Their model is briefly outlined here and can be assessed in detail in [22] and [23].

A schematic of Antonsen's FW model is depicted in Figure 3.13. It consists of two TLs. Parameters for each TL are assumed to be those of a straight RW. The TLs are separated by a shunt admittance  $Y_S$ . The influence of the beam tunnel and the bends is subsumed in this admittance which is a parallel  $LC$  resonant circuit. The model parameters are the length  $L_{wg}/2$  of each TL, the lower cutoff frequency  $f_c$ , the resonant frequency  $f_S$  of the shunt, the magnitude  $\hat{Y}_S$  of the admittance, and the impedance parameter  $Z_\infty$  which is defined as the waveguide characteristic impedance for  $f \rightarrow \infty$  (see Equation (3.3)). Furthermore, Antonsen uses the quantity

$$\Delta_\infty = \frac{Z_\infty \cdot \hat{Y}_S}{2} \quad (3.14)$$

instead of  $\hat{Y}_S$  as a model parameter.

Most of these parameters can be directly related to physical dimensions of the delay line. However, in doing so one neglects the influence of the periodic nature of

### 3 Folded-Waveguide Delay Lines

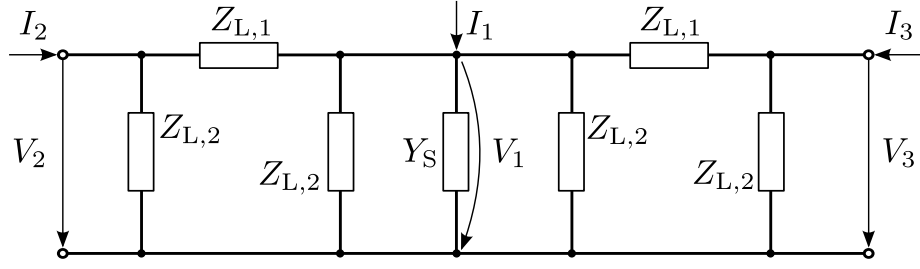


Figure 3.14: Lumped-element circuit folded-waveguide model.

the delay line. It is therefore preferable to use these parameters to fit the dispersion curve and the coupling impedance obtained by eigenmode analysis. The fitting process is described in the following section.

The coupling impedance of an EC cannot be directly compared to the one obtained by eigenmode simulation. The distribution of the electric field along the electron beam path is needed for this purpose (see Equation (3.11)). In the EC only a voltage  $V_1$  at the location of the beam, the so-called beam port, can be obtained and related to the transmitted power  $P$  along the EC. This results in the definition of the Kino impedance through [24]

$$R_{\text{Kino}} = \frac{|V_1|^2}{2P}. \quad (3.15)$$

The Kino impedance does not take into account the shape of the axial electric field. It is a measure of the total electric field strength relative to the transported power. Therefore, it is not suited to predict the interaction strength of a certain space harmonic.

The Kino impedance according to Equation (3.15) can also be calculated from full-wave eigenmode results. The complex axial electric field is integrated to yield the complex-valued gap voltage  $V_1$ , and the power is computed by means of Equation (3.13).

The EC in Figure 3.13 contains TL sections that can be replaced by an EC representation according to [25]. This EC exhibits the same behavior at the ports as a TL with the same characteristic quantities. The complete lumped EC is shown in Figure 3.14. The impedances are calculated as [25]

$$Z_{L,1} = Z_{\text{wg}} \cdot \tanh(\gamma L_{\text{wg}}/4) \text{ and} \quad (3.16)$$

$$Z_{L,2} = Z_{\text{wg}} \cdot (\sinh(\gamma L_{\text{wg}}/2))^{-1}. \quad (3.17)$$

where  $\gamma = j\beta_{\text{wg}}$  is the propagation constant of the line segment. From the EC shown in Figure 3.14 a three-port impedance matrix can be derived that describes the propagation in one unit cell of an FW delay line and provides a means to

simulate the interaction with an electron beam. Losses along the FW line can be incorporated by introducing a complex propagation constant  $\gamma = \alpha + j\beta_{\text{wg}}$  with  $\alpha$  being the attenuation constant. It can be obtained, for example, by a perturbation approach assuming low metallic losses [26].

### 3.3.1 Dispersion of the Equivalent Circuit Model

Once the impedance matrix of a unit cell of an FW delay line is known, the dispersion and electrical parameters of the periodic line can be readily deduced using an eigenvalue approach similar to that in Section 3.2 and Equation (3.5). Without electron beam, the three-port network in Figure 3.14 can be reduced to two ports by terminating port 1 by an open circuit, i.e.,  $I_1 = 0$ . The reduced impedance matrix  $[Z]$  with ports labeled as in Figure 3.14 is defined by

$$\begin{pmatrix} V_2 \\ V_3 \end{pmatrix} = [Z] \cdot \begin{pmatrix} I_2 \\ I_3 \end{pmatrix}. \quad (3.18)$$

It can be transformed into the voltage-current transfer matrix  $[T]$  defined by

$$\begin{pmatrix} V_3 \\ -I_3 \end{pmatrix} = [T] \cdot \begin{pmatrix} V_2 \\ I_2 \end{pmatrix} \quad (3.19)$$

in a straightforward manner. The transfer parameters then become

$$[T] = \begin{pmatrix} T_{11} & T_{12} \\ T_{21} & T_{22} \end{pmatrix} = \frac{1}{Z_{23}} \begin{pmatrix} Z_{33} & -\det([Z]) \\ -1 & Z_{22} \end{pmatrix}. \quad (3.20)$$

Assuming a reciprocal and symmetrical two-port network with respect to ports 2 and 3 results in

$$[T] = \frac{1}{Z_{23}} \begin{pmatrix} Z_{22} & Z_{23}^2 - Z_{22}^2 \\ -1 & Z_{22} \end{pmatrix}. \quad (3.21)$$

For a lossless and periodic delay line the voltages and currents of propagating modes at port 3 are the same as those at port 2 except for a phase factor. The eigenvalue problem

$$[T] \cdot \mathbf{x} = \psi \cdot \mathbf{x} \quad (3.22)$$

leads to eigenvectors  $\mathbf{x}$  and corresponding eigenvalues  $\psi$  of the periodic unit cell. From these the propagation constant and other electrical parameters can be obtained. The characteristic equation

$$p(\psi) = \det([T] - \psi[I_2]) = \psi^2 - 2\frac{Z_{22}}{Z_{23}}\psi + 1 \stackrel{!}{=} 0 \quad (3.23)$$

### 3 Folded-Waveguide Delay Lines

can be solved analytically and the eigenvalues are

$$\psi_{1,2} = \frac{Z_{22}}{Z_{23}} \pm \sqrt{\left(\frac{Z_{22}}{Z_{23}}\right)^2 - 1}, \quad (3.24)$$

where  $\psi_1$  and  $\psi_2$  correspond to the forward and the backward mode, respectively. The phase and magnitude of  $\psi_{1,2}$  yield the phase shift and damping per unit cell, respectively. For lossless lines the magnitude of  $\psi_{1,2}$  is one for propagating modes and unequal to one for evanescent modes.

The voltages and currents of the forward and backward modes follow from

$$V^\pm = \sqrt{Z_{22}^2 - Z_{23}^2} \cdot I_{\text{eig}}, \text{ and} \quad (3.25)$$

$$I^\pm = \pm I_{\text{eig}}, \quad (3.26)$$

where  $I_{\text{eig}}$  is an arbitrary current that represents a degree of freedom inherent to this eigenvalue problem. The superscripts “+” and “−” denote the amplitude of the forward- and backward-traveling mode, respectively. From Equations (3.25) and (3.26) the characteristic impedance of the periodic delay line is calculated according to

$$Z^\pm = \frac{V^\pm}{I^\pm} = \pm \sqrt{Z_{22}^2 - Z_{23}^2}. \quad (3.27)$$

Additionally, the Kino impedance can be derived directly from the  $Z$ -parameters of the unit cell. Using circuit theory, the voltage at the interaction gap (port 1) and the transported power are obtained from

$$V_1 = I_{\text{eig}} \cdot (\psi Z_{12} - Z_{13}) \text{ and} \quad (3.28)$$

$$P = 0.5 \cdot \Re(V^\pm I^{\pm*}) = \pm 0.5 \cdot |I_{\text{eig}}|^2 \cdot \Re(\sqrt{Z_{22}^2 - Z_{23}^2}), \quad (3.29)$$

respectively. From these the Kino impedance follows using Equation (3.15).

#### 3.3.2 Abstract Coupler and Sever Model

The EC model presented in the previous section allows to setup a delay line circuit. However, a circuit topology to include couplers and severs is missing. Therefore, it cannot be used in a simulation tool without further work. Energy has to be injected into and extracted from the delay line. Additionally, a sever model is needed, because conventional TWTs are in general equipped with one or more severs to improve stability.

Proper models for such devices are necessary when a new model for a type of delay line is to be tested. Therefore, it would be preferable to model ideal couplers and severs, i.e., to directly excite the wave on the delay line without reflections,

### 3 Folded-Waveguide Delay Lines

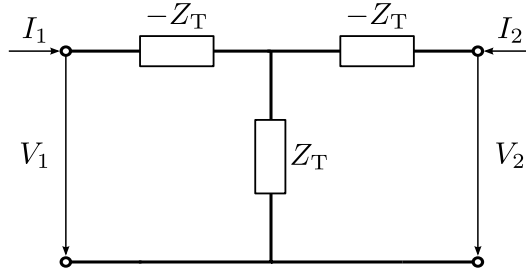


Figure 3.15: Abstract model of ideal coupler.

and absorb the wave in a similar fashion. In order to achieve this, the characteristic impedance of the periodic line has to be known [26]. This quantity follows from Equation (3.27) and can be used once the  $[Z]$  matrix of the delay line is known.

This impedance can be used to abstractly model couplers with the possibility of implementing an arbitrary (local) reflection coefficient  $\Gamma$ . A possible EC for a transformer that exhibits such a behavior is given in Figure 3.15. The impedance parameter  $Z_T$  of the transformer is given by [26]

$$Z_T = -j\sqrt{Z_1 Z_2}, \quad (3.30)$$

where  $Z_1$  and  $Z_2$  are the reference impedances at port 1 and 2, respectively. If one of the impedances in Equation (3.30) is modified according to

$$\tilde{Z}_i = Z_i \frac{1 + \Gamma}{1 - \Gamma}, \quad (3.31)$$

a complex local reflection factor  $\Gamma$  can be taken into account. It does not matter which impedance is modified, since the transformer EC in Figure 3.15 is symmetric.

In a similar fashion the impedance of Equation (3.27) can be used to model a sever which corresponds to a load impedance to absorb the periodic wave. A predefined reflection factor can also be considered using Equation (3.31).

#### 3.3.3 Nonlinear Curve Fitting

Antonsen's FW model has four degrees of freedom to adjust the dispersion of the delay line and one additional degree for the impedance level of the EC. The model does not rely on the real physical dimensions of the delay line as similar models do, e.g. [27]. This is a major advantage of this model, because it allows for a much more accurate prediction of the phase velocity, which is crucial for interaction simulation.

This accuracy comes at a price, because the five parameters of the model have to be determined. This can be achieved by minimization, for example. The function to be minimized is the RMS error between the characteristics obtained from the EC and those from eigenmode simulation. First, the four parameters

### 3 Folded-Waveguide Delay Lines

Table 3.2: Parameters obtained by curve fitting.

	$f_c$ in (GHz)	$L_{\text{wg}}$ in (mm)	$Z_c$ in ( $\Omega$ )	$f_s$ in (GHz)	$\hat{Y}_S$ in (mS)
B-FW	38.42	3.09	151.24	42.23	9.13
NC-FW	37.45	2.90	161.17	37.47	11.41

determining the dispersion are obtained by minimizing the deviation of the  $\omega$ - $\beta$  curves. The physical dimensions of the delay line are used as initial values in this process. The minimization is performed by Basin-Hopping [28] in this work. There are multiple parameter sets that lead to the same model accuracy, i.e., there is no unique minimum. That said, it is sufficient to acquire one set of parameters satisfying a desired accuracy in contrast to finding a global minimum. Chernin also proposed a method to reduce the number of fitting parameters by including additional information about the dispersive behavior of the model [23].

When the dispersion parameters are fixed, the impedance of the TLs is obtained by setting the Kino impedance of the model to the one calculated from the eigenmode fields at a certain frequency. Usually, this frequency is chosen to be at the center of the operating band.

An exemplary fitting result for an FW with geometrical parameters given as “Nominal” in Table 3.1 is shown in Figure 3.16. The resulting model parameters for this basic FW (B-FW) are listed in Table 3.2. The dispersion of the lowest propagating mode in Figure 3.16(a) is rendered very accurately by the model. Despite the simplicity of the model, the lower part of the upper mode is also described very well with deviations arising toward higher frequencies. The obtained Kino impedance is shown in Figure 3.16(b). It is fitted at a frequency of 45 GHz and agrees well with the full-wave results for the fundamental mode.

The relative deviations  $\Delta_{\text{rel}}$  for the dispersion and Kino impedance are plotted in Figure 3.16(c) over frequency. According to [29] a delay line model should render the phase velocity and the Kino impedance with an accuracy of 0.5% and 10%, respectively. Therefore, the obtained results for dispersion and Kino impedance are well within the required boundaries for accurate interaction simulation of the lowest propagating mode.

The model is still accurate when introducing a nose cone into the FW delay line. The geometry is identical to that of the B-FW, except for the nose cones. Their dimensions are given by  $L_b = 0.125$  mm and  $s_b = 0.9$  mm (cf. Figure 3.10). The EC parameters for the nose-cone loaded FW (NC-FW) obtained through minimization are also given in Table 3.2. Eigenmode and EC model results are compared in Figure 3.17. Again, the accuracy for the dispersion is around 0.2% for the lower mode, and the upper mode is well represented near its lower cutoff. The relative error of the Kino impedance is well below 5% inside the lower passband.

### 3 Folded-Waveguide Delay Lines

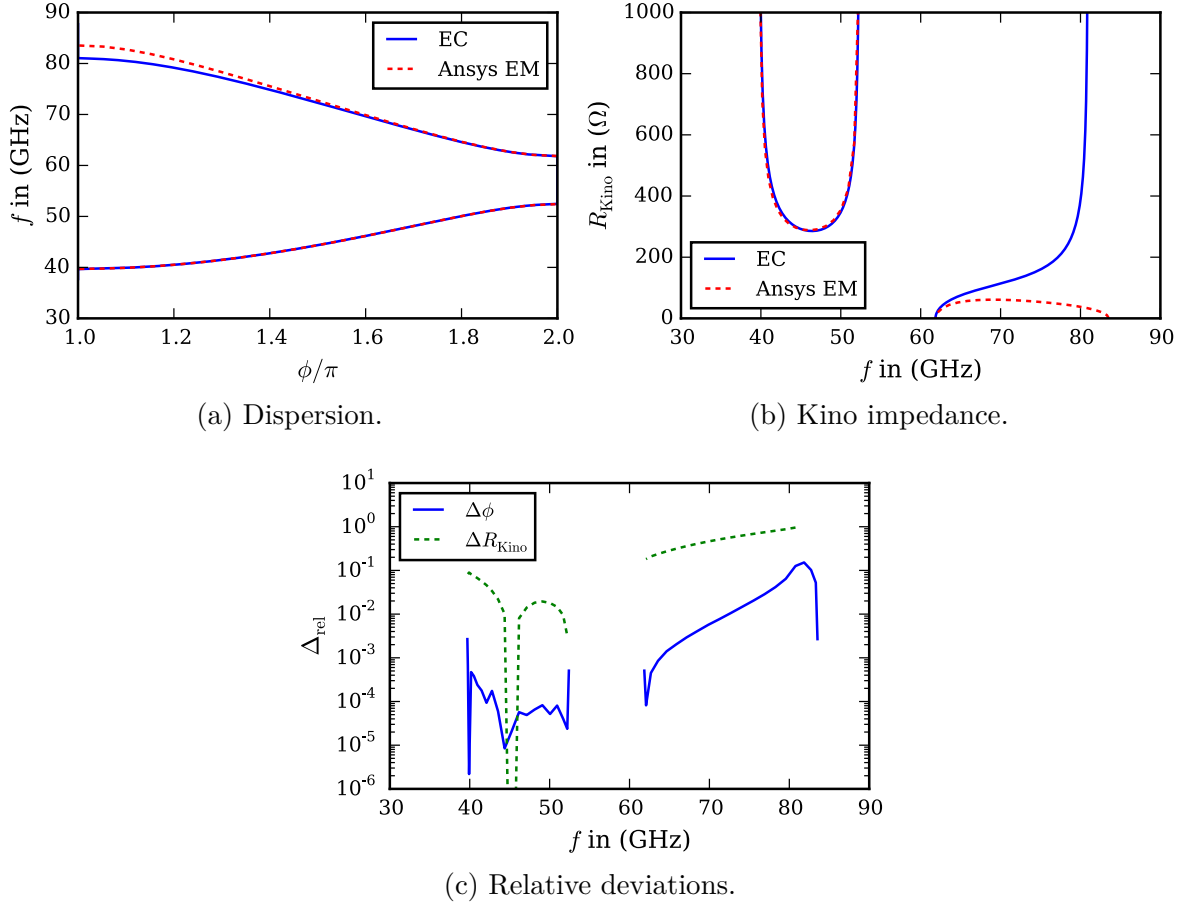


Figure 3.16: Comparison of results obtained by equivalent-circuit model and *Ansys EM* for the nominal design.

A few remarks can be made when comparing the two sets of model parameters in Table 3.2. Although the model parameters are obtained by a curve fitting process, certain conclusions and physical interpretations can be drawn from their respective values. First of all, the nose cone shifts the cutoff frequency of the TL to lower frequencies. This fact was already observed in Section 3.2.2 for the folded line. Additionally,  $L_{\text{wg}}$  is reduced although the physical length is the same in both cases. This means, however, that the electrical length of the TLs has changed which leads to a different upper cutoff frequency. The shunt resonant frequency  $f_S$  is also reduced and incidentally lies in the range of the lower cutoff frequency  $f_c$  for the NC-FW line. The amplitude  $\hat{Y}_S$  of the shunt admittance relative to the waveguide impedance  $Z_c$  is considerably larger for the NC-FW case. Physically, the nose cones introduce distortions manifesting in local reflections. In the model, a large shunt admittance amplitude  $\hat{Y}_S$  leads to more pronounced reflections, since the admittance is connected in shunt between the two TL sections.

### 3 Folded-Waveguide Delay Lines

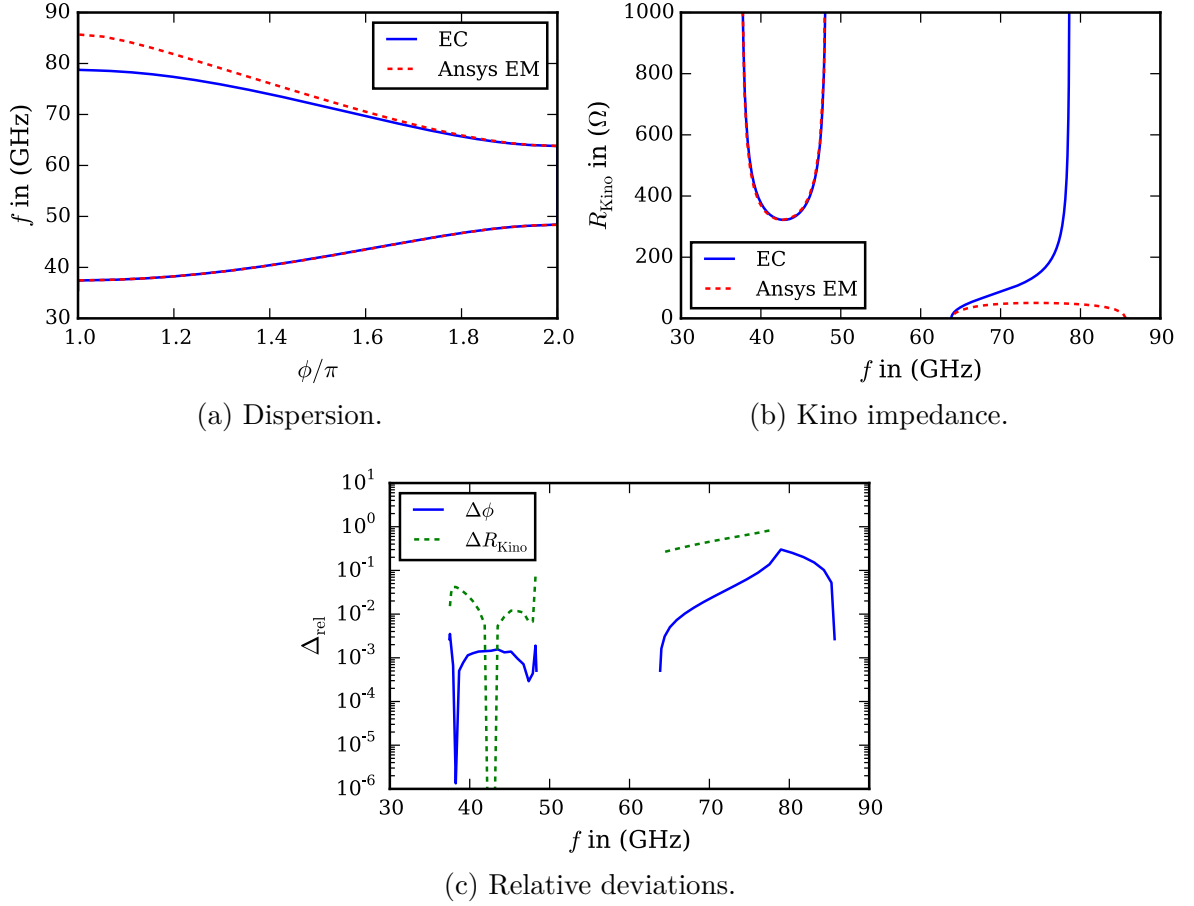


Figure 3.17: Comparison of results obtained by equivalent-circuit model and *Ansys EM* for the design with nose cones.

#### 3.3.4 Correction of Electric Field Shape

As has been mentioned above, only the Kino impedance can be obtained from the EC representation. However, for interaction simulation it is more important to describe the coupling impedance accurately. For this purpose the shape of the axial electric field across the beam cross section is needed. In *KlysTOP* an approximation of the actual electric field is obtained by solving the Laplace equation

$$\Delta\varphi = 0 \quad (3.32)$$

in the electron beam region where  $\varphi$  is an electrostatic potential. The resulting field shape is normalized such that its integral is 1 V. On the axis it is Gaussian-like. The field is maximum in the center of the interaction gap and decays into the beam tunnel region. Away from the beam axis the field is more strongly concentrated in the vicinity of the gap. For radii approaching the beam tunnel, the field is approximately zero outside the gap and similar to a cosine hyperbole inside the

### 3 Folded-Waveguide Delay Lines

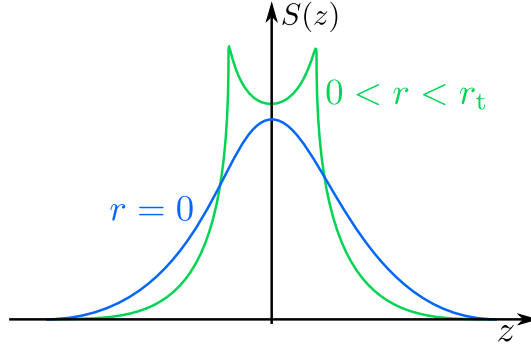


Figure 3.18: Field shapes used in *KlysTOP*.

gap. Field shapes of the axial electric field  $E_z$  for two different radii are sketched in Figure 3.18.

Matching the Kino impedance would be sufficient, if the same field shape were used in *KlysTOP* as in *Ansys EM*. However, since this is not the case, either the impedance parameter of the FW model or the axial electric field have to be adjusted in order to obtain the correct coupling impedance.

Inspecting Equations (3.11) and (3.15) shows that the Kino and coupling impedance are in fact closely related. This relation is briefly outlined here. When the axial electric field shape  $S(z)$  is normalized such that

$$\int_{-\infty}^{\infty} S(z) dz = 1, \quad (3.33)$$

the gap voltage  $V_1$  is obtained by

$$V_1 = \int_{-\infty}^{\infty} E_z(z) dz = \int_{-\infty}^{\infty} V_\beta S(z) dz = V_\beta, \quad (3.34)$$

where  $V_\beta$  is the electric field amplitude. Calculating the spectrum of the axial electric field leads to

$$E_\beta = \int_{-\infty}^{\infty} V_\beta S(z) \cdot e^{j\beta z} dz \triangleq V_\beta \cdot S_\beta, \quad (3.35)$$

where  $S_\beta$  is the spectrum of the normalized local field shape. Since  $S(z)$  is a localized, non-periodic function in  $z$ , its spectrum is continuous and calculated according to the Fourier transform. Inserting Equation (3.35) into Equation (3.11) leads to

$$R_{c,n}^{EC} = \frac{|E_{\beta_n}|^2}{2\phi_n^2 \cdot P} = \frac{|V_{\beta_n}|^2}{2P} \cdot \frac{|S_{\beta_n}|^2}{\phi_n^2} = R_{\text{Kino}} \cdot F_n, \quad (3.36)$$

### 3 Folded-Waveguide Delay Lines

with  $\phi_n = \beta_n p$ ,  $\beta_n$  the propagation constant of the  $n$ th space harmonic, and  $F_n$  a defined shape factor of the  $n$ th space harmonic. It depends on the dispersion of the delay line and the field shape on the axis. Equation (3.36) gives a relationship between the coupling impedance and the Kino impedance. Additionally, it yields the delay line's coupling impedance assuming the axial field shape  $S(z)$  and a given EC model. The shape factor  $F_n$  describes all frequency dispersion effects related to the field shape and takes into account the distributed nature of the delay line circuit, while  $R_{\text{Kino}}$  includes all network-related effects modeled by the lumped elements.

The representation given in Equation (3.36) is useful, because it allows to extrapolate the coupling from the Kino impedance for any known axial electric field shape and dispersion. Thus, a field shape as in *KlysTOP* can be used, if it is corrected using additional information about the actual coupling impedance. The electric field shape  $S(z)$  can then be scaled at each frequency by

$$\delta_0 = \sqrt{\frac{R_{c,0}^{\text{FW}}}{R_{\text{Kino}} \cdot F_0}}, \quad (3.37)$$

where  $R_{c,0}^{\text{FW}}$  is data supplied from a full-wave solver about the coupling impedance of the fundamental space harmonic and  $R_{\text{Kino}} \cdot F_0$  is the EC coupling impedance of the same space harmonic assuming the field shape  $S(z)$ . The electric field is thus forced to exhibit the proper amount of coupling to the electron beam. All quantities in Equation (3.37) are frequency-dependent.

To illustrate the impact of the field shape used in *KlysTOP*,  $\delta_0$  is plotted over frequency in Figure 3.19 for two different FW delay lines, the parameters of which are given in Table 3.2. For the B-FW line, plotted in blue, it is apparent that a constant scaling factor would be sufficient inside the passband. The strong deviations at the edges of the passband stem from inaccuracies of the dispersion obtained from the EC, where a small error in frequency results in a large error in Kino impedance. Additionally, Equation (3.37) is not applicable when the Kino impedance is infinite, i.e., when the transported power vanishes.

The NC-FW line featuring nose cones (green line) clearly shows the merit of scaling the field shape at each operating frequency. Inside the passband the scaling factor is approximately linear over frequency and varies between 1.25 and 1.6 excluding the effects at the band edges. A constant scaling would lead to an error in coupling impedance for the fundamental space harmonic proportional to  $\delta_0^2$ , i.e., an error between 56 and 156 %.

For both delay lines it is additionally obvious that a scaling, either constant or frequency-dependent, is necessary, because  $\delta_0(f) \neq 1$  throughout the analyzed frequency band. This means that the Kino impedance together with the field shape provided by *KlysTOP* does not exhibit the correct coupling impedance at any frequency point.

### 3 Folded-Waveguide Delay Lines

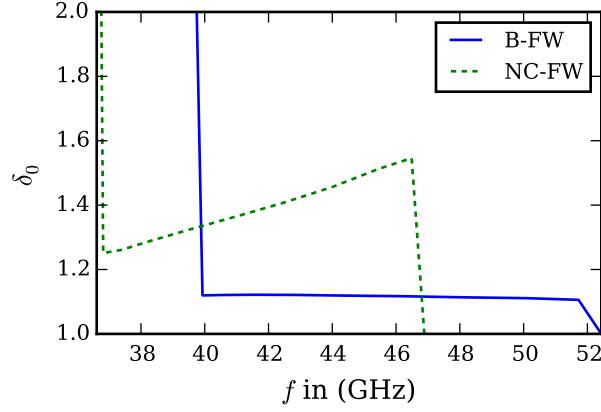


Figure 3.19: Scaling factors for field shapes used in *KlysTOP*.

As an additional note, the actual field shape is less important for tubes with a high accelerating voltage. When the electron's traveling time across the interaction gap is negligibly small, which is the case for either small gaps and/or fast electrons, only the voltage acting on the electrons matters. The envelope of the field simply changes too fast from the point of view of the electrons. For CC-TWTs this holds true, and *KlysTOP* was primarily developed for this kind of tube.

#### 3.3.5 Synthesis of Electric Field Shape

Scaling an existing field shape as in the previous section might yield the correct coupling impedance at each frequency. However, the scaled shape might not be physical and can therefore lead to undesired behavior in an interaction simulation. Also, the scaled field shape yields only correct values for one space harmonic and only inside the passband. It is therefore preferable to define a field shape which is independent of frequency and yields the correct coupling impedance for all space harmonics. Following a method described in [30] a field shape model is derived from a combination of full-wave and EC results.

The periodic longitudinal field  $E_z(z, \beta)$  inside one period  $p$  can be written as

$$E_z(z, \beta) = V_\beta \cdot \sum_{m=-\infty}^{\infty} S(z - mp) \cdot e^{-jm\beta p}, \quad (3.38)$$

where  $V_\beta$  is the field amplitude,  $S(z)$  is a local, frequency-independent, normalized field shape, and a phase progression per period of  $\beta p$  is assumed. Equation (3.38) assumes that the periodic field  $E_z$  is a superposition of the local field shapes at all gaps. On the other hand, the field shape  $S(z)$  at one gap can be obtained from Equation (3.38) with  $m = 0$  and is

$$S(z) = \frac{p}{2\pi} \int_0^{2\pi/p} \frac{E_z(z, \beta)}{V_\beta} d\beta. \quad (3.39)$$

### 3 Folded-Waveguide Delay Lines

Instead of  $E_z(z, \beta)$ , its separation into space harmonics is used for further analysis, i.e.,

$$E_z(z, \beta) = \sum_{n=-\infty}^{\infty} E_n \cdot e^{-j\beta_n z}, \quad (3.40)$$

where  $\beta_n$  is the propagation constant of the  $n$ th spatial harmonic defined by Equation (3.8) and  $E_n$  is the respective complex amplitude according to Equation (3.12). Inserting Equation (3.40) into Equation (3.39), interchanging integration and summation, and rearranging the integrals lead to

$$S(z) = \frac{1}{2\pi} \int_{-\infty}^{\infty} p \frac{E_\beta}{V_\beta} \cdot e^{-j\beta z} d\beta, \quad (3.41)$$

where  $E_\beta$  is the Fourier transform of  $E_z(z)$ . If  $S(z)$  is an even function, then  $E_\beta/V_\beta$  is real and even. Additionally, if  $E_\beta$  decreases with  $\beta$ , Equation (3.41) can be written as

$$S(z) \approx \frac{1}{\pi} \int_0^{\beta_{\max}} p \frac{E_\beta}{V_\beta} \cdot \cos(\beta z) d\beta, \quad (3.42)$$

where  $\beta_{\max}$  is the largest spatial frequency to be taken into account. Equation (3.11) and Equation (3.15) provide information about  $E_\beta$  and  $V_\beta$ , respectively, independently of the transported power. Therefore, Equation (3.42) can be cast into

$$S(z) \approx \frac{1}{\pi} \int_0^{\beta_{\max}} \beta p \sqrt{\frac{R_{c,\beta}}{R_{\text{Kino},\beta}}} \cdot \cos(\beta z) d\beta, \quad (3.43)$$

where  $R_{c,\beta}$  and  $R_{\text{Kino},\beta}$  are the coupling and Kino impedance at  $\beta$ , respectively. For the subsequent synthesis  $R_{c,\beta}$  is computed using full-wave eigenmode results from *Ansys EM*, while  $R_{\text{Kino},\beta}$  stems from Antonsen's EC model for FW delay lines. In this model all impedances are proportional to  $Z_c$  and therefore the gap voltage is proportional to  $\sqrt{Z_c}$ . If we calculate the circuit assuming  $Z_c = 1 \Omega$ , the normalization integral

$$V_S = \int_{-\infty}^{\infty} S(z) dz, \quad (3.44)$$

gives the waveguide impedance

$$Z_c = V_S^2 \quad (3.45)$$

to be used in the model to obtain the correct coupling and Kino impedance with the normalized field shape  $S(z)/V_S$ . This method can be used as an alternative to the fitting procedure for  $Z_c$  outlined in Section 3.3.3.

Care has to be taken, if Equation (3.43) is calculated with a discrete rather than a continuous spectrum. The integral then becomes a sum and repetition field shapes occur according to the frequency separation  $\Delta\beta$  of the samples. This limits the range of  $z$  values where  $S(z)$  is valid.

### 3 Folded-Waveguide Delay Lines

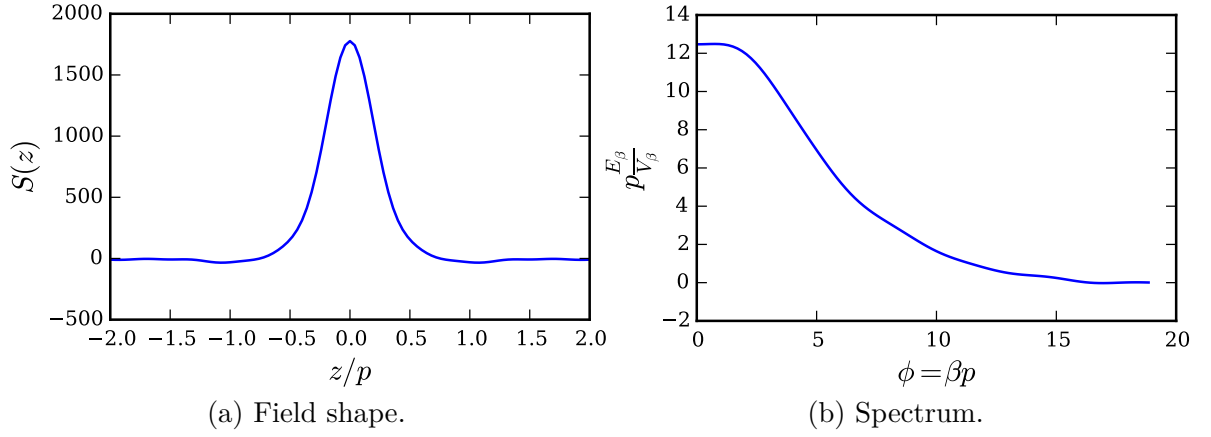


Figure 3.20: Synthesized field shape and spectrum.

For illustration a field shape for the NC-FW structure (Table 3.2) is considered. The resulting unnormalized field shape  $S(z)$  and its spectrum  $pE_\beta/V_\beta$  are shown in Figures 3.20(a) and 3.20(b), respectively. The field shape is strongly localized in the vicinity of the gap. At  $z = \pm p$  the sign of the shape function has changed and its amplitude is only a fraction of the one at  $z = 0$ . Farther away from the gap center, the field shape is already at a negligible level. The rate of decrease depends certainly on the analyzed structure, and is smaller for unit cells that are more strongly coupled. The spectrum in Figure 3.20(b) is indeed band limited. Therefore,  $\beta_{\max}p = 6\pi$  is chosen during the assembly of  $S(z)$ . This value has been found to yield good results for all tested FW lines.

The EC model with the derived field shape is now used to calculate the coupling impedance. It is compared with full-wave results in Figure 3.21(a). The agreement is excellent, and no discernible error appears. Therefore, the relative error is additionally depicted in Figure 3.21(b). Inside the passband it is well below 1% and slightly higher near the band edges. This can be traced back to small deviations in the dispersion between the EC model and eigenmode simulation results. Then a small error in frequency results in a large error in coupling impedance.

## 3.4 Fabrication and Characterization of Folded-Waveguide Delay Lines

The FW structure analyzed in Section 3.2.2 has very small feature sizes down to  $10\ \mu\text{m}$ . It is very challenging to manufacture such a delay line given the high level of accuracy needed to realize the correct phase velocity for TWT applications. An FW structure featuring rectangular nose cones [31, 32] is fabricated in the frame of this work. For ease of manufacturing, the nose cones are only placed on one

### 3 Folded-Waveguide Delay Lines

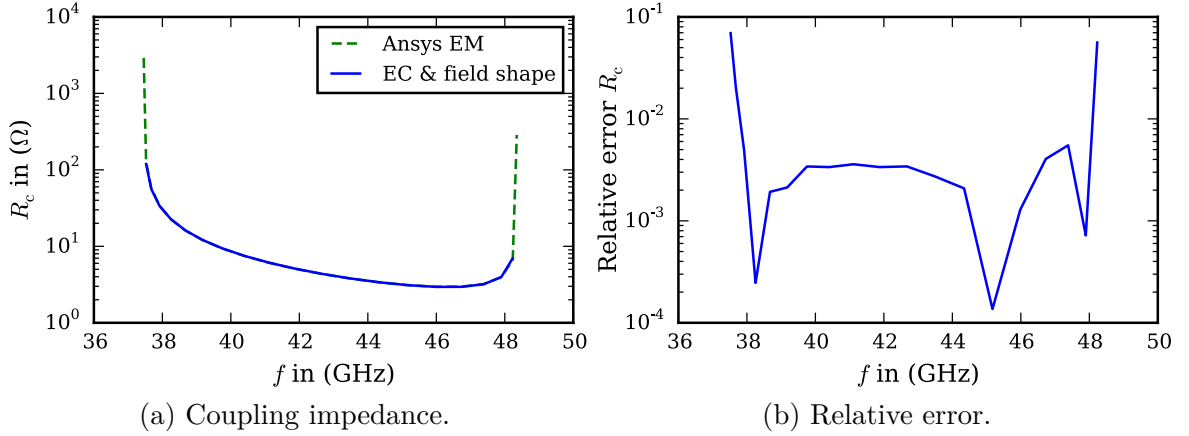


Figure 3.21: Comparison of coupling impedance obtained by *Ansys EM* and equivalent-circuit model with synthesized field shape.

side of the interaction gap. The respective geometry parameters are summarized in Table 3.3. The fabrication process is presented and measurements are evaluated in this section.

#### 3.4.1 Fabrication

The FW delay line is fabricated at *Thales Electronic Systems GmbH*, Ulm, Germany. The process is outlined in Figure 3.22. A block of molybdenum (Mo) is used as bulk material as shown in Figure 3.22(a). A contour is then eroded electrically by a small wire which is subject to high voltage. The large potential difference between the wire and the material leads to discharges that erode the material in the vicinity of the wire. This process is called “electrical discharge machining” (EDM). A constant dielectric liquid flow washes away the debris and serves as conduit for the discharge. The wire runs on a spool and is thus constantly renewed, since the sparks remove material from the wire as well as from the workpiece. A highly accurate two-dimensional profile is obtained using this process (Figure 3.22(b)).

The ridges are then partly milled away from both sides, thus becoming nose cones (Figure 3.22(c)). It might occur that the milling leads to formation of burr at the edges of the nose cones. Care has to be taken to avoid this, because burr can lead to large fields and undesirable electrical effects such as reflections.

Table 3.3: Parameters of the fabricated delay line in (mm).

$p$	$r_t$	$L_s$	$a_{wg}$	$b_s$	$b_g$	$L_{b1}$	$L_{b2}$	$\ell$
1.1	0.35	2.0	3.7	0.9	0.55	0.25	0.0	68.2

### 3 Folded-Waveguide Delay Lines

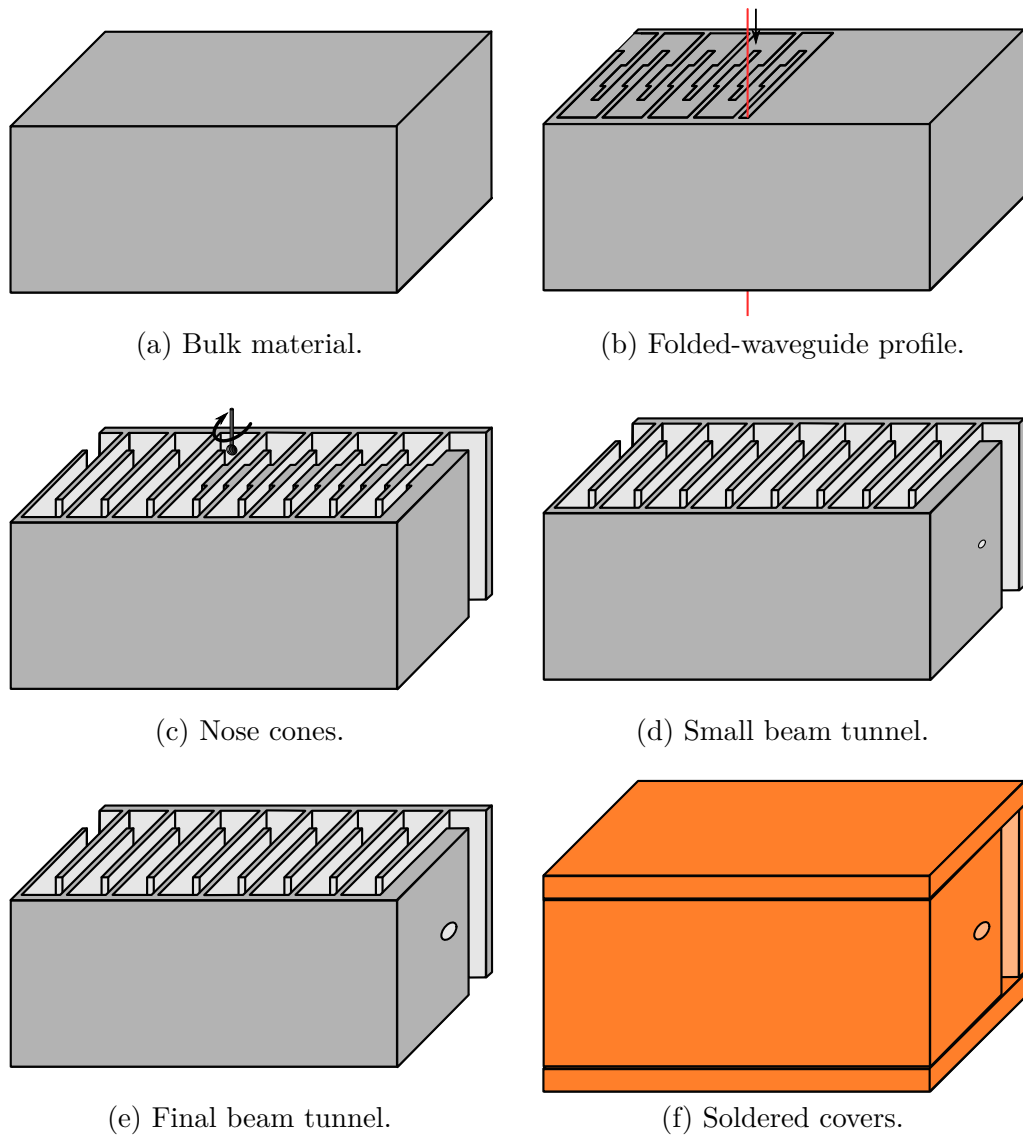


Figure 3.22: Fabrication overview.

After the nose cones are properly milled, the beam tunnel is manufactured. For this purpose, a fine hole is drilled from both sides of the line (Figure 3.22(d)) which is later enlarged by EDM to the proper diameter (Figure 3.22(e)).

Next, the workpieces are acid-cleaned in preparation of the copper-plating process which is necessary to properly solder the side walls onto the center piece (Figure 3.22(f)). After the soldering step, the workpieces are machined to a cylindrical shape to allow later insertion into a measurement flange for electrical characterization.

Four different delay lines were fabricated: two made from Mo, and the other two from a MoCu alloy. Mo has a low thermal expansion coefficient. Mixing it

### 3 Folded-Waveguide Delay Lines

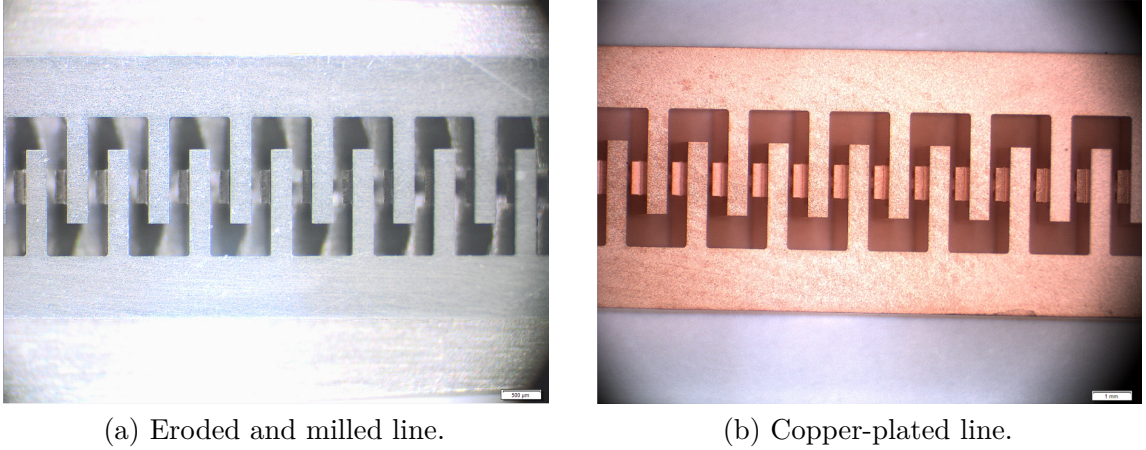


Figure 3.23: Images of intermediate stages of fabrication.

with copper, however, increases the thermal conductivity considerably which is preferable for high-power applications. Therefore both variants were manufactured to compare producibility.

Microscope images of a Mo workpiece before acid cleaning and after copper plating are shown in Figure 3.23. The fabricated lines are characterized optically. The measurement protocol confirms that almost all tolerances could be met, except for one delay line where  $L_b$  exceeds its specified value by approximately  $5\ \mu\text{m}$ . However, this is still an acceptable result. One of the MoCu lines was ruined, because the small holes for the beam tunnel did not meet in the middle of the line. Nevertheless, the workpiece was further processed in order to test the subsequent fabrication steps.

#### 3.4.2 Resonant Measurement

The fabricated delay line is characterized electrically by measuring the fundamental mode phase velocity without evacuation or electron beam (cold measurement).

For the measurement of the dispersion the homogeneous delay line is terminated at both ends by strongly reflecting discontinuities. A ripple is then observable in the measured input reflection spectrum  $\Gamma_{\text{in}}$ . The resonant frequencies can be evaluated to derive the dispersion curve [33]. Starting at the cutoff frequency, minima in the spectrum occur at frequencies where the electrical length is such that destructive interference occurs, i.e.,

$$\beta_0 \ell = n\pi, \quad (3.46)$$

where  $\beta_0$  is the fundamental propagation constant of the periodic line,  $\ell$  is the line length, and  $n$  is the longitudinal mode index. If the line is  $\ell = N_c \cdot p$  long, with  $p$  the pitch and  $N_c$  the number of unit cells, the phase change per unit cell  $\phi$  can be

### 3 Folded-Waveguide Delay Lines

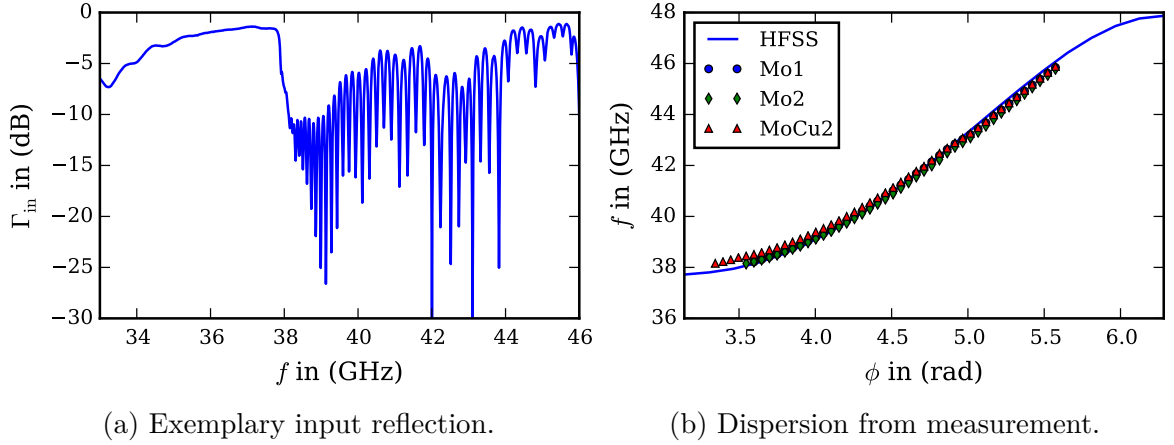


Figure 3.24: Results of resonant measurement.

calculated from [33]

$$\phi = \beta_0 p + \pi = \frac{n\pi}{N_c} + \pi, \quad (3.47)$$

where the additional phase shift of  $\pi$  stems from folding the FW line after each unit cell. The fabricated delay lines have  $N_c = 62$  unit cells.

A sample input reflection spectrum from a one-port measurement is depicted in Figure 3.24(a). The delay line is terminated by an open circuit which reflects strongly. The input coupler also exhibits a pronounced mismatch, because it was actually designed for another delay line at a lower frequency. The cutoff frequency of the delay line is clearly visible at about 38 GHz which agrees very well with the simulation results from *Ansys EM* of  $f_c = 37.8$  GHz. At low frequencies, the ripple period is very small, but changes rapidly over frequency which stems from the underlying dispersion. Close to the cutoff, it is difficult to identify the resonant frequencies as the high attenuation masks the minima, or rather, the attenuation is too high such that interference cannot occur. This is why the first resonant frequencies are not measurable. Each of these missing resonances shifts the dispersion curve by  $\pi/N_c$  (see Equation (3.47)). By extrapolating the frequency spacing between the first visible minima, it can be assumed that six resonant frequencies cannot be observed.

The calculated dispersion of the three fabricated lines (“Mo1”, “Mo2”, and “MoCu2”) is plotted in Figure 3.24(b) together with full-wave eigenmode results from *Ansys EM*. The agreement is very good, especially the lower cutoff is very well verified by all three lines. For the line “MoCu2” three more resonances could be identified. Around  $\phi = 5.0$  there is a small deviation in all measured curves. Starting at approximately 42.2 GHz the  $H_{20}$ -mode of the feed waveguide, which is wider than the measured FW line, can propagate and presumably shifts the measured

### 3 Folded-Waveguide Delay Lines

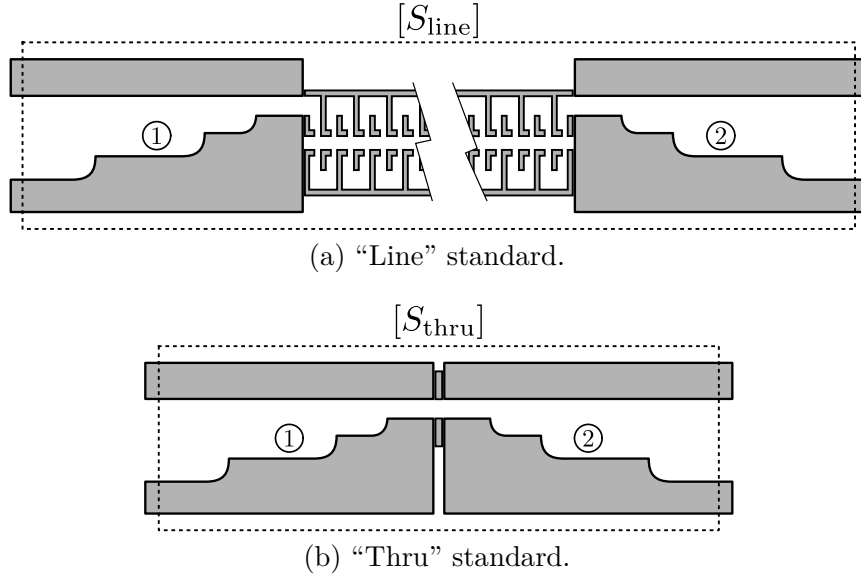


Figure 3.25: Measurement setup of the delay line.

results. The beam tunnel seems to be correctly centered, since a misalignment would lead to a stopband at  $\phi = 3\pi/2 \approx 4.71$ . This stopband, caused by an actual periodicity of twice the gap-to-gap pitch  $p$ , is not observed in any of the fabricated delay lines. Unfortunately, the lines could only be characterized by this method up to 46 GHz due to the measurement setup.

#### 3.4.3 Measurement of Complex Propagation Constant

Since the previous measurements could not be conducted across the whole passband, a different characterization approach is now used that can be evaluated more easily. In general, it is not necessary to obtain the scattering parameters of the delay line under test, since the complex propagation constant is of interest. For this purpose a measurement procedure as in [34] is applied and briefly outlined here.

The measurement setup is depicted in Figure 3.25(a). It requires a calibration standard in addition to the actual delay line. The calibration standard is shown in Figure 3.25(b). For both measurements the vector network analyzer (VNA) is calibrated to the characteristic impedance of the connecting waveguide.

The measured scattering parameters  $[S_{\text{line}}]$  and  $[S_{\text{thru}}]$  can be transformed to the wave cascade parameters  $[T_{\text{line}}]$  and  $[T_{\text{thru}}]$ , respectively [35]. They can be further separated into

$$[T_{\text{line}}] = [T_{\text{steps},1}] \cdot [T_{\text{FW}}] \cdot [T_{\text{steps},2}] \quad \text{and} \quad (3.48)$$

$$[T_{\text{thru}}] = [T_{\text{steps},1}] \cdot [T_{\text{steps},2}], \quad (3.49)$$

### 3 Folded-Waveguide Delay Lines

where  $[T_{\text{FW}}]$  is the cascade matrix of the FW delay line, and  $[T_{\text{steps},1}]$  and  $[T_{\text{steps},2}]$  are the cascade matrices of the input and output stepped transformers, respectively. Multiplying  $[T_{\text{line}}]$  by the inverse of  $[T_{\text{thru}}]$  results in

$$[T_{\text{line}}] [T_{\text{thru}}]^{-1} = [T_{\text{steps},1}] \cdot [T_{\text{FW}}] \cdot [T_{\text{steps},1}]^{-1}. \quad (3.50)$$

The matrices  $[T_{\text{line}}] [T_{\text{thru}}]^{-1}$  and  $[T_{\text{FW}}]$  are mathematically similar and thus exhibit the same trace. A homogeneous piece of TL of length  $\ell$  has a cascade matrix of the form

$$[T] = \begin{pmatrix} e^{-\gamma\ell} & 0 \\ 0 & e^{+\gamma\ell} \end{pmatrix}, \quad (3.51)$$

where  $\gamma = \alpha + j\beta$  is the complex propagation constant with attenuation constant  $\alpha$  and phase constant  $\beta$ . Therefore, the complex propagation constant can be computed from

$$\gamma = \frac{\text{arcosh} \left( 0.5 \cdot \text{trace} \left( [T_{\text{line}}] [T_{\text{thru}}]^{-1} \right) \right)}{\ell}. \quad (3.52)$$

The two stepped impedance transformers in waveguide technology are connected to the VNA and the FW line via flanges. The transformers are optimized in *Ansys EM* to exhibit a low reflection across the passband. In the “thru” standard the same transformers are used. However, a short piece of waveguide with the same cross section as the input of the FW line ( $3.7 \times 0.9 \text{ mm}^2$ ) is placed between the transformers instead of the delay line. Therefore, the influence of the change in waveguide width is also included in the calibration. For the “line” and “thru” measurements the same transformers are used, i.e., after one measurement they are disconnected from the setup and reused for the other. This immensely improves the accuracy of the approach. Otherwise, mechanical inaccuracies during the manufacturing of the waveguide components would deteriorate the measurement results, because the cascade matrices would be different and would therefore not cancel out as in Equation (3.50).

The measured S-parameters for the “line” and “thru” setup are shown in Figures 3.26(a) and 3.26(b), respectively. The passband is clearly visible in the “line” measurement. The stepped transformers yield low reflections across the band for both the “line” and the “thru” setup.

From these results the complex propagation constant  $\gamma = \alpha + j\beta$  can be derived by applying Equation (3.52) with  $\ell = 62p = 68.2 \text{ mm}$ . The phase constant  $\beta$  calculated from the imaginary part of the inverse cosine hyperbole is ambiguous by increments of  $2\pi$ . This is corrected by minimizing

$$\text{RMS}_{\beta\ell} = \left[ (\beta\ell)^{\text{HFSS}} - \left( (\beta\ell)^{\text{Meas}} + 2\pi n \right) \right]^2 \quad (3.53)$$

inside the passband and with an integer  $n$ . The real part of  $\gamma$  is uniquely defined and needs no further processing. The results for  $\beta$  and  $\alpha$  are shown in Figures 3.27(a)

### 3 Folded-Waveguide Delay Lines

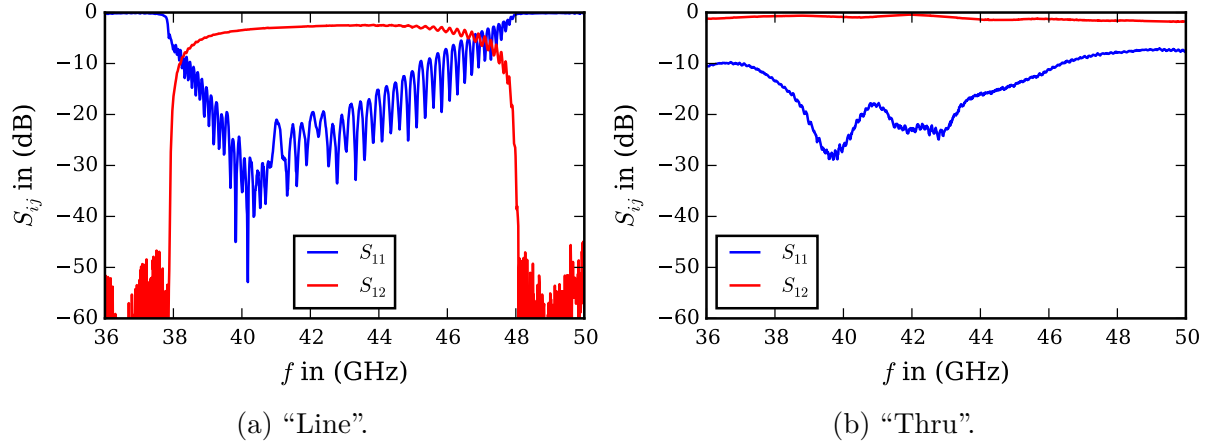


Figure 3.26: Measurement results for line "Mo2".

and 3.27(b), respectively. In Figure 3.27(a) the obtained results are additionally compared with the eigenmode results. The agreement is excellent with deviations of less than 1% across the passband. Only the lower cutoff frequency for "MoCu2" and at the upper one for "Mo2" and "MoCu2" exhibit slightly larger discrepancies. The attenuation over frequency in Figure 3.27(b) is also quite similar for all lines. They exhibit a relatively low attenuation of approximately 0.5 dB/cm. There are some artificial peaks in Figure 3.27(b) due to the evaluation algorithm, presumably when the transmission through the delay line is low. Small peaks around 42 GHz are proof of slight asymmetries of the electron beam tunnel that could not be identified with the resonant measurement setup. If the beam tunnel would be off-centered, a stopband would occur at this frequency. The placement of the beam tunnel seems to be acceptable for all manufactured lines, since the dispersion in Figure 3.27(a) shows no discernible stopband.

The obtained attenuation  $\alpha$  has an order of magnitude comparable to that of typical helical delay lines in this frequency range which exhibit approximately 0.1 dB of attenuation per wavelength. Therefore, it should be relatively easy to extract the amount of loss-induced heat, since the FW delay line consists of bulk metal. An accurate thermal prediction calls for involved multi-physics simulation and is outside the scope of this thesis. However, the distribution of the surface current in the lossless case can be used to estimate the impact of the nose cones on the power loss distribution. The edges of the nose cones might lead to strongly increased electric field and surface current density amplitudes. The distribution of the latter obtained by eigenmode simulation with and without nose cone is compared for this purpose. The maximum surface current density along the center of the FW line is slightly increased by 10% due to the nose cones. This means that local power

### 3 Folded-Waveguide Delay Lines

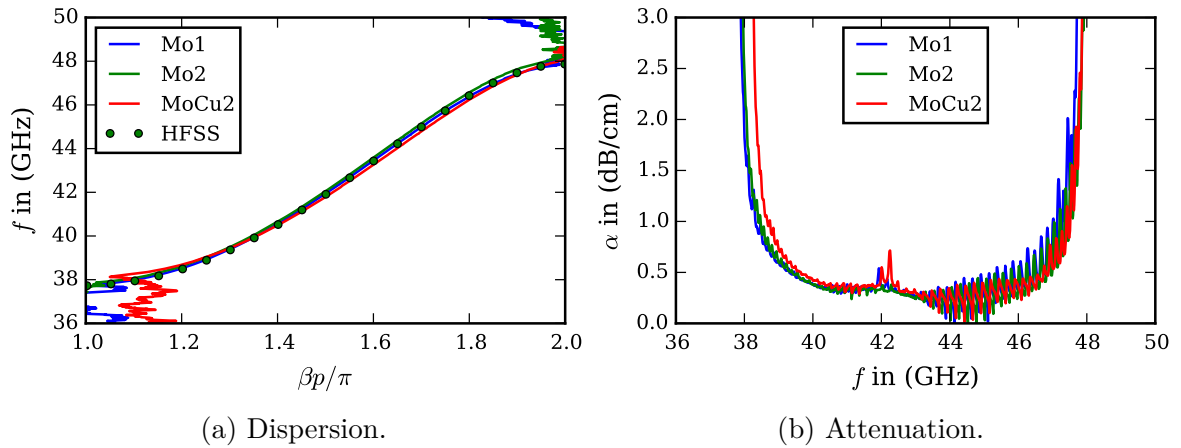


Figure 3.27: Comparison of derived propagation constants.

conversion is only marginally changed, not taking the slightly longer path length into account.

The obtained results verify the reproducibility and feasibility of nose-cone loaded FW lines. Additionally, the agreement with full-wave results confirms the field enhancement achieved by means of the nose-cone topology.

# 4 Matching for Cold and Hot Operation

In Section 3.3.2 models for delay lines with ideally matched couplers and severs have been introduced. The ideal matching condition was derived from the characteristic impedance of the delay line circuit. Coupling the delay line to an electron beam, however, changes the propagation constant and characteristic impedance of the line [36, 37]. In the following, all quantities related to the first case are denoted as cold, while those related to the latter case are referred to as hot. The approach outlined in [36, 37] is applied here to an FW-TWT. Alternative modeling approaches of space-charge induced reflections and hot operation can be found in [38, 39].

## 4.1 Dispersion of the Coupled System

For the subsequent analysis, the coupled beam-wave system is assumed to be a periodic structure so that considering a single unit cell is sufficient to derive characteristic quantities. In order to determine the impact of an electron beam coupled to the delay line, a beam model similar to the one presented in Section 2.2.2 is used. The modulation of the beam is thus modeled by velocity and space-charge density amplitudes,  $u$  and  $\rho$ , that are assumed to be small with respect to their DC counterparts.

This description of the electron beam is coupled to the EC model of the FW line outlined in Section 3.3. All in all, a four-by-four transmission matrix can be set up to relate the relevant signals in one plane of the periodic unit cell to those in the other. This yields

$$\begin{pmatrix} V_3 \\ -I_3 \\ u_b \\ \rho_b \end{pmatrix} = [T_c] \cdot \begin{pmatrix} V_2 \\ I_2 \\ u_a \\ \rho_a \end{pmatrix}, \quad (4.1)$$

where  $V_{2,3}$  and  $I_{2,3}$  denote the voltages and currents at the respective ports, and  $u_{a,b}$  and  $\rho_{a,b}$  are the amplitudes of velocity and charge density modulation in the respective planes. The coupled unit cell is illustrated in Figure 4.1, where  $[Z]$  indicates the three-port impedance matrix of the delay line unit cell. Rotational symmetry of the beam tunnel region is assumed.

#### 4 Matching for Cold and Hot Operation

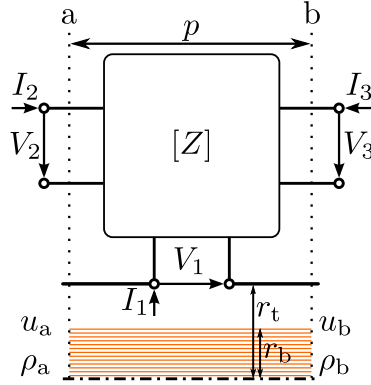


Figure 4.1: Schematic of coupled beam-wave unit cell.

The transfer matrix of the coupled system  $[T_c]$  is obtained numerically by evaluating the interaction of the delay line and the electron beam in one unit cell. The axial electric field shape, as described in Section 3.3.4, is crucial in this analysis, because it defines the coupling between the two systems. It determines the field the beam is subjected to (Equation (2.9)) and also the current induced in the delay line (Equation (2.19)). The field shape of *Klystron* discussed in Section 3.3.4 is used for the following analysis. Once the matrix  $[T_c]$  is set up, the eigenvalue problem

$$[T_c] \cdot \begin{pmatrix} V_2 \\ I_2 \\ u_a \\ \rho_a \end{pmatrix} = \psi \cdot \begin{pmatrix} V_2 \\ I_2 \\ u_a \\ \rho_a \end{pmatrix} \quad (4.2)$$

is solved numerically. Again, as in Section 3.3.1, the eigenvalues and -vectors can be interpreted physically. The phase (magnitude) of the complex eigenvalue  $\psi$  corresponds to the phase shift (gain) per unit cell. Forward and backward traveling modes can be distinguished and amplification can be identified by evaluating the eigenvalues and -vectors. This way a coupled, or hot, characteristic impedance can be defined.

Four modes exist in the coupled system, since each  $(n \times n)$  matrix has exactly  $n$  eigenvalues including algebraic multiplicity. The same number of coupled modes is found from the solution of the determinantal equation as in Section 2.2.3. Depending on the synchronism, these modes are more or less tightly bound to the delay line. For example, when EM wave and electron beam are not synchronized, there are two modes on the delay line (forward and backward traveling mode) and two on the electron beam (slow and fast space-charge mode). For normal TWT interaction as discussed in Section 2.2.3 these modes couple and there are three forward traveling modes, one fast and two slow ones, in addition to a backward traveling mode. One of the slow modes grows exponentially, i.e., the operating mode of a TWT, while the other one decays.

#### 4 Matching for Cold and Hot Operation

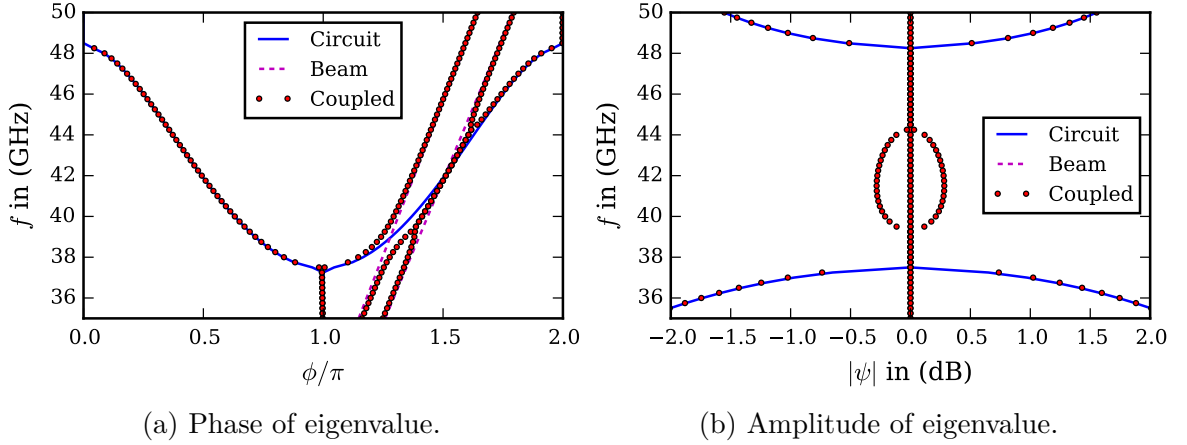


Figure 4.2: Comparison of uncoupled (“Circuit” and “Beam”) and coupled dispersion curves.

Sweeping over the operating frequency and solving the eigenvalue problem in Equation (4.2) results in the dispersion curves shown in Figure 4.2 for the uncoupled (red and blue lines) and coupled case (red dots). In this example, the EC parameters of the nose-cone loaded line (NC-FW in Table 3.2) are used and coupled to a beam with  $V_0 = 12.5$  kV,  $I_0 = 0.4$  A, and  $r_b = 0.25$  mm. Figure 4.2(a) depicts the operating frequency  $f$  over the phase  $\phi$ , while Figure 4.2(b) shows the operating frequency  $f$  over the magnitude  $|\psi|$  of the eigenvalues. Without synchronism the modes propagate independently as in the uncoupled case. Inside the passband the circuit mode propagates without attenuation (lossless case), and outside the modes are evanescently damped. The space-charge modes are undamped at any frequency. When the slow beam mode and forward traveling mode have approximately the same phase velocity, two coupled modes with the same phase constant exist (Figure 4.2(a)). One of these modes has a growing, the other one a decaying amplitude as can be seen in Figure 4.2(b). This frequency range is denoted as the amplification bandwidth in the following. It ranges from approximately 39 to 44 GHz in this case.

Identifying the modes from the eigenvalue problem is not straightforward, especially when done over a broad range of frequencies exceeding the amplification bandwidth or even the cold passband. A mere check of, e.g., the magnitude  $|\psi|$  is not sufficient, because an evanescent backward mode also exhibits  $|\psi|$  larger than unity, similarly to an amplified forward mode. The transported power has to be taken into account to identify the modes properly. Even with this consideration the coupled modes can only be identified by taking the electron beam parameters into account. For example, if the beam is synchronous with the backward traveling mode, a narrowband phenomenon known as backward-wave oscillation may occur [11].

## 4 Matching for Cold and Hot Operation

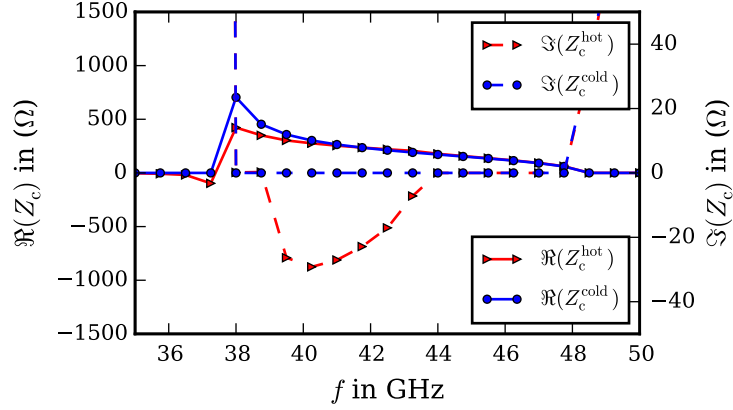


Figure 4.3: Comparison of cold and hot characteristic impedance.

The interpretation of the eigenvalues and -vectors is fundamentally different for this kind of beam-wave interaction.

The characteristic impedance of the coupled system, or hot characteristic impedance, is calculated by relating the voltage  $V_{\text{amp}}$  to the current  $I_{\text{amp}}$  of the amplified forward mode of the coupled system, i.e.,

$$Z_c^{\text{hot}} = \frac{V_{\text{amp}}}{I_{\text{amp}}}. \quad (4.3)$$

A comparison between the hot and cold characteristic impedance  $Z_c^{\text{hot}}$  and  $Z_c^{\text{cold}}$  is shown in Figure 4.3. Again, the delay line is assumed to be lossless. Figure 4.3 shows that for non-synchronous operation both impedances are essentially the same. Inside the cold passband they are purely real (no losses), and outside purely imaginary (evanescent mode). However, for frequencies inside the amplification bandwidth the hot characteristic impedance is obviously different. The real part is slightly modified and an imaginary part appears due to the beam. The imaginary part is one order of magnitude smaller than the real part. This fact and the small change of the real part illustrate the relatively weak coupling of circuit and beam modes despite the nose-cone loaded delay line. A similar analysis of a CC-TWT as in [40] shows a stronger change of the hot characteristic impedance due to the stronger beam-wave coupling for this delay line topology.

## 4.2 Influence of Matching for Hot Operation

Optimization of couplers and severs is in practice commonly performed based on the characteristics of the cold delay line. As is well known, an ideal match for cold operation does not result in optimum operating conditions of the active device, i.e., with an electron beam. Therefore, it is worthwhile to study the impact of

matching for cold and hot operation using the abstract models for couplers and severs presented in Section 3.3.2. Figure 4.3 suggests that the amplified forward mode experiences a mismatch, if the tube is terminated by the cold characteristic impedance. Depending on the gain and the magnitude of the reflection this can lead to instabilities and a gain ripple over frequency. These effects are studied in the following.

### 4.2.1 Stability

Three main causes can be identified for instabilities in vacuum tubes: backward-wave, drive-induced, and regenerative oscillations [41]. The first type, as mentioned above, depends mainly on the operating point of the tube and can be observed without any input signal. For helices this type of oscillation occurs mostly for large beam radii and can be tuned by changing the accelerating voltage  $V_0$  of the tube [11]. The second oscillation type is a large-signal phenomenon. A tube that is zero-drive stable, or even stable under small-signal conditions, may start to oscillate when the input power is increased. Figuratively, the electrons become slower and thus the electron beam line may intersect the dispersion curve close to a band edge at  $\phi = \pi$  or  $\phi = 2\pi$ . Because the coupling can be high at these frequencies and power cannot propagate, the tube may start to oscillate [41]. Instabilities of the third type occur due to mismatches along the TWT delay line with an amplifying path in between, essentially leading to a loop gain larger than unity. In the following the focus is on oscillations of this type.

These oscillations can be described by means of control theory as an unstable control loop with a loop gain (expressed in dB)

$$g_{\text{loop}} = \Gamma_1 + \Gamma_2 + G + B > 0, \quad (4.4)$$

where  $\Gamma_i, i = 1, 2$ , are reflection coefficients at delay line discontinuities, and  $G$  and  $B$  are amplification coefficients (including loss) in forward and backward direction, respectively.

In a linear beam device such as a TWT, the feedback path is created by discontinuities along the line, e.g., by couplers and severs. The distributed nature of the TWT results in the formation of resonant frequencies at which the oscillations occur. For an inhomogeneous delay line this is more involved, because the dispersion changes along the line.

A TWT with homogeneous delay line is therefore studied in this section to demonstrate the impact of matching for hot operation only, i.e., without any additional effects. The EC and beam parameters from Section 4.1 are used here to illustrate the impact of input and output matching on stability. A generic, lossless TWT with one section and  $N_c = 25$  cells is simulated using the small-signal version of *KlysTOP* with couplers exhibiting a specified reflection. A sketch of

#### 4 Matching for Cold and Hot Operation

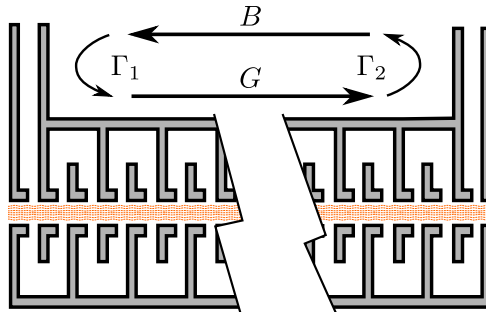


Figure 4.4: Sketch of a single-section folded-waveguide traveling-wave tube with signal paths indicated.

the interaction space of the considered tube is shown in Figure 4.4. A signal flow chart is included in the figure for convenience. The backward mode experiences a mismatch  $\Gamma_1$  at the input coupler and the amplified forward mode is reflected at the output coupler assuming a reflection of  $\Gamma_2$ . For simplicity  $\Gamma_1 = \Gamma_2 = \Gamma$ ,  $\Gamma \in [0, 1]$ , is assumed in the following.

The calculated small-signal gain  $G_{ss}$  of the tube is depicted in Figure 4.5(a) for several values of  $\Gamma$ . An ideal match for hot operation, i.e.,  $\Gamma = 0$ , yields a smooth gain curve. Increasing the local reflection at the couplers leads to the formation of local maxima and minima, i.e., a gain ripple. Its period  $\Delta f$  is determined by the length and dispersion of the delay line, while its amplitude  $\Delta G$  depends on the magnitude of  $\Gamma$ . The respective input reflections for the different matching conditions are shown in Figure 4.5(b). It can be clearly observed that the amplifier gain as well as the hot input reflection grow indefinitely for  $\Gamma = 0.4$  ( $\approx -8$  dB) at discrete frequencies. The maximum stable gain can be calculated from Equation (4.4) for a given reflection  $\Gamma$ . Taking into account the loss of the delay line relaxes the stability limit, because loss effectively decreases the loop gain.

Further conclusions can be drawn from Figure 4.5(b). A perfect match for the amplified forward mode results in non-zero hot input reflections. The other two forward modes that are inevitably excited at the input coupler of the TWT [11] experience a mismatch, while the amplified mode does not. The main contribution to the input reflection stems from the fast forward mode, because the other slow mode is exponentially damped and therefore has a negligible amplitude at the end of the tube. On the other hand, a small reflection for the operating mode, e.g.,  $\Gamma = 0.1$ , already leads to a significantly larger input reflection, because this mode is amplified. The mismatch at the end is thus magnified by the amplification. Matching the amplified forward mode is consequently the optimum load condition in terms of stability.

Furthermore, it is obvious that a perfect match for hot operation can only be obtained if the TWT is mismatched in the cold case with a specific load condition.

## 4 Matching for Cold and Hot Operation

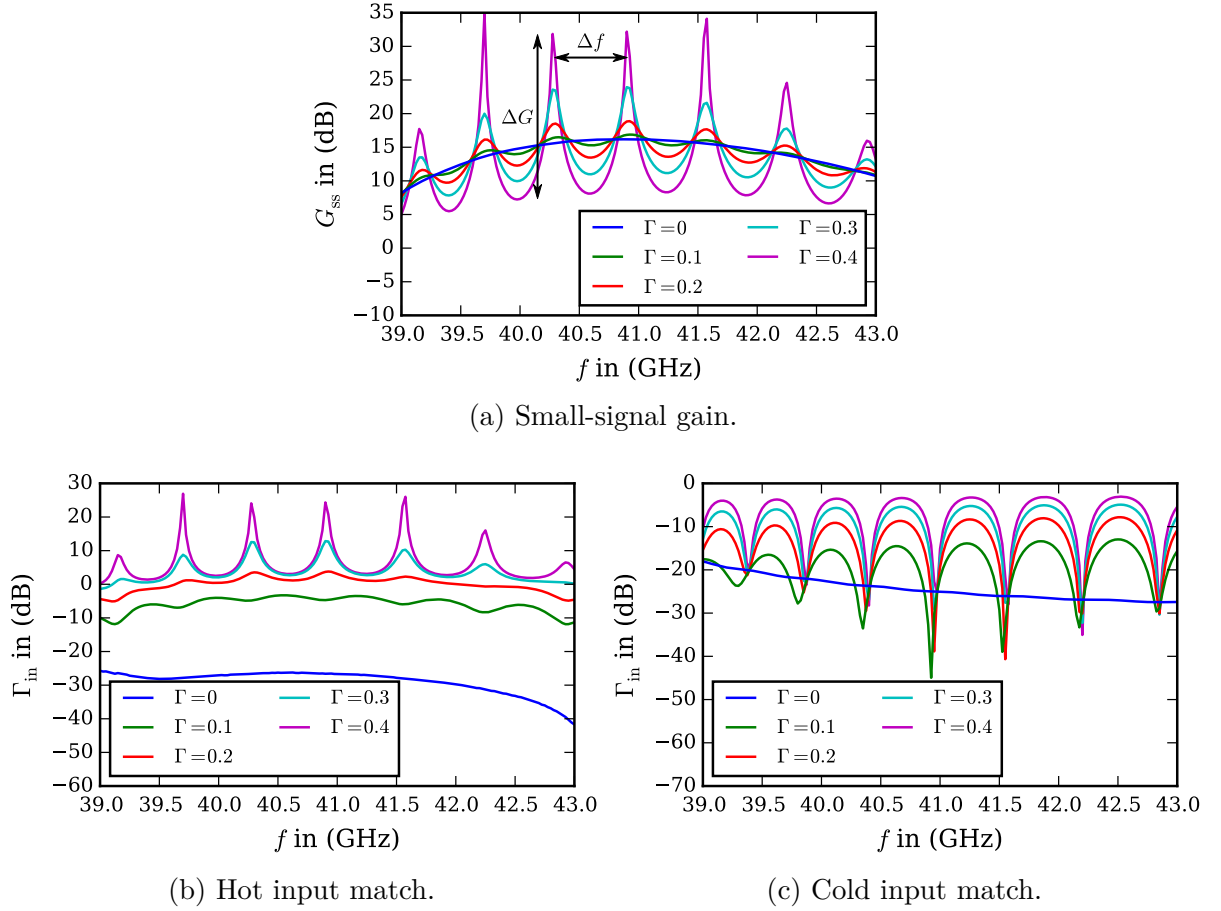


Figure 4.5: Comparison of input match and gain for different levels of input and output coupler reflection  $\Gamma$ .

This can be observed in Figure 4.5(c) which shows the cold input reflection for the different cases. The reflection at the end of the tube has to exhibit the proper amplitude and phase for minimum hot input reflection. Additionally, the ideal load condition depends on the electron beam, i.e., accelerating voltage  $V_0$  and beam current  $I_0$ , as well as on the operating frequency  $f$  of the tube.

### 4.2.2 Large-Signal Behavior

The derivation of the coupled characteristic impedance is performed using a small-signal approach. The derived matching condition for hot operation is now applied to the single-section TWT of the previous section at an operating frequency  $f = 40.5$  GHz for maximum gain and the input power is changed to analyze how the reflection is altered. The large-signal version of *Klystron* is used for this analysis. As before, the input coupler and output coupler are assumed to be perfectly matched to the backward and amplified forward mode, respectively.

## 4 Matching for Cold and Hot Operation

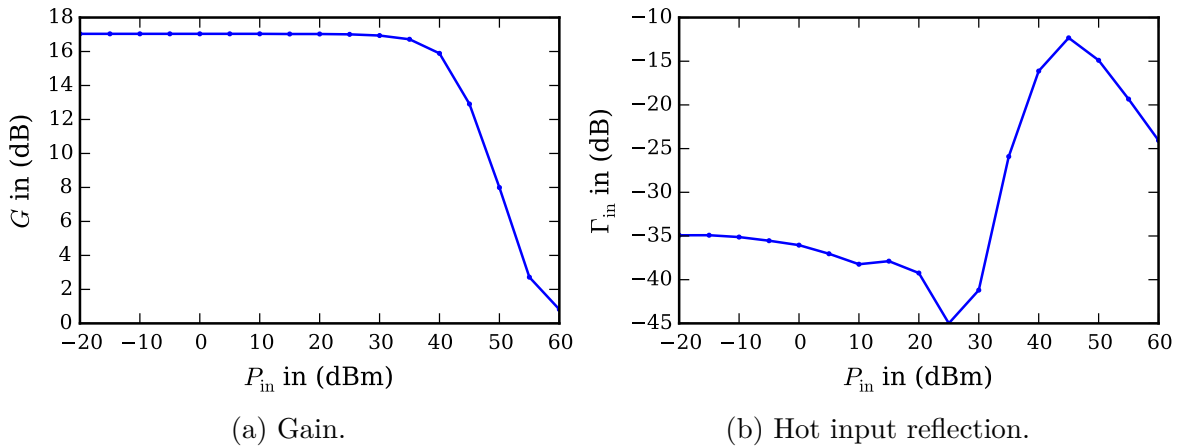


Figure 4.6: Results at  $f = 40.5$  GHz for different input power levels  $P_{in}$ .

Figure 4.6 summarizes the obtained results. Figure 4.6(a) shows the gain over input power at 40.5 GHz. Relatively large input powers are necessary to drive the tube into the nonlinear regime, since the tube has only 25 cells. For input powers up to 30 dBm the amplifier is linear. For higher powers the gain drops drastically. The respective hot input reflection is depicted in Figure 4.6(b). For small input powers the match is very good with reflections smaller than  $-30$  dB. In the nonlinear regime the input reflection rises up to  $-12$  dB. The electrons are then strongly modulated and have lost a non-negligible portion of their kinetic energy. This shifts the synchronism to higher frequencies and thus changes the propagation and ideal matching condition for hot operation at the operating frequency. In a real tube this knowledge could be used to optimize the load of the amplifier for a specific output power.

### 4.3 Sever Topology for Hot Operation

In the previous section the reflection at couplers and severs could be arbitrarily changed by assuming ideal transformers and loads. This is especially useful to test a delay line concept without directly modeling the additional components. However, for a real tube physical concepts must be developed. Knowledge of the coupled characteristic impedance can be helpful to design a sever exhibiting the proper amount of reflection in the cold case in order to improve its performance under hot operating conditions.

When considering a physical realization of couplers and severs, the matter is even more involved than in the EC model, especially under large-signal conditions. In case of output couplers, for example, the interaction is strongly nonlinear and a prediction of the impedance of the coupled system becomes very difficult.

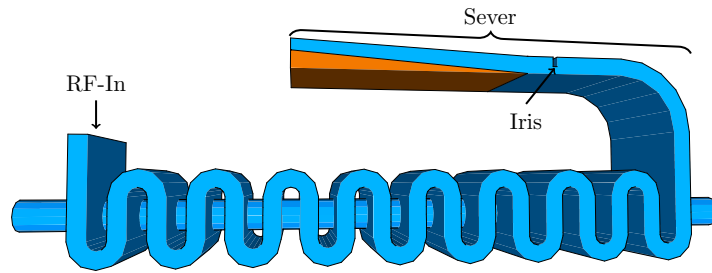


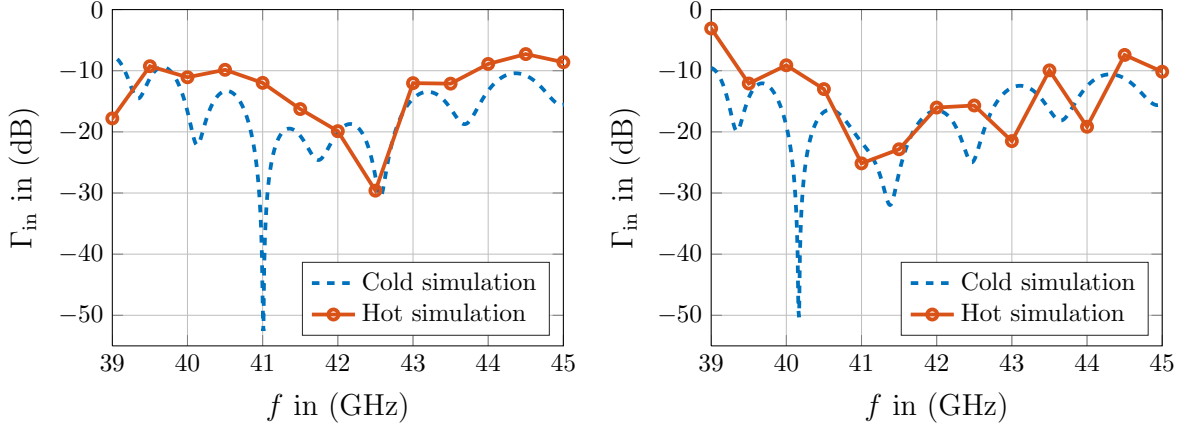
Figure 4.7: Sever topology for serpentine-waveguide delay lines from [42].

Additionally, the load of the TWT plays a major role then, because the possible feedback directly influences the interaction inside the tube. To simplify the analysis, an input section of a TWT with a serpentine delay line is considered here, where interaction is essentially linear. The input coupler can be expected to exhibit the same reflection coefficient as for cold operation, even with electron beam. The space-charge waves are not yet present at the input coupler and therefore do not contribute to a mismatch. Additionally, the broadband characteristic of the SW delay line facilitates the design. The sever of the input section is the component to be optimized in the following. The optimization is performed at a single, arbitrarily chosen frequency inside the delay line passband. This limitation is accepted in order to prove the concept of matching for hot operation with a physical sever topology. It is well understood that a broadband optimization is desirable in practice. With the above mentioned constraints, the optimization of a sever at the end of an input section becomes feasible.

A design strategy for severs in FW-TWTs with a conventional serpentine delay line has been developed in [42, 43]. A 3D structure is proposed that is easy to integrate into a TWT topology and design strategies for cold and hot operation are evaluated. A perspective view of such a sever integrated into the input section of an FW-TWT is depicted in Figure 4.7. Vacuum is shown in blue and lossy dielectric material in orange. The background material is PEC. After the last gap of the SW delay line a smooth E-plane bend guides the signal into the damping element of the sever. A small iris mainly determines the imaginary part of the sever load, while the real part stems from the tapered lossy dielectric. Since the sever input impedance is very sensitive to the opening of the iris, the height of the waveguide and that of the dielectric material at the end of the sever serve as tuning parameters. Optimization leads in general to a wedge-shaped waveguide at the end of the sever.

Information about the cold delay line extracted from full-wave simulation can be used to obtain an ideal cold match at a single operating frequency [42]. This is, however, not optimum for hot operation as has been pointed out earlier in this chapter. Knowledge about the coupled characteristic impedance is only available from the small-signal computation and cannot be used directly to determine the

#### 4 Matching for Cold and Hot Operation



(a) Sever matched for cold operation.

(b) Sever matched for hot operation.

Figure 4.8: Cold and hot input reflection for different sever designs [43].

necessary load reflection. The reference impedance changes from the FW delay line to the RW of the sever. In the EC, however, only impedance information is available. Nevertheless, the ideal load condition for hot operation can be an indication in what direction the sever input impedance, or reflection coefficient, has to be changed to reduce the mismatch at the input of the FW line. For this reason a full-wave optimization is necessary to obtain minimum input reflection. Since a 3D sever structure is sought, a 3D simulation tool is necessary to perform this optimization, e.g., *CST Particle Studio* which is commercially available and has a full-wave particle-in-cell (PIC) solver.

A comparison of input reflections  $\Gamma_{in}$  for sever designs optimized for cold and hot operation is shown in Figure 4.8. The design goal is a minimum input reflection at the arbitrarily chosen operating frequency of 41 GHz. The results of the sever optimized for cold operation are depicted in Figure 4.8(a) and include the cold and hot input reflection. As designed, the cold input reflection is minimum at 41 GHz. During hot operation with only a small input power ( $-20$  dBm), however, the match at this frequency deteriorates and the position of the minimum is shifted to 42.5 GHz. An input reflection lower than  $-10$  dB is obtained between 40.5 and 43.5 GHz.

After redesigning the sever using the hot characteristic impedance as indication, the results in Figure 4.8(b) are obtained. The cold input reflection is still relatively low, but obviously different compared to the previous design. However, for hot operation the minimum input reflection appears at the specified design frequency. Additionally, the input reflection is relatively low ( $< -10$  dB) between 40 and 43.5 GHz.

#### *4 Matching for Cold and Hot Operation*

It can be seen that the results of the optimization exhibit good properties at the specified design frequency. The bandwidth of this solution is difficult to control, however, because it depends on the dispersion of both the delay line and the electron beam. However, regarding the constraints given at the beginning of this section, a proof of concept was presented to match under hot operating conditions by exploiting small-signal beam-wave interaction results for a physical sever design.

# 5 General Interaction Simulation

In this chapter the general approach of *KlysTOP* to solve the nonlinear interaction problem is outlined. A Broyden iteration algorithm is implemented and initialization schemes are tested to accelerate the convergence.

## 5.1 Nonlinear Multidimensional Root Problem

*KlysTOP* calculates the interaction between EM wave and electron beam for sinusoidal excitation and is thus a frequency-domain tool. For this purpose the interaction problem is subdivided into two parts: the RF fields on the delay line and the electrons inside the drift tube. The fields on the delay line are projected onto a set of ECs that render their dispersive characteristics. The electron beam is modeled in one of two ways. For small input powers it can be modeled by a set of differential equations, similar to the ones discussed in Section 2.2.2. For large input powers, however, a PIC approach is incorporated by injecting particles into a discretized computational domain and solving the equation of motion subject to external and space-charge fields at each time step. The first description is one-dimensional, while the latter is a 2.5D approach, since the grid is two-dimensional and cylindrical symmetry is implicitly assumed.

The RF fields and the electron beam influence each other, i.e., they form a coupled system. The RF wave creates axial electric fields that modulate the electron velocity and space-charge density. The electrons, on the other hand, induce RF currents on the delay line that excite forward and backward traveling waves. Both procedures happen at the same time and for stationary TWT operation they are balanced.

In the chosen approach this coupled nonlinear problem is solved iteratively. One part of the problem is calculated assuming the other one to be fixed. Afterwards, the other part is updated under the assumption that the first one is constant. This process is repeated until consistency is reached, i.e., the results do not change from one iteration to the next. Mathematically this process can be written as

$$x_{k+1} = h(x_k), \tag{5.1}$$

where  $x_k$  is a state of the coupled system at iteration  $k$  and  $h(x)$  is some nonlinear function. The convergence of Equation (5.1) depends strongly on the properties of  $h(x)$ . In *KlysTOP* the state  $x$  corresponds to a set of voltages and is thus a vector. Therefore,  $h(x)$  is a nonlinear and vector-valued function.

## 5.2 Formulation of *KlysTOP* Algorithm

The general approach of *KlysTOP* is outlined in the following. The interaction simulation domain for the whole TWT can be separated into the individual sections. The sections are only coupled via the modulated electron beam. If the beam at the end of one section is known, it can be used as input for the next section. The voltages  $\mathbf{V}$  at the gaps in one section are related to the induced currents  $\mathbf{I}$  via

$$\mathbf{V} = [Z_g] \cdot \mathbf{I} + \mathbf{V}_{\text{rf}}, \quad (5.2)$$

where  $[Z_g]$  is the gap impedance matrix and  $\mathbf{V}_{\text{rf}}$  the voltage distribution without induced currents that stems from the RF input signal. It is therefore zero for all sections except the first one.

In a similar fashion, the induced currents  $\mathbf{I}$  can be formulated as a function of the gap voltages  $\mathbf{V}$ . However, this relation is in general nonlinear and can be written as

$$\mathbf{I} = [Y_b(\mathbf{V})] \cdot \mathbf{V} + \mathbf{I}_{\text{mod}}, \quad (5.3)$$

where  $[Y_b(\mathbf{V})]$  is the nonlinear beam admittance matrix and  $\mathbf{I}_{\text{mod}}$  the current distribution without gap voltages, i.e., due to prior beam modulation. It is therefore zero for the first and non-zero for all subsequent sections.

Inserting Equation (5.3) into Equation (5.2) leads to the relationship

$$\mathbf{V} = [Z_g] \cdot [Y_b(\mathbf{V})] \cdot \mathbf{V} + [Z_g] \cdot \mathbf{I}_{\text{mod}} + \mathbf{V}_{\text{rf}}, \quad (5.4)$$

which cannot be solved explicitly for  $\mathbf{V}$ , because  $[Y_b]$  depends on  $\mathbf{V}$ . Equation (5.4) can be formulated as a fixed-point iteration

$$\mathbf{V}_{k+1} = [Z_g][Y_b(\mathbf{V}_k)] \cdot \mathbf{V}_k + [Z_g] \cdot \mathbf{I}_{\text{mod}} + \mathbf{V}_{\text{rf}}, \quad (5.5)$$

where  $k$  is the iteration index. The convergence of Equation (5.5) depends on the eigenvalues of  $[Z_g] \cdot [Y_b(\mathbf{V}_k)]$ . Even for a linear problem, i.e.,  $[Y_b]$  being constant, Equation (5.5) does not converge in general, since the eigenvalues vary strongly with frequency due to the impedance matrix  $[Z_g]$ .

Convergence is reached when the voltage distribution from one iteration to the next does not change, or when the function  $f$  fulfills

$$f(\mathbf{V}_*) = \mathbf{V}_* - [Z_g] \cdot \mathbf{I}(\mathbf{V}_*) - \mathbf{V}_{\text{rf}} = 0, \quad (5.6)$$

where  $\mathbf{V}_*$  denotes the physically consistent solution for the voltage distribution. Therefore, the fixed-point iteration can be translated into a nonlinear multidimensional root problem.

In *KlysTOP*, the convergence of  $\mathbf{I}$  is handled by a dedicated algorithm. The induced currents  $\mathbf{I}_k$  are only used to update the voltages, if they are consistent with the present voltage distribution  $\mathbf{V}_k$ . This aspect will be addressed in more detail after the discussion of the voltage convergence which follows next.

### 5.3 Newton-Raphson Method

A common way to solve a multidimensional root problem as given in Equation (5.6) is to use gradient methods such as the Newton-Raphson method [44]. For the given problem the iteration can be written as

$$\mathbf{V}_{k+1} = \mathbf{V}_k - [J_f(\mathbf{V}_k)]^{-1} \cdot f(\mathbf{V}_k), \quad (5.7)$$

where  $[J_f(\mathbf{V}_k)]$  is the Jacobian of the function  $f$  defined in Equation (5.6) for the voltage distribution  $\mathbf{V}_k$ . This method converges locally with quadratic order and only if the initial state  $\mathbf{V}_0$  is sufficiently close to the convergence point  $\mathbf{V}_*$  [44].

The implemented algorithm of the Newton-Raphson method, or Newton's method, in *KlysTOP* at iteration  $k$  is as follows:

- (1) Evaluate  $f$  at  $\mathbf{V}_k$ .
- (2) Calculate the Jacobian  $[J_f(\mathbf{V}_k)]$ .
- (3) Solve the linear system  $[J_f(\mathbf{V}_k)] \cdot \mathbf{s}_k = -f(\mathbf{V}_k)$  for  $\mathbf{s}_k$ .
- (4) Update the voltages according to  $\mathbf{V}_{k+1} = \mathbf{V}_k + \mathbf{s}_k$ .

In step (2) the Jacobian of  $f$  is calculated, i.e., the linear variation of  $f$  with respect to the voltage distribution at  $\mathbf{V}_k$ . Therefore, the function  $f$  has to be evaluated  $N_c$  times, with  $N_c$  the number of cells in the section under consideration. As each of these evaluations involves PIC calculations under a specific circuit field, this estimation is computationally expensive. Additionally, the Jacobian changes after each iteration step, depending on the degree of nonlinearity of the problem at hand.

It is therefore desirable to avoid the calculation of the Jacobian in step (2) in order to reduce the overall simulation time. Furthermore, convergence should be achieved within the least possible amount of iteration steps, because the most time-consuming operation is the PIC simulation needed to estimate the induced currents.

Especially for tubes with a high number of cells in each section it is advantageous to avoid the second step of the Newton iteration. FW-TWTs usually have a large number of cells per section, because their gain per cell is relatively low.

### 5.4 Broyden's (Good) Method

A modification of Newton's method is Broyden's good<sup>1</sup> method (BGM) [44–46]. It updates the Jacobian, or rather an estimate thereof, in the direction of the last

<sup>1</sup>BGM is the name originally given by Broyden. Broyden's bad method (BBM) is not necessarily worse, it just happened to be that way for the problems Broyden analyzed using his update schemes.

## 5 General Interaction Simulation

iteration step (rank-one update). It is the multidimensional equivalent of the secant method. The iteration can be formulated as

$$\mathbf{V}_{k+1} = \mathbf{V}_k - [B_k]^{-1} \cdot f(\mathbf{V}_k), \quad (5.8)$$

where  $[B_k]$  is the Broyden system matrix. Broyden's method is of superlinear convergence and also requires the initial state  $\mathbf{V}_0$  to be sufficiently close to  $\mathbf{V}_*$  [44]. Even for a converged iteration there is no guarantee that  $[B_k]$  converges to the Jacobian at  $\mathbf{V}_*$  [44, p. 186].

Broyden's good update scheme [44] applied to Equation (5.6) reads

$$[B_{k+1}] = [B_k] + \frac{(\mathbf{y}_k - [B_k] \cdot \mathbf{s}_k) \cdot (\mathbf{s}_k)^H}{\|\mathbf{s}_k\|^2}, \quad (5.9)$$

where  $\mathbf{y}_k = f(\mathbf{V}_k) - f(\mathbf{V}_{k-1})$ ,  $\mathbf{s}_k = \mathbf{V}_k - \mathbf{V}_{k-1}$ , and  $(\cdot)^H$  denotes the conjugate transpose. The advantage of Broyden's method is self-evident. It updates the iteration system matrix using the previous step. No additional function evaluation is necessary and thus the simulation time is not increased by the voltage update. However, it must be checked whether the number of iterations needed to reach  $\mathbf{V}_*$  is actually smaller than that of the Newton-Raphson method, which includes the calculation of  $[J_f]$ . It is possible that more iterations are necessary in total using Equation (5.8), because the update relies on an approximation of the Jacobian matrix.

## 5.5 Initialization Procedures

The convergence of iterative procedures such as Broyden's method can be improved by starting at a location  $\mathbf{V}_0$  closer to  $\mathbf{V}_*$ . Furthermore, a good initial guess  $[B_0]$  helps to keep the required number of iteration steps low. The question is, of course, from where this kind of information can be obtained. Three possibilities are presented here and their impact on the convergence will be discussed in the following section.

### 5.5.1 Unity Initialization

Without further knowledge  $\mathbf{V}_0$  and  $[B_0]$  can be initialized in the following way. The voltage distribution  $\mathbf{V}_0$  is given by the voltages due to the RF input power for the first and by zero for all other sections of the TWT. Broyden's matrix  $[B_0]$  can be initialized with the respective identity matrix  $[I_{N_c}]$  which is equivalent to starting with a fixed-point iteration. This initialization scheme can be written as

$$[B_0] = [I_{N_c}] \text{ and} \quad (5.10)$$

$$\mathbf{V}_0 = \mathbf{V}_{\text{rf}}. \quad (5.11)$$

### 5.5.2 Initialization from Small-Signal Model

Computing the interaction using a small-signal model is orders of magnitude faster than the solution of the nonlinear problem. Therefore, it could be efficient to initialize  $\mathbf{V}_0$  in the large-signal computation by using the small-signal results for the gap voltages. Additionally,  $[B_0]$  can be estimated from the small-signal beam admittance matrix  $[Y_b]$  according to

$$[B_0] = [I_{N_c}] - [Z_g] \cdot [Y_b]. \quad (5.12)$$

The small-signal model does not take into account all effects that occur in the large-signal case. Therefore an error is introduced when using this initialization, especially when the input power  $P_{in}$  is large. Nevertheless, for low input powers this error is supposed to be smaller than the error introduced by an initialization using Equations (5.10) and (5.11).

### 5.5.3 Initialization from Large-Signal Computation

Another possibility is to initialize from a previous large-signal computation at another input power. In a similar fashion as for the small-signal initialization, the converged results  $\mathbf{V}_*$  and the last Broyden matrix  $[B_*]$  are used for initialization, i.e.,

$$[B_0] = [B_*] \text{ and} \quad (5.13)$$

$$\mathbf{V}_0 = \left( \frac{P_{in,new}}{P_{in,old}} \right)^{\frac{1}{2}} \cdot \mathbf{V}_*, \quad (5.14)$$

where  $P_{in,new}$  and  $P_{in,old}$  are the present and the previous input power, respectively. This initialization is convenient, since the saturated output power  $P_{out,sat}$  is often of interest and is commonly obtained by a loop over several input powers.

## 5.6 Convergence Analysis

*KlysTOP* was originally developed for Klystrons and CC-TWTs. It is therefore reasonable to validate BGM and the different initialization schemes on a CC-TWT test case. The only fundamental differences to FW-TWTs are the underlying EC to describe the propagation of the circuit fields and the number of unit cells per section typical for the respective topology. As a consequence, interaction simulation of CC-TWTs is not as time consuming, because the interaction space is electrically shorter compared to FW-TWTs. This allows to conduct a more detailed analysis in a reasonably short time.

## 5 General Interaction Simulation

Table 5.1: Simulation parameters.

$V_0$	$I_0$	$r_b$	$r_t$	$B_0$	$N_c$
20.3 kV	3.6 A	1.2 mm	1.68 mm	250 mT	{8, 12, 15}

The convergence problems do not arise from the nonlinearity of the interaction simulation. Even a small-signal computation using an iterative approach may diverge. The nonlinear nature of the large-signal model certainly complicates the problem, since it adds a tremendous amount of simulation time and complexity. It is therefore convenient to start the analysis by studying the convergence behavior of BGM on the small-signal model. This is done in the next section and thereafter the large-signal convergence is studied.

In both cases a typical CC-TWT is considered. The simulation parameters are reported in Table 5.1. The TWT consists of three sections with 8, 12, and 15 cavities, respectively. An electron beam of  $I_0 = 3.6$  A accelerated by  $V_0 = 20.3$  kV is used for the computations. The electron beam and the tunnel have radii of  $r_b = 1.2$  mm and  $r_t = 1.68$  mm, respectively. A constant magnetic focusing field of  $B_0 = 250$  mT is assumed. The cold delay line exhibits a passband from  $0.83f_0$  to  $f_0$  where  $f_0$  is the upper cutoff frequency. The EC for the CC delay line is briefly described in [36]. Its parameters and their identification are not further specified here for conciseness. The convergence of the iterative approach employing BGM is of interest in this chapter. The actual EC and electron beam parameters are interchangeable for this analysis.

A criterion is necessary to assess the convergence of the iterative approach. The latter can be assumed, if either  $f(\mathbf{V}_k) = 0$  or the step width  $\mathbf{s}_k = -[B_k]^{-1} \cdot f(\mathbf{V}_k)$  becomes very small. The residual  $\epsilon$  is defined as the minimum of

$$\epsilon_f = \frac{\|f(\mathbf{V}_k)\|_2^2}{\|\mathbf{V}_k\|_2^2}, \quad (5.15)$$

and

$$\epsilon_s = \frac{\|\mathbf{s}_k\|_2^2}{\|\mathbf{V}_k\|_2^2}, \quad (5.16)$$

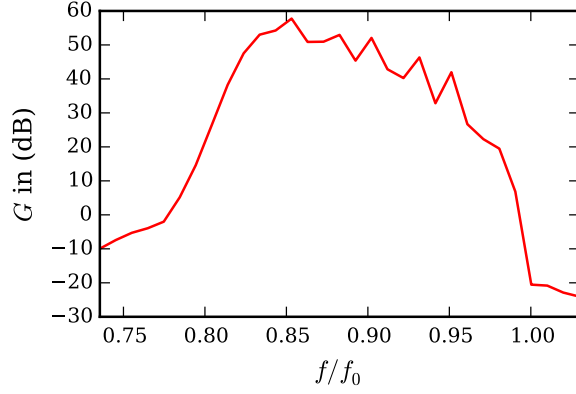
where the norm  $\|\cdot\|_2$  of a vector  $\mathbf{x}$  with length  $N$  is defined by

$$\|\mathbf{x}\|_2^2 = \sum_{n=1}^N |x_n|^2, \quad (5.17)$$

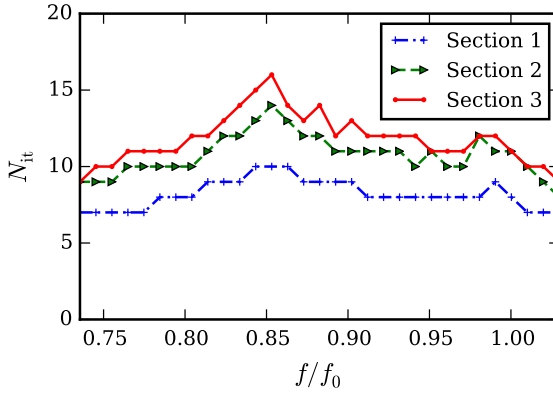
Here, the convergence criterion is defined as

$$\epsilon = \min(\epsilon_f, \epsilon_s) < 10^{-5}. \quad (5.18)$$

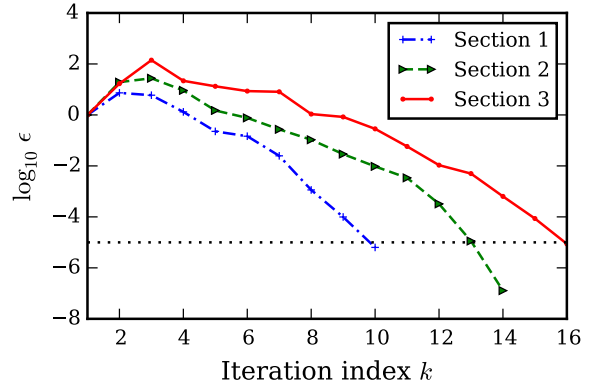
## 5 General Interaction Simulation



(a) Small-signal gain over frequency.



(b) Number of iterations over frequency.



(c) Worst-case convergence profile.

Figure 5.1: Iteration results of the small-signal interaction model.

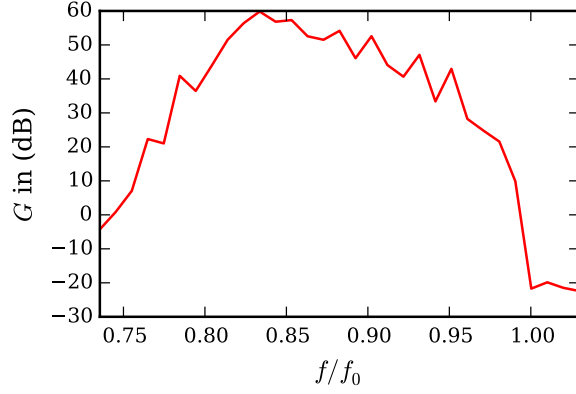
### 5.6.1 Small-Signal Convergence

In the small-signal version of *KlysTOP* the beam admittance matrix  $[Y_b]$  is calculated by successively setting 1 V in each gap and calculating the resulting induced currents. Therefore, it takes  $N_c$  calculations (see Table 5.1) to determine the linear system that describes the interaction inside the considered section. This system of linear equations is then solved, since the problem is linear due to the underlying small-signal approximations. However, Equation (5.8) is applied here in order to test the algorithm.

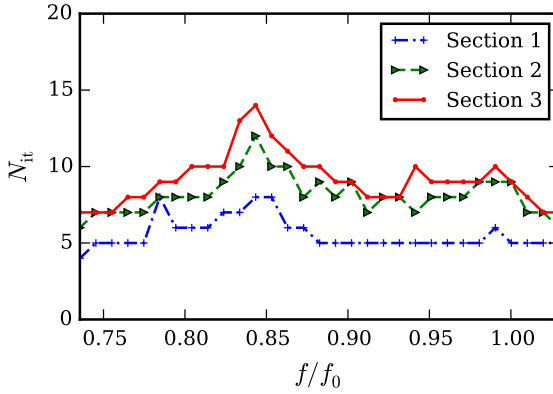
Figure 5.1 reports the results of the iteration. Figure 5.1(a) shows the calculated small-signal gain over frequency. The tube exhibits a maximum gain of about 55 dB which is a typical value for such devices. The gain ripple implies a non-ideal matching at couplers and severs [47]. Calculations performed by directly solving the system of linear equations lead to exactly the same results.

Figure 5.1(b) depicts the number of iterations needed for convergence for each of the three sections over operating frequency. As can be seen, for most frequencies the

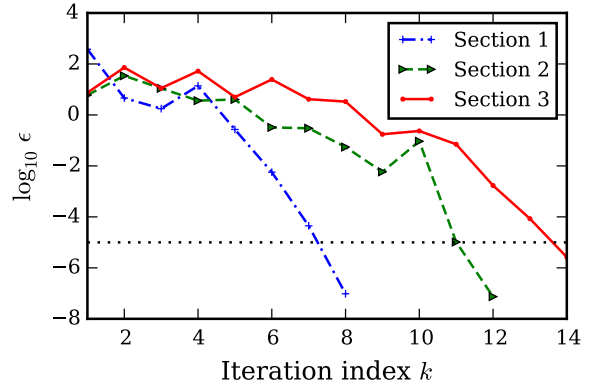
## 5 General Interaction Simulation



(a) Gain over frequency.



(b) Number of iterations over frequency.



(c) Worst-case convergence profile.

Figure 5.2: Iteration results of the large-signal interaction model with  $P_{\text{in}} = -20$  dBm using unity initialization.

iterative approach needs less iterations than the number of cells  $N_c$ , except for strong interaction, e.g., at  $f/f_0 = 0.85$ . At these frequencies the overall amplification is large. This suggests that the number of iterations is linked to the gain of the device or to the degree of synchronism. Additionally, the iteration peaks correlate to some degree to the gain ripple in Figure 5.1(a). This observation further suggests a relationship between the gain inside a section and the number of iterations required for convergence.

Plotting the worst-case convergence profile at  $f/f_0 = 0.853$  results in Figure 5.1(c). The Broyden matrix is initialized with the identity matrix of rank  $N_c$ . Therefore, Broyden's method needs a few training steps where the residual increases or stays approximately constant. During these steps the Broyden matrix is updated with information about the problem. The number of necessary training steps depends on  $N_c$ . Once the Broyden matrix  $[B_k]$  is sufficiently close to the Jacobian, the algorithm starts to converge at nearly the same rate for all sections.

This observation may have strong implications for the large-signal model. An increase of the residual implies that steps are taken in the wrong direction. If this continues for too long, the particles in the PIC simulation may become influenced by unrealistic fields, leading at worst to a diverging computation. In the small-signal model this is not a problem. No matter how large the voltage amplitudes are numerically, the underlying small-signal assumptions always lead to the same results, independently of the voltage path taken during convergence.

## 5.6.2 Large-Signal Convergence

The convergence of the large-signal model largely depends on the applied initialization scheme. For this reason, the impact of the three schemes mentioned above is analyzed in the following sections.

### Convergence Using Unity Initialization

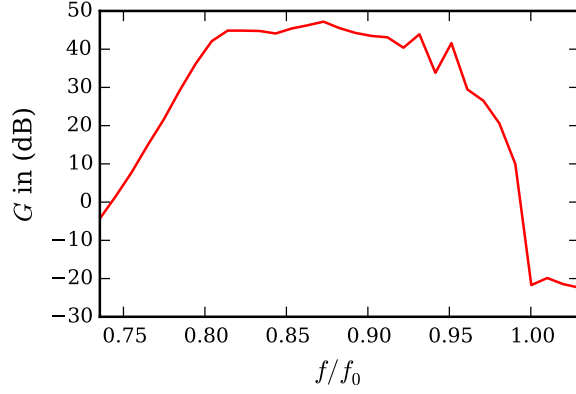
The results of the large-signal computation for an input power of  $P_{\text{in}} = -20$  dBm are shown in Figure 5.2. This input power is considered to drive the tube under linear conditions. However, the gain in Figure 5.2(a) differs from the results of the small-signal model. As the latter does not include radial variation of the electron beam, this is not surprising.

Figure 5.2(b) leads to same conclusions as for the small-signal model. The number of iterations is linked to the device gain and convergence is obtained at all frequencies. The number of iterations is smaller than  $N_c$  at most frequencies, with a pronounced maximum around  $f = 0.85f_0$ . There the convergence is slower in all three sections which is linked to the large amplification. The location of the maximum number of iterations is shifted slightly to lower frequencies compared to the small-signal analysis.

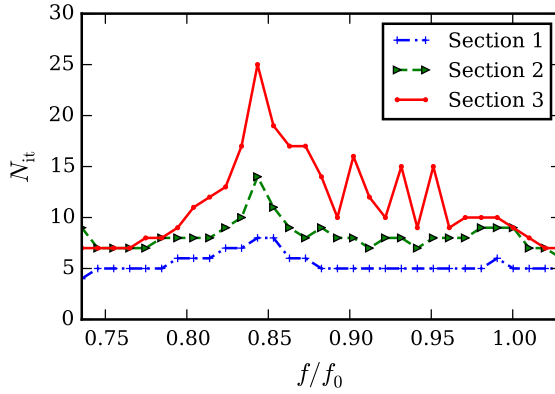
Looking more closely at the worst-case convergence profile at  $f/f_0 = 0.843$  reveals the same principle convergence behavior compared to the small-signal computation. First, the algorithm is trained by the iteration steps followed by a fast decrease of the residual. The necessary number of training steps depends on the number of cells  $N_c$  in each section. Afterwards, the convergence rate is approximately the same for all sections. Since the tube is driven under linear conditions, the Jacobian does not change after each step. Once it is sufficiently well approximated, the iteration converges quite fast. For this reason, the iteration process is also investigated for a larger input power of  $P_{\text{in}} = 25$  dBm.

Considering the results obtained for the larger input power in Figure 5.3(a), it can be seen that the tube is indeed driven into the nonlinear regime. The gain compresses by approximately 10 dB. Additionally, the gain profile is not as strongly tilted in frequency compared to Figure 5.2(a). As the electron beam transfers some

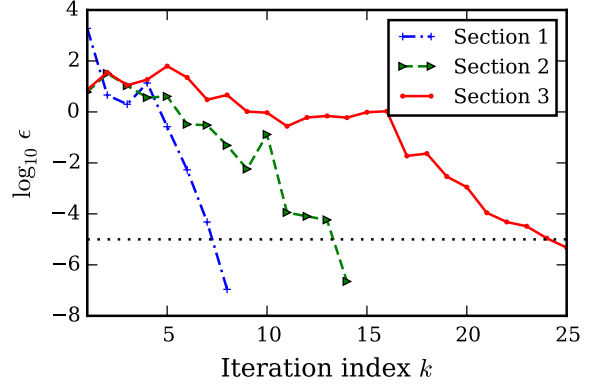
## 5 General Interaction Simulation



(a) Gain over frequency.



(b) Number of iterations over frequency.



(c) Worst-case convergence profile.

Figure 5.3: Iteration results of the large-signal interaction model with  $P_{\text{in}} = 25$  dBm using unity initialization.

of its energy to the circuit wave, it becomes synchronous at other frequencies, thus smoothing some of the dispersive effects.

Figure 5.3(b) reveals some interesting facts about the interaction simulation. The number of iterations in the first section is approximately the same as for the lower input power. The interaction in this section is essentially linear and thus convergence depends only on the number of cells. In the second section the difference is small as well. For the third one the algorithm converges very slowly with pronounced peaks of up to 25 iterations. The frequency region of slow convergence is also shifted to lower frequencies. The electrons in the third section become slower and are therefore synchronous at other frequencies, thus shifting the region of maximum gain.

Considering the convergence profile at the frequency of slowest convergence ( $f/f_0 = 0.843$ ) the previous conclusions are confirmed. While the convergence profile looks very similar in the first two sections for both input powers, the

convergence for the third section is significantly slower for the higher input power. This behavior is caused by the nonlinear part, i.e., the PIC computation. At each new voltage distribution  $\mathbf{V}_{k+1} = \mathbf{V}_k + \mathbf{s}_k$  the Jacobian changes. The update of the Broyden system matrix  $[B_k]$ , however, only takes into account the change along the direction of the step  $\mathbf{s}_k$ . The derivative in the directions orthogonal to the step are unchanged (rank-one update) [46]. The more nonlinear the computation becomes, the stronger the actual Jacobian differs at each new voltage distribution. Figuratively, this behavior corresponds to a hiker seeking a valley who has no sense of direction and needs to sample the vicinity of the valley in order to actually find it.

Additionally, the results summarized in Figure 5.3 confirm that mismatches at the end of the delay line influence the convergence of the algorithm. Some of the iteration peaks in Figure 5.3(b) are correlated with peaks in the gain spectrum in Figure 5.3(a). A similar conclusion was drawn from the small-signal analysis. If the tube were perfectly matched, the electron beam together with the EM fields could be integrated from the beginning to the end of each section without introducing an error. In *KlysTOP* the electron beam is integrated by the PIC algorithm in such a way, i.e., from front to back. The EC, however, feeds energy back from the end of the section to the beginning and thus influences the electron beam in the whole section. It is easy to realize that this feedback further complicates the convergence of the interaction iteration.

### Convergence with Initialization Schemes

A sweep over several values of input power  $P_{\text{in}}$  is in general necessary to obtain the saturated output power  $P_{\text{out,sat}}$ . Therefore, several large-signal computations at the same operating frequency are required. For this kind of computation the large-signal initialization proposed by Equations (5.13) and (5.14) is well suited. The Jacobian and the gap voltages are stored after convergence and used to initialize the next computation with a higher input power. To search the saturation point, typically a low input power is used at first. This input power is considered to drive the tube under linear operating conditions. The small-signal initialization of Equation (5.12) is useful for this purpose.

In the previous section the iteration process was started without an estimate of either the gap voltages or the Broyden matrix. Therefore, convergence was not particularly fast. For the tube considered here, a small-signal simulation takes approximately 0.45 s on a personal computer<sup>2</sup>. This is shorter than one space-charge iteration in the large-signal code which makes the small-signal initialization a very useful tool.

---

<sup>2</sup>Intel Core i7 3770 @ 3.4 GHz and 8 GB of RAM

## 5 General Interaction Simulation

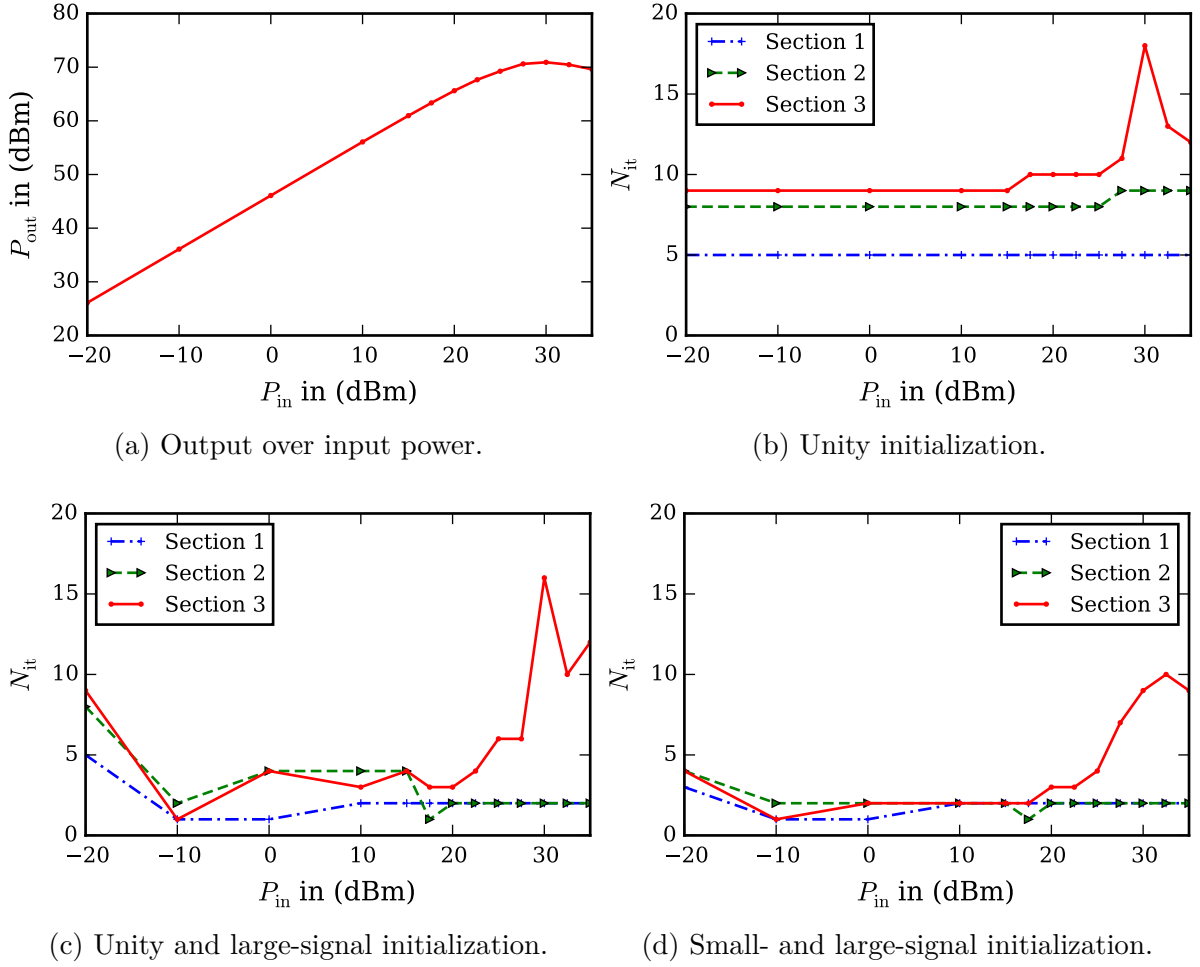


Figure 5.4: Iteration results over input power at  $f/f_0 = 0.89$  for the different initialization schemes.

The  $P_{out}$ - $P_{in}$  characteristic, or drive curve, of the considered CC-TWT at an arbitrarily chosen frequency of  $f/f_0 = 0.89$  is calculated to analyze the impact of the different initializations. The resulting drive curve is depicted in Figure 5.4(a). Thirteen input power levels are used to obtain this curve. The output power saturates around  $P_{in} = 30$  dBm, revealing the nonlinear nature of the amplifier. It reaches a maximum value of  $P_{out,sat} \approx 71$  dBm.

Figures 5.4(b) to 5.4(d) depict the necessary number of iterations over input power for the different initialization schemes. All the schemes result in the same drive curve as the one depicted in Figure 5.4(a). The unity initialization yields the convergence behavior depicted in Figure 5.4(b). For low input powers the number of iterations is constant for all sections as observed earlier. An increase of input power leads to a more nonlinear interaction which starts to manifest in the last section. Closer to saturation the interaction in the second section also becomes

## 5 General Interaction Simulation

Table 5.2: Total number of voltage iterations.

Scheme	Section			$\Sigma$
	1 <sup>st</sup>	2 <sup>nd</sup>	3 <sup>rd</sup>	
Unity	65	108	139	312
Unity/LS	27	38	82	147
SS/LS	25	27	58	110

stronger and one more voltage iteration is necessary. In the last section the number of iterations rises considerably at the saturated output power, but falls again for even larger input powers.

Figure 5.4(c) shows the impact of using a large-signal initialization. Results for the lowest input power are obtained by unity initialization. The iterations at the other operating points are initialized using the respective previous results for  $[B_*]$  and  $\mathbf{V}_*$  according to Equations (5.13) and (5.14). This combined scheme is denoted as “Unity/LS” in the following. This approach drastically reduces the number of necessary voltage iterations. Near saturation, the required number of iterations increases similarly to Figure 5.4(b). The benefit of this initialization is diminished, because the problem becomes more and more nonlinear. A cure could be to decrease the input power step width, thereby improving the estimate. However, the saturated input power is unknown a priori. Therefore, it is not possible to know an appropriate step width beforehand. Additionally, the step width also influences the number of simulations necessary to obtain the saturation point. This means that a trade-off is necessary between the input power discretization and the rate of convergence for each individual simulation run.

Figure 5.4(d) illustrates the impact of initializing from small-signal results for the lowest input power and from large-signal results for all subsequent operating conditions. This scheme is identified by “SS/LS” in the following. The outcome of using this scheme is very similar to the previous case, but the convergence is a lot faster for the lowest input power. Also, the transition to the nonlinear regime is smoother. This can be explained in the following way. For the “Unity/LS” scheme, the Broyden matrix is initialized at the lowest input power using the identity matrix and the number of steps required to obtain convergence might not be sufficient to have a good estimate of the Jacobian. Nevertheless, the Broyden matrix is accurate enough to achieve convergence. However, if this rough estimate is then used for the next operating point, the introduced error has to be compensated by additional Newton steps. On the other hand, a complete estimate of the derivative is obtained using the small-signal initialization for the lowest input power. It is therefore not as critical in this case, if only a few Newton steps are needed for convergence.

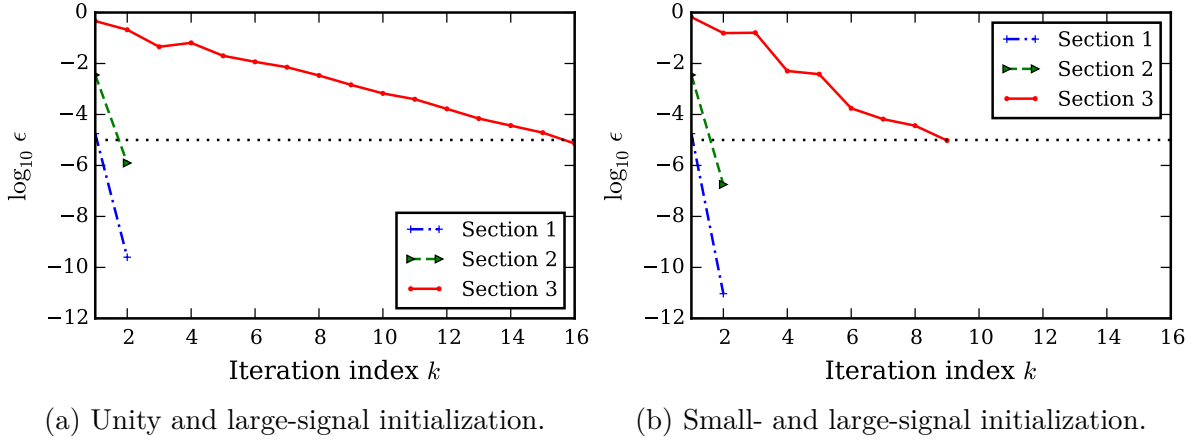


Figure 5.5: Convergence profiles at  $f/f_0 = 0.89$  and  $P_{\text{in}} = 30$  dBm resulting from different initialization schemes.

To support the above observation, the convergence profiles resulting from the “Unity/LS” and “SS/LS” scheme at  $f/f_0 = 0.89$  and  $P_{\text{in}} = 30$  dBm are depicted in Figures 5.5(a) and 5.5(b), respectively. A substantial difference can be observed between the profiles obtained by the respective initialization schemes. While convergence is reached in the first two sections after only two iterations for both schemes, the small-signal initialization is beneficial for the convergence in the last section, even though the operating point is far away from the initial computation.

The total number of voltage iterations for the different initialization schemes required to obtain the 13 data points of the amplifier characteristic in Figure 5.4(a) is summarized in Table 5.2. The benefit of using the large-signal initialization is evident. This initialization scheme comes at practically no additional computational cost and is thus very efficient. A factor of two can be saved in terms of iteration steps which is directly proportional to the overall simulation time. The merit of the small-signal initialization is obvious as well. A lot of time can be saved by prepending a small-signal calculation which is two to three orders of magnitude faster than the large-signal code.

## 5.7 Space-Charge Iterations

The presented convergence analysis considers only the update of the gap voltages. The convergence has not been analyzed when using more particles for the PIC simulation of the beam, or when refining the finite element mesh or the number of time steps per RF period. All these parameters affect the computing time in several ways. This study has intentionally been omitted here, since it is outside the scope of this thesis. However, some studies have been conducted and it was observed that

## 5 General Interaction Simulation

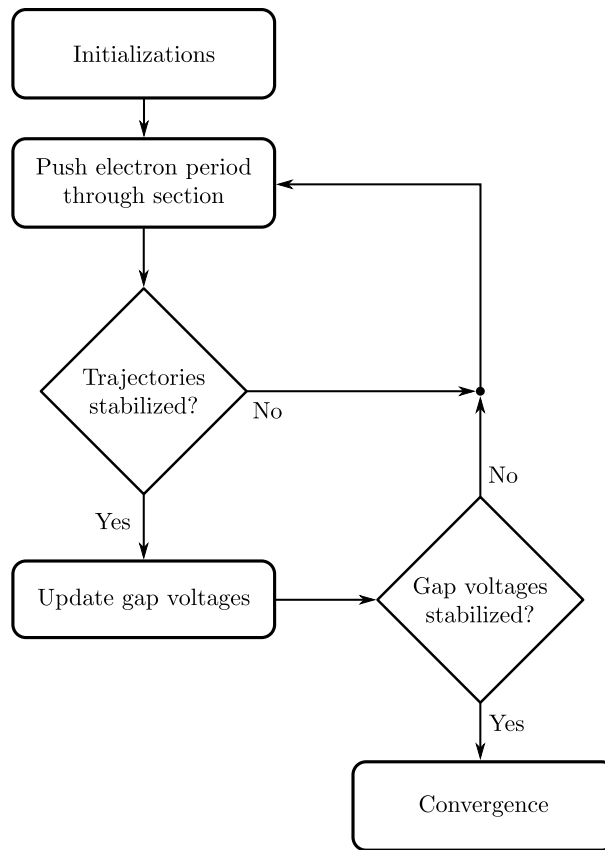


Figure 5.6: Flow chart of *KlysTOP* algorithm.

the simulation and discretization parameters must be chosen carefully to guarantee reliable results. The results obtained in the previous sections are not affected, if the simulation parameters are further refined.

However, one additional consideration is addressed in this section, because it has critical influence on the convergence for structures which are electrically longer than CC-TWTs, such as FW-TWTs. As has been already indicated, the current program sequence in *KlysTOP* involves a two-fold loop. The outer one is the update of the gap voltages addressed in the presented convergence analysis. Inside this loop, a PIC simulation runs several times until the electron trajectories, or space-charge fields, have converged. The convergence is checked by monitoring the induced currents at each gap. The algorithm of *KlysTOP* for each section of a TWT is summarized in Figure 5.6 as a flow chart.

There is a peculiarity about the algorithm implemented into *KlysTOP*. Most PIC solvers emit electrons into the computational domain until the space-charge fields have stabilized. This can take a long time, since the computational time increases with the number of particles. The PIC solver in *KlysTOP* exploits the fact that a steady-state solution under harmonic excitation is sought. Electrons are

## 5 *General Interaction Simulation*

thus only emitted through one RF period into the interaction area. This electron package travels to the end of the section while it is exposed to the EM fields. The electric field along the circuit is fixed during this space-charge loop, because the gap voltages are assumed to be constant. After the first space-charge iteration the electrons are additionally influenced by the space-charge fields arising from the trajectories of the previous iteration. This process is repeated until the trajectories do not change from one iteration to the next. Then the gap voltages and the circuit fields are updated. These two nested loops are repeated until total convergence is achieved.

The gap voltage loop and the space-charge loop are independent from each other in a sense that both can be dealt with in an individual way. The voltage update can be implemented using Broyden's method without changing the update of the space-charge fields in any way. This is why the space-charge convergence could be excluded from consideration for the convergence analysis of the gap voltages.

At some operating conditions overall convergence may not be reached due to the space-charge iterations. This is a numerical issue that has not been solved by the time this thesis was written. Possible reasons might be the discretization of space, time, and charge density which cause instabilities under certain conditions.

## 6 Folded-Waveguide Interaction Simulation

There are, amongst others, proprietary software packages to compute the beam-wave interaction in CC-TWTs developed by research laboratories in the United States of America. CHRISTINE-CC, for example, implements a one-dimensional, large-signal steady-state method [48]. TESLA-CC, on the other hand, is a two-dimensional, large-signal envelope code, featuring a hybrid approach between time and frequency domain [49]. Both describe the EM wave on the delay line by means of ECs, and have been extended to FW-TWTs by implementing appropriate circuit models for FW delay lines [50]. However, these beam-wave interaction tools are in general not available.

Therefore, the improvements regarding the iterative interaction simulation from Chapter 5 are applied to FW-TWTs to have competitive simulation tools. FW-TWTs generally have a much higher number of cells per section. The original *KlysTOP* iteration scheme implements the Newton-Raphson method and thus estimates the Jacobian at the beginning of the actual interaction computation. This approach becomes exceedingly inefficient for FW-TWTs, because a lot of time is spent to calculate something the user is not directly interested in. The approach described in Section 5.4 is much more convenient in this case, because an approximation of the Jacobian is calculated as the algorithm progresses without any additional computational effort. Moreover, according to the findings in Section 5.6, this approach works very well when the gain per cell is relatively low as is the case for TWTs with FW delay lines.

The FW delay line is approximated using Antonsen’s EC model presented in Section 3.3. Input and output couplers are modeled as ideal transformers exhibiting zero reflection for cold operation. An optimized delay line is required to study the large-signal performance of FW-TWTs with *KlysTOP*. This means that the delay line has to be tapered to extract a large amount of energy from the electron

Table 6.1: Geometry parameters of the delay line.

$a_{\text{wg}}$	$b_g$	$b_s$	$L_s$	$r_t$	$L_{\text{tube}}$
3.8 mm	0.55 mm	0.9 mm	2.0 mm	0.35 mm	132 mm

## 6 Folded-Waveguide Interaction Simulation

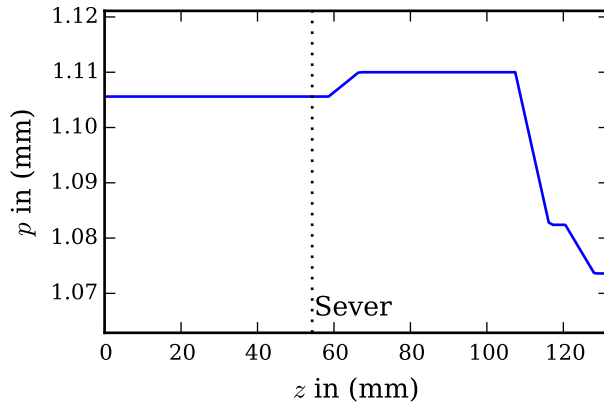


Figure 6.1: Pitch taper of the considered folded-waveguide traveling-wave tube.

beam. Tapering in this sense means a change of delay line characteristics in axial direction  $z$ . Most commonly, the pitch  $p$  is changed in order to keep the EM wave synchronous with the electron bunches as they lose kinetic energy. For the subsequent analysis the optimized taper presented in [51] is used. It has been obtained by an automatized optimization procedure [52]. The pitch taper  $p(z)$  is depicted in Figure 6.1. The geometry and electronic parameters are given in Tables 6.1 and 6.2, respectively.

### 6.1 Interaction Convergence

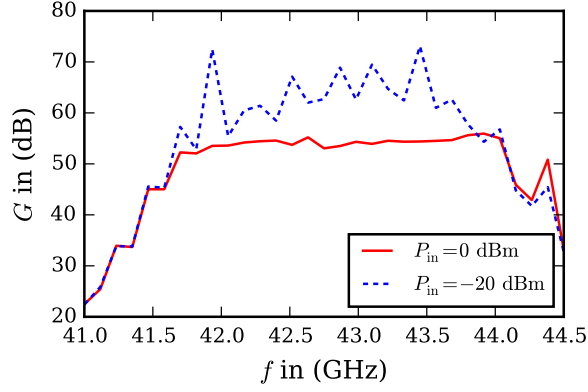
The convergence analysis in this section is not as detailed as in Section 5.6. The benefit of using Broyden's method for interaction simulation of FW-TWTs is briefly elaborated. The iteration is initialized with the unity scheme (Section 5.5.1). Of course, for loops over input power the schemes presented earlier yield the same benefits for FW-TWTs.

Figure 6.2 summarizes the convergence for an input power of  $P_{\text{in}} = 0$  dBm. The tube has two sections with 51 and 69 cells, respectively. Figure 6.2(a) reports the gain. The tube is driven into the nonlinear regime, since the gain is nearly constant between 42 and 43.5 GHz and does not follow the gain for an input power of  $P_{\text{in}} = -20$  dBm which is also indicated in Figure 6.2(a). A ripple of the gain due to the assumed cold match is observed in this frequency range. The ripple

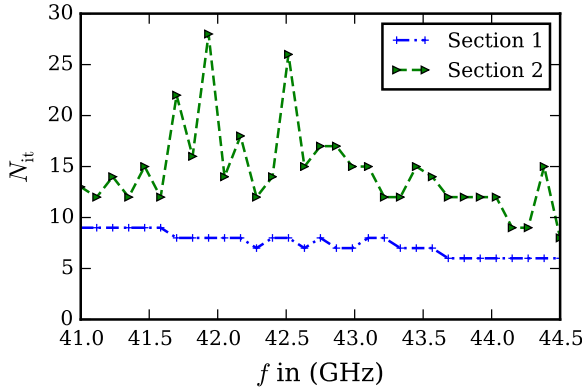
Table 6.2: Electronic parameters used for interaction simulation.

$V_0$	$I_0$	$r_{\text{beam}}$	$B_0$
14 kV	200 mA	0.22 mm	2200 G

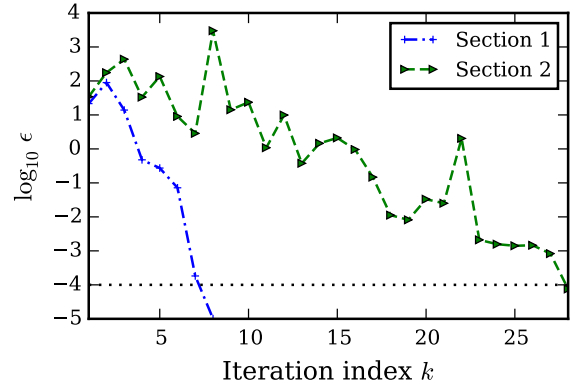
## 6 Folded-Waveguide Interaction Simulation



(a) Gain over frequency.



(b) Number of iterations over frequency.



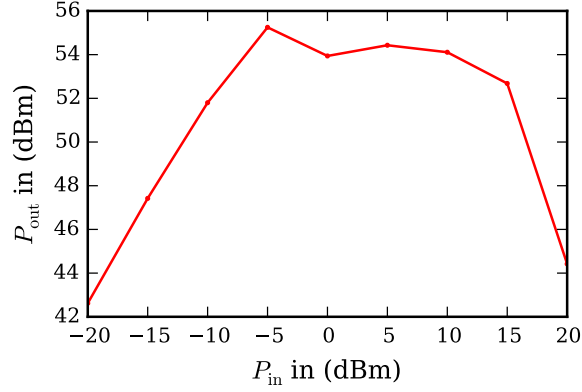
(c) Worst-case convergence profile.

Figure 6.2: Iteration results for the large-signal interaction model with  $P_{\text{in}} = 0$  dBm using unity initialization.

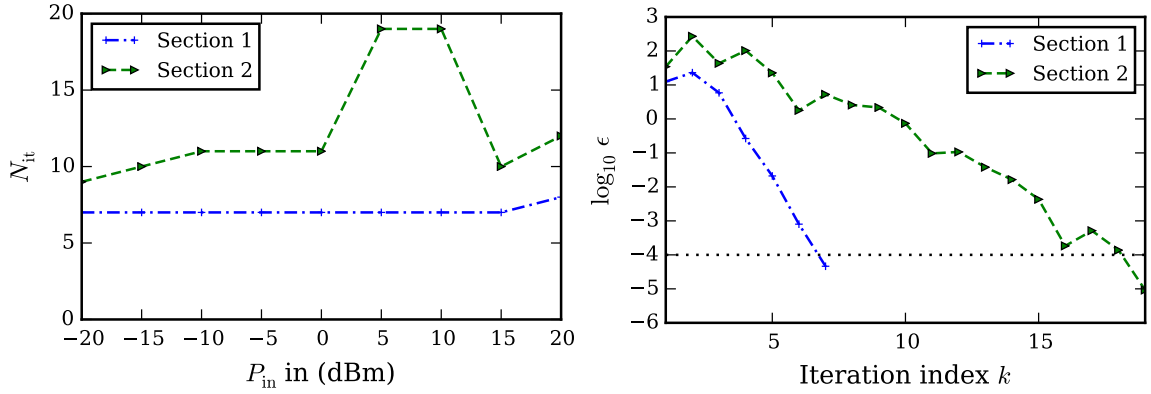
is smoothed out for the larger input power by nonlinear effects. For frequencies below 41.5 GHz and above 44 GHz the gain is approximately the same for both input powers.

The iterations necessary for convergence for  $P_{\text{in}} = 0$  dBm are displayed in Figure 6.2(b) as a function of operating frequency  $f$ . In the first section the interaction is essentially linear and convergence is reached after six to eight iterations over the entire frequency band. The number of necessary iterations is much lower than the number of unit cells in this section. In contrast, the original *KlysTOP* iteration algorithm needs eight times as many iterations just to initialize the Jacobian. The improvement achieved by implementing Broyden's method is obvious in this case. In the second section more iterations are needed for convergence. However, the number of unit cells is much larger and thus the new implementation is also efficient in this case. Looking more closely at the iteration count, strong peaks occur throughout the frequency band, with a maximum of 28 at  $f = 41.93$  GHz.

## 6 Folded-Waveguide Interaction Simulation



(a) Output over input power.



(b) Number of iterations over input power. (c) Convergence profile at  $P_{\text{in}} = 5$  dBm.

Figure 6.3: Convergence behavior at  $f = 43$  GHz for different input power levels.

The corresponding convergence profile is plotted in Figure 6.2(c). While the residual in the first section decreases almost monotonically, in the second section it increases sporadically during the convergence process. This extends the overall simulation time significantly, because each voltage iteration entails on average 20 space-charge iterations (cf. Section 5.7). The local growth of  $\epsilon$  is reminiscent of the training steps already observed in Section 5.6. During convergence, the Jacobian is estimated at several steps. However, if the interaction is strongly nonlinear, the Jacobian is a function of the voltage distribution and thus also changes during the convergence process.

Figure 6.3 further summarizes the convergence behavior for several levels of input power at an operating frequency of 43 GHz in the center of the amplification bandwidth. Figure 6.3(a) shows the output power characteristic with an unusual property above saturation. The output power is largest for  $P_{\text{in}} = -5$  dBm, drops slightly, and then stays approximately constant up to 10 dBm. Figure 6.3(b) reports the required number of iterations for each section. Again, convergence is obtained

in a number of steps much smaller than the number of cells inside the respective section. As expected, more iterations are necessary in overdrive compared to the saturation point due to the strong nonlinearity of the problem. Figure 6.3(c) shows the convergence profile for an input power of  $P_{\text{in}} = 5$  dBm. Convergence in the first section is obtained with almost monotonically decreasing residual, while in the second section it is again slower with some increases in error during the iteration. Therefore, the unusual behavior observed in Figure 6.3(a) has no significant implications for the iteration convergence in this case.

## 6.2 Comparison of Interaction Results

The software package *MVTRAD* (from French: *mouvement radial*) is a 2.5D steady-state beam-wave interaction tool from *Thales Electron Devices* [53, 54]. It predicts the interaction by applying the Poynting theorem to the beam-wave system from the front of the tube to the back. Reflections due to mismatches are neglected in *MVTRAD*, but can be considered by a recent extension of the program [54]. However, this extension increases the computing time considerably. *MVTRAD* assumes cylindrical symmetry of the beam tunnel region and uses the coupling impedance to build the axial electric field. All other electric and magnetic field components are extrapolated from the axis by well-known analytical relations. Interaction prediction close to band edges is not possible using this code, because the gain then grows indefinitely. This is due to very large values of the coupling impedance combined with the fact that the backward propagating wave is not taken into account. This shortcoming of *MVTRAD* was one of the main reasons for *Thales* to develop *KlysTOP*.

Nevertheless, *MVTRAD* can be used as a reference tool for frequencies far away from the cold cutoff frequency of the delay line. It is used here without the extension to include reflections. Results for an input power of  $P_{\text{in}} = 0$  dBm from *KlysTOP* and *MVTRAD* for the FW-TWT in Section 6.1 are displayed in Figure 6.4. The agreement in terms of bandwidth is good. The gain predicted by *MVTRAD* is smooth, because reflections are neglected and thus effects due to multiple reflections such as a gain ripple can not occur [54]. In *KlysTOP* these effects are taken into account by the EC and feedback from the back to the front of a section is included by the iterative approach. Results from *CST Particle Studio* at the same input power are also indicated in Figure 6.4 for additional reference. They have been shifted to higher frequencies by 250 MHz for better comparison with the other results. This frequency shift can be explained by a different beam rotation in *CST*. This leads to a different axial velocity of the electrons which, in turn, alters the condition for synchronism. Apart from this frequency shift, the agreement is better than 1 dB. Deviations up to 2 dB arise only at the upper amplification band. These

## 6 Folded-Waveguide Interaction Simulation

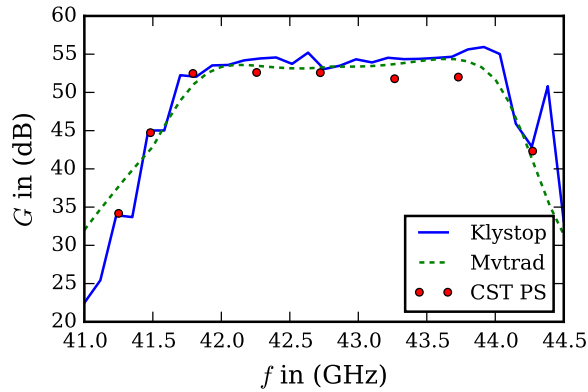


Figure 6.4: Simulation results for  $P_{\text{in}} = 0$  dBm using *Klystop*, *MVTRAD*, and *CST Particle Studio*.

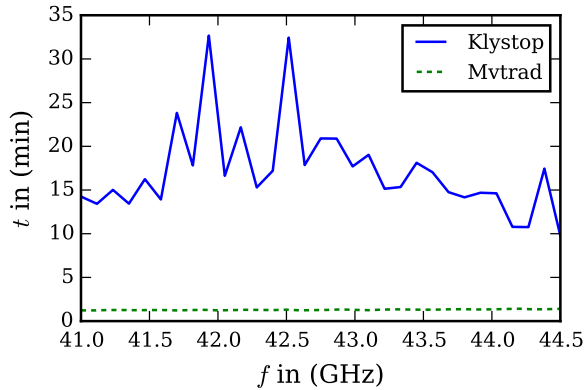


Figure 6.5: Simulation time of *Klystop* and *MVTRAD* over frequency.

deviations from *CST* results can be explained by the fact that the transients have not totally decayed in the time-domain calculation. This deteriorates the evaluated power levels.

The simulation time required by *Klystop* and *MVTRAD* to obtain the above results is plotted over frequency in Figure 6.5. For *Klystop* it is directly correlated to the number of voltage iterations for the last section in Figure 6.2(b). On average 17 min are necessary. *Klystop* thus clearly outperforms commercial time-domain solvers such as *CST Particle Studio* which require tens of hours computing time per operating point for similarly realistic problems. *MVTRAD*, on the other hand, takes approximately 75s per operating point. The extension for *MVTRAD* including reflections increases the computing time approximately by a factor of ten [54]. *Klystop* and *MVTRAD* are then comparable in terms of speed.

# 7 Conclusion

Traveling-wave tubes are high-power vacuum electronic devices with high-efficiency used as sources for microwave radiation. Their radio frequency response depends largely on the delay line technology. The two dominant structures are the helical and the coupled-cavity delay line. The former features superior bandwidth performance, the latter achieves highest output powers. The folded-waveguide delay line is a relatively novel structure which can be regarded as a trade-off in terms of bandwidth and output power between the two established topologies.

In this thesis various aspects of folded-waveguide traveling-wave tubes are elaborated and analyzed to gain insight into this complex device.

In Chapter 2 the main components of a traveling-wave tube are briefly described, and a general understanding about their functionality is conveyed. Afterwards, the interaction problem is addressed by separating it into two main systems, i.e., the electromagnetic circuit and the electron beam. Synchronous operation is briefly outlined to illustrate the operating mode of a traveling-wave tube. The concept of nonlinearities is also addressed and the necessity of specialized numerical software is stressed.

Chapter 3 outlines possibilities to characterize and model folded-waveguide delay lines. The propagation characteristics can be calculated using an eigenmode analysis by exploiting the periodic nature of the delay line. An extensive parametric investigation is performed using this approach. The results can be used to shape the electromagnetic response of a folded-waveguide delay line. Nose cones are found to be a feasible means to improve the beam-wave coupling of this kind of delay line. Once the structure is fixed, it is modeled by an equivalent circuit for later implementation into a specialized beam-wave interaction tool called *KlysTOP*. This circuit has to provide the correct dispersion and impedance in order to model the delay line properly. An accurate model from literature is used and a fitting algorithm is briefly described that determines the elements of the lumped circuit. Models for the input and output couplers as well as for the attenuating sever elements are additionally provided. With these constituents a complete traveling-wave tube delay line can be modeled. The chapter continues by assessing the importance of a proper model for the shape of the axial electric field in order to simulate the beam-wave interaction in folded-waveguide traveling-wave tubes. A synthesis approach for a local field shape independent of frequency is given. Fabrication of folded-waveguide lines and their cold characterization are additionally addressed. Delay lines for

## 7 Conclusion

Q-band applications featuring nose cones to shape the electromagnetic response are fabricated and the results are evaluated using optical and microwave measurement. The measured propagation constant agrees very well with full-wave estimates. The results show micro-machining to be sufficiently accurate for this frequency range.

In Chapter 4 the hot propagation along the delay line is analyzed. When the delay line is coupled to an electron beam, interaction takes place and modifies the propagation characteristics along the structure. The coupled system can be modeled by an effective transmission line using a small-signal approach. The change of propagation constant and characteristic impedance is derived, and the impact of beam-wave coupling on the matching conditions of traveling-wave tubes is analyzed. The stability of the active device can be improved by taking the electron beam into account during the design process of the delay line. The small-signal characteristic impedance is then applied to a large-signal computation in *KlysTOP*. The performance for small input powers is confirmed, but it is shown to deteriorate for larger ones, because the small-signal assumptions are violated. The operating point of the tube is virtually shifted by the strong modulation of the electron beam. Additionally, harmonics of the fundamental operating frequency arise that are not taken into account by the small-signal model. At the end of the chapter a physical sever structure is briefly described that presents the proper load to a traveling-wave tube input section for stable operation and an optimization process is sketched.

Chapter 5 describes an approach to predict large-signal beam-wave interaction for a traveling-wave tube with sinusoidal excitation. As the nonlinear problem is split into its linear (the delay line) and nonlinear part (the electron beam), a consistent solution is obtained by means of an iterative process. The focus in this thesis is on the convergence with regard to the electromagnetic fields on the delay line. A quasi-Newton algorithm is implemented as a means to accelerate the interaction simulation. This algorithm is tested on a tube with a coupled-cavity delay line to verify the approach, analyze the convergence, and assess the performance of the proposed method. For this kind of traveling-wave tube, an acceleration factor between two and three is achieved. Additionally, alternatives to initialize the iterative process are described and evaluated. A considerable amount of time is saved by exploiting the underlying physics behind the beam-wave interaction problem. Depending on the tube's linearity and the change in operating condition, an additional factor of two to three can be saved in terms of simulation time.

Chapter 6 at last combines the previously introduced concepts and discusses the large-signal performance of a folded-waveguide traveling-wave tube with an optimized delay line. As these devices have sections that are electrically very long, the implemented iteration algorithm has a tremendous impact on simulation speed. The interaction results are validated with those obtained by an established specialized software called *MVTRAD* and a commercial particle-in-cell solver from *CST*. The agreement between results is good. However, the computing times differ

## 7 Conclusion

by orders of magnitude. While *MVTRAD* needs approximately one minute per frequency and operating point, *KlysTOP* takes about twenty minutes. The *CST* solver needs approximately one day of computation, but is also the most general tool.

All parts necessary to efficiently predict the beam-wave interaction of folded-waveguide traveling-wave tubes are subsumed in this work. This is an important step to allow engineers to explore new concepts for traveling-wave tubes and design the interaction space according to their desire. Efficient software is an enabling part to push new concepts from the lab to the market in a time frame that would otherwise not be realizable.

As an outlook for this thesis, the following topics should be investigated further. Instead of an abstract equivalent circuit, a physical model for couplers and severs should be developed. The flexibility to analyze the impact of local reflections caused by these components is a good asset in a more fundamental study like in this thesis, but constitutes more of a hindrance when a real delay line has to be designed and optimized. Then, the actual reflection must follow implicitly from the physical design.

Regarding the interaction simulation, several aspects could be investigated further. One-dimensional nonlinear tools could be used to initialize the iteration process and further improve the initial guess for both the Jacobian and the voltage distribution. Furthermore, interaction becomes more and more nonlinear in axial direction which may be exploited for the initialization as well. To accelerate the simulation even more, the space-charge iteration including the particle-in-cell algorithm could be improved. As this is the most time-consuming operation, the potential speed-up margin is supposedly very large.

A folded-waveguide delay line featuring the proposed nose cones should be implemented into a traveling-wave tube to assess its feasibility for space applications. Such a device is expected to be very robust against mechanical and thermal stress and should thus be a very good candidate for high-power applications. The bandwidth and power capabilities also act in favor of this topology. To build such a device, an electron gun needs to be designed, the delay line must be optimized in terms of pitch profile, and a multi-stage collector has to be developed. This overall design is a project in its own right due to the interdependency and complexity of the components. Additionally, the concept of matching for hot operation under large-signal operating conditions should be investigated further to improve the tube performance.

All in all, vacuum technologies are far from extinct and are a challenging research topic. In the 70 years of its development, the traveling-wave tube has succeeded to meet the ever higher requirements of our modern communication society. This trend can be continued by developing new concepts for vacuum devices and refining the prediction capabilities of modern computer codes.

# Bibliography

- [1] R. J. Barker, J. H. Booske, N. C. J. Luhmann, and G. S. Nusinovich, *Modern Microwave and Millimeter-Wave Power Electronics*. IEEE Press, 2005.
- [2] J. A. Eichmeier and M. Thumm, *Vacuum Electronics: Components and Devices*. Springer Berlin Heidelberg, 2008.
- [3] G. Dohler, D. Gagne, D. Gallagher, and R. Moats, “Serpentine Waveguide TWT”, in *Proc. Int. Electron Devices Meeting*, vol. 33, 1987, pp. 485–488. DOI: [10.1109/IEDM.1987.191465](https://doi.org/10.1109/IEDM.1987.191465).
- [4] C. L. Kory, L. Ives, M. Read, J. H. Booske, H. Jiang, D. van der Weide, and P. Phillips, “Microfabricated W-Band Traveling Wave Tubes”, in *Proc. Joint Int. Conf. Infrared and mm Waves and Int. Conf. THz Electronics*, vol. 1, 2005, 85–86 vol. 1. DOI: [10.1109/ICIMW.2005.1572419](https://doi.org/10.1109/ICIMW.2005.1572419).
- [5] J. Cai, J. Feng, and F. Liao, “Investigation of W-Band Folded Waveguide Slow-Wave Structure using MAFIA”, in *Proc. IEEE Int. Vacuum Electronics Conf. held Jointly with IEEE Int. Vacuum Electron Sources*, 2006, pp. 453–454. DOI: [10.1109/IVELEC.2006.1666378](https://doi.org/10.1109/IVELEC.2006.1666378).
- [6] J. Feng, J. Cai, X. Wu, S. Ma, Y. Hu, and M. Huang, “Design Investigation of 10W W-Band Folded Waveguide TWT”, in *Proc. IEEE Int. Vacuum Electronics Conf. (IVEC)*, 2007, pp. 1–2. DOI: [10.1109/IVELEC.2007.4283224](https://doi.org/10.1109/IVELEC.2007.4283224).
- [7] H. Gong, Y. Gong, T. Tang, J. Xu, and W.-X. Wang, “Experimental Investigation of a High-Power Ka-Band Folded Waveguide Traveling-Wave Tube”, *IEEE Trans. Electron Devices*, vol. 58, no. 7, pp. 2159–2163, 2011. DOI: [10.1109/TED.2011.2148119](https://doi.org/10.1109/TED.2011.2148119).
- [8] C. D. Joye, A. M. Cook, J. P. Calame, D. K. Abe, A. N. Vlasov, I. A. Chernyavskiy, K. T. Nguyen, and E. L. Wright, “Microfabrication and Cold Testing of Copper Circuits for a 50-Watt 220-GHz Traveling Wave Tube”, in *Proc. SPIE OPTO*, 2013, pp. 1–9.
- [9] J. Feng, J. Cai, Y. Hu, X. Wu, Y. Du, J. Liu, P. Pan, and H. Li, “Development of W-Band Folded Waveguide Pulsed TWTs”, *IEEE Trans. Electron Devices*, vol. 61, no. 6, pp. 1721–1725, 2014. DOI: [10.1109/TED.2014.2307476](https://doi.org/10.1109/TED.2014.2307476).

## Bibliography

- [10] R. K. Sharma, A. Grede, S. Chaudhary, V. Srivastava, and H. Henke, “Design of Folded Waveguide Slow-Wave Structure for W-Band TWT”, *IEEE Trans. Plasma Sci.*, vol. 42, no. 10, pp. 3430–3436, 2014. DOI: [10.1109/TPS.2014.2352267](https://doi.org/10.1109/TPS.2014.2352267).
- [11] A. S. Gilmour Jr., *Principles of Traveling Wave Tubes*, ser. The Artech House Radar Library. Artech House, Incorporated, 1994.
- [12] J. Hanika, C. Dietrich, and P. Birtel, “Thales 300 Watt Ku-Band Radiation and Conduction Cooled Travelling Wave Tube”, in *Proc. IEEE Int. Vacuum Electronics Conf. (IVEC)*, 2015, pp. 1–2. DOI: [10.1109/IVEC.2015.7223815](https://doi.org/10.1109/IVEC.2015.7223815).
- [13] C. D. Joye, A. M. Cook, J. P. Calame, D. K. Abe, K. T. Nguyen, E. L. Wright, A. N. Vlasov, I. A. Chernyavskiy, T. Kimura, and B. Levush, “Demonstration of a High Power, Wideband 220 GHz Serpentine Waveguide Amplifier Fabricated by UV-LIGA”, in *Proc. IEEE Int. Vacuum Electronics Conf. (IVEC)*, 2013, pp. 1–2. DOI: [10.1109/IVEC.2013.6571005](https://doi.org/10.1109/IVEC.2013.6571005).
- [14] G. Guo, Y. Wei, Y. Gong, Z. Duan, and G.-S. Park, “Analysis of the Three Types of Folded Waveguide Slow-Wave Structure for 140 GHz Traveling Wave Tube”, in *Proc. IEEE Int. Vacuum Electronics Conf. (IVEC)*, 2014, pp. 307–308. DOI: [10.1109/IVEC.2014.6857612](https://doi.org/10.1109/IVEC.2014.6857612).
- [15] J. R. Pierce, *Traveling-Wave Tubes*, ser. Bell Telephone Laboratories. Van Nostrand, 1950.
- [16] R. E. Collin, *Foundations for Microwave Engineering*, ser. IEEE Press on Electromagnetic Wave Theory. Wiley, 2001.
- [17] J. D. Wilson, “Electromagnetic Field Shaping for Efficiency Enhancement in Terahertz Folded-Waveguide Traveling-Wave Tube Slow-Wave Circuit Design”, in *Proc. IEEE Int. Vacuum Electronics Conf. (IVEC)*, 2007, pp. 1–2. DOI: [10.1109/IVELEC.2007.4283222](https://doi.org/10.1109/IVELEC.2007.4283222).
- [18] J. He, Y. Wei, Y. Gong, W. Wang, and G.-S. Park, “Investigation on a W Band Ridge-Loaded Folded Waveguide TWT”, *IEEE Trans. Plasma Sci.*, vol. 39, no. 8, pp. 1660–1664, 2011. DOI: [10.1109/TPS.2011.2157176](https://doi.org/10.1109/TPS.2011.2157176).
- [19] J. Cai, J. Feng, Y. Hu, X. Wu, Y. Du, and J. Liu, “10 GHz Bandwidth 100 Watt W-Band Folded Waveguide Pulsed TWTs”, *IEEE Microw. Comp. Lett.*, vol. 24, no. 9, pp. 620–621, 2014. DOI: [10.1109/LMWC.2014.2328891](https://doi.org/10.1109/LMWC.2014.2328891).
- [20] I. A. Nakrap and A. N. Savin, “Comparison of a Class of Millimeter-Band Slow-Wave Structures with a Traditional Chain of Coupled Resonators”, English, *Journal of Communications Technology and Electronics*, vol. 59, no. 8, pp. 852–859, 2014. DOI: [10.1134/S1064226914080166](https://doi.org/10.1134/S1064226914080166).

## Bibliography

- [21] A. W. Chao, K. H. Mess, M. Tigner, and F. Zimmermann, *Handbook of Accelerator Physics and Engineering*. World Scientific Publishing Company, 2013.
- [22] T. M. Antonsen, A. N. Vlasov, D. P. Chernin, I. A. Chernyavskiy, and B. Levush, “Transmission Line Model for Folded Waveguide Circuits”, *IEEE Trans. Electron Devices*, vol. 60, no. 9, pp. 2906–2911, 2013. DOI: [10.1109/TED.2013.2272659](https://doi.org/10.1109/TED.2013.2272659).
- [23] D. P. Chernin, T. M. Antonsen, A. N. Vlasov, I. A. Chernyavskiy, K. T. Nguyen, and B. Levush, “1-D Large Signal Model of Folded-Waveguide Traveling Wave Tubes”, *IEEE Trans. Electron Devices*, vol. 61, no. 6, pp. 1699–1706, 2014. DOI: [10.1109/TED.2014.2298100](https://doi.org/10.1109/TED.2014.2298100).
- [24] H. J. Curnow, “A General Equivalent Circuit for Coupled-Cavity Slow-Wave Structures”, *IEEE Trans. Microw. Theory and Techn.*, vol. 13, no. 5, pp. 671–675, 1965. DOI: [10.1109/TMTT.1965.1126062](https://doi.org/10.1109/TMTT.1965.1126062).
- [25] N. Marcuvitz, *Waveguide Handbook*, ser. IEE Electromagnetic Waves. P. Peregrinus, 1951.
- [26] R. Collin, *Field Theory of Guided Waves*, ser. IEEE Press on Electromagnetic Wave Theory. New York: IEEE Press, 1991.
- [27] F. Malek, “The Analytical Design of a Folded Waveguide Traveling Wave Tube and Small Signal Gain Analysis Using Madey’s Theorem”, *Progress In Electromagnetics Research*, vol. 98, pp. 137–162, 2009. DOI: [10.2528/PIER09092604](https://doi.org/10.2528/PIER09092604).
- [28] D. J. Wales and J. P. K. Doye, “Global Optimization by Basin-Hopping and the Lowest Energy Structures of Lennard-Jones Clusters Containing up to 110 Atoms”, *The Journal of Physical Chemistry A*, vol. 101, no. 28, pp. 5111–5116, 1997.
- [29] J. H. Booske, M. C. Converse, C. L. Kory, C. T. Chevalier, D. A. Gallagher, K. E. Kreisler, V. O. Heinen, and S. Bhattacharjee, “Accurate Parametric Modeling of Folded Waveguide Circuits for Millimeter-Wave Traveling Wave Tubes”, *IEEE Trans. Electron Devices*, vol. 52, no. 5, pp. 685–694, 2005. DOI: [10.1109/TED.2005.845798](https://doi.org/10.1109/TED.2005.845798).
- [30] N. M. Ryskin and V. N. Titov, “Nonstationary Simulation of Electron Beam Interaction with Coupled Resonant Microwave Oscillators”, in *Proc. IEEE Int. Conf. Plasma Science (ICOPS)*, 2007, p. 725. DOI: [10.1109/PPPS.2007.4346031](https://doi.org/10.1109/PPPS.2007.4346031).
- [31] S. Meyne, P. Birtel, and A. F. Jacob, “Nose-Cone Loaded Folded-Waveguide Delay Lines for Q-Band Traveling-Wave Tubes”, in *Proc. German Microwave Conf. (GeMiC)*, Bochum, Germany, 2016.

## Bibliography

- [32] S. Meyne, P. Birtel, and A. F. Jacob, “Design, Fabrication, and Measurement of Nose-Cone Loaded Folded-Waveguide Delay Line in Q-Band”, in *Proc. IEEE Int. Vacuum Electronics Conf. (IVEC)*, 2016, pp. 1–2. DOI: [10.1109/IVEC.2015.7223780](https://doi.org/10.1109/IVEC.2015.7223780).
- [33] A. Horsley and A. Pearson, “Measurement of Dispersion and Interaction Impedance Characteristics of Slow-Wave Structures by Resonance Methods”, *IEEE Trans. Electron Devices*, vol. ED-13, no. 12, pp. 962–969, 1966. DOI: [10.1109/T-ED.1966.15876](https://doi.org/10.1109/T-ED.1966.15876).
- [34] N. Meyne, S. Latus, and A. F. Jacob, “Corrugated Coplanar Transmission-Line Sensor for Broadband Liquid Sample Characterization”, in *Proc. German Microwave Conf. (GeMiC)*, 2014, pp. 1–4.
- [35] R. B. Marks and D. F. Williams, “A General Waveguide Circuit Theory”, *Journal of Research - National Institute of Standards and Technology*, vol. 97, pp. 533–533, 1992.
- [36] S. Meyne, J.-F. David, and A. F. Jacob, “Cold and Hot Matching of Coupled-Cavity Traveling-Wave Tubes”, in *Proc. German Microwave Conf. (GeMiC)*, 2014, pp. 1–4.
- [37] S. Meyne, J.-F. David, and A. F. Jacob, “Hot Matching Conditions of Coupled-Cavity Traveling-Wave Tubes”, in *Proc. IEEE Int. Vacuum Electronics Conf. (IVEC)*, 2014, pp. 15–16. DOI: [10.1109/IVEC.2014.6857467](https://doi.org/10.1109/IVEC.2014.6857467).
- [38] S. O. Wallander, “Reflexions and Gain Ripple in TWT’s”, *IEEE Trans. Electron Devices*, vol. 19, no. 5, pp. 655–660, 1972. DOI: [10.1109/T-ED.1972.17469](https://doi.org/10.1109/T-ED.1972.17469).
- [39] T. M. Antonsen, D. P. Chernin, S. J. Cooke, and B. Levush, “Spurious Reflection of Space Charge Fields in TWTAs”, *IEEE Trans. Electron Devices*, vol. 52, no. 5, pp. 755–763, 2005. DOI: [10.1109/TED.2005.845869](https://doi.org/10.1109/TED.2005.845869).
- [40] S. Meyne, J.-F. David, and A. F. Jacob, “Large-Signal Investigation of Cold and Hot Matched Coupled-Cavity Traveling-Wave Tubes”, *Frequenz. Journal of RF-Engineering and Telecommunications*, vol. 69, no. 1-2, pp. 3–10, 2014. DOI: [10.1515/freq-2014-0118](https://doi.org/10.1515/freq-2014-0118).
- [41] D. M. H. Hung, I. M. Rittersdorf, P. Zhang, D. Chernin, Y. Y. Lau, T. M. Antonsen, J. W. Luginsland, D. H. Simon, and R. M. Gilgenbach, “Absolute Instability near the Band Edge of Traveling-Wave Amplifiers”, *Phys. Rev. Lett.*, vol. 115, no. 12, p. 124 801, 2015. DOI: [10.1103/PhysRevLett.115.124801](https://doi.org/10.1103/PhysRevLett.115.124801).
- [42] D. Safi, “Design and Interaction Simulation of Folded-Waveguide Traveling-Wave Tubes”, Master’s Thesis, Technische Universität Hamburg-Harburg, 2015.

## Bibliography

- [43] S. Meyne, D. Safi, and A. F. Jacob, “Design Procedure for Hot-Matched Severs in Folded-Waveguide Traveling-Wave Tubes”, in *Proc. German Microwave Conf. (GeMiC)*, Bochum, Germany, 2016.
- [44] J. E. Dennis Jr. and R. B. Schnabel, *Numerical Methods for Unconstrained Optimization and Nonlinear Equations*. Society for Industrial & Applied Math, 1996.
- [45] C. G. Broyden, “A Class of Methods for Solving Nonlinear Simultaneous Equations”, *Mathematics of Computation*, vol. 19, no. 92, pp. 577–593, 1965.
- [46] J. M. Martínez, “Practical Quasi-Newton Methods for Solving Nonlinear Systems”, *Journal of Computational and Applied Mathematics*, vol. 124, no. 1, 2000, Numerical Analysis 2000, Vol. IV: Optimization and Nonlinear Equations. DOI: [http://dx.doi.org/10.1016/S0377-0427\(00\)00434-9](http://dx.doi.org/10.1016/S0377-0427(00)00434-9).
- [47] T. M. Antonsen, P. Saifer, D. P. Chernin, and B. Levush, “Stability of Traveling-Wave Amplifiers with Reflections”, *IEEE Trans. Plasma Sci.*, vol. 30, no. 3, pp. 1089–1107, 2002. DOI: [10.1109/TPS.2002.801563](https://doi.org/10.1109/TPS.2002.801563).
- [48] D. P. Chernin, T. M. Antonsen, I. A. Chernyavskiy, A. N. Vlasov, B. Levush, R. Begum, and J. R. Legarra, “Large-Signal Multifrequency Simulation of Coupled-Cavity TWTs”, *IEEE Trans. Electron Devices*, vol. 58, no. 4, pp. 1229–1240, 2011. DOI: [10.1109/TED.2011.2106504](https://doi.org/10.1109/TED.2011.2106504).
- [49] A. N. Vlasov, T. M. Antonsen, I. A. Chernyavskiy, D. P. Chernin, and B. Levush, “A Computationally Efficient Two-Dimensional Model of the Beam-Wave Interaction in a Coupled-Cavity TWT”, *IEEE Trans. Plasma Sci.*, vol. 40, no. 6, pp. 1575–1589, 2012. DOI: [10.1109/TPS.2012.2188547](https://doi.org/10.1109/TPS.2012.2188547).
- [50] A. N. Vlasov, I. A. Chernyavskiy, C. D. Joye, A. M. Cook, J. P. Calame, B. Levush, D. Chernin, T. M. Antonsen, and K. T. Nguyen, “Modeling of the NRL G-Band TWT Amplifier Using the CHRISTINE and TESLA Simulation Codes”, in *Proc. IEEE Int. Vacuum Electronics Conf. (IVEC)*, 2013, pp. 1–2. DOI: [10.1109/IVEC.2013.6571086](https://doi.org/10.1109/IVEC.2013.6571086).
- [51] S. Meyne, P. Birtel, and A. F. Jacob, “Q-Band High-Power Traveling-Wave Tube with Optimized Folded-Waveguide Delay Line”, in *Proc. IEEE Int. Vacuum Electronics Conf. (IVEC)*, 2015, pp. 1–2. DOI: [10.1109/IVEC.2015.7223780](https://doi.org/10.1109/IVEC.2015.7223780).
- [52] M. Krenz, “Taper-Optimization of a Helix Traveling-Wave Tube using Adaptive Simulated Annealing”, Bachelor’s Thesis, Technische Universität Hamburg-Harburg, 2013.
- [53] P. Waller, “Modélisation Numérique de l’Interaction et Diagnostic Expérimental du Faisceau d’Électrons dans un Tube à Ondes Progressives Spatial”, PhD thesis, Université Paris 7, 1999.

## *Bibliography*

- [54] P. Birtel, “Inclusion of Multi-Reflections in the Beam-Wave Interaction Simulation of Traveling Wave Tubes”, PhD thesis, Technische Universität Hamburg-Harburg, 2011.

# Lebenslauf

<b>Name</b>	Meyne
<b>Vorname</b>	Sascha
<b>Geburtsdatum</b>	30.08.1985
<b>Geburtsort, -land</b>	Dannenberg (Elbe), Deutschland
08.1992 - 07.1996	Grundschule Hitzacker in Hitzacker
08.1996 - 07.1998	Bernhard-Varenius-Schule in Hitzacker
08.1998 - 07.2005	Fritz-Reuter-Gymnasium in Dannenberg (Elbe)
07.2005 - 03.2006	Zivildienst bei der Häuslichen Krankenpflege Riedel & Klappstein in Dannenberg (Elbe)
04.2006 - 07.2006	Geringfügig Beschäftigter bei der Häuslichen Krankenpflege Riedel & Klappstein in Dannenberg (Elbe)
10.2006 - 05.2012	Studium an der Technischen Universität Hamburg-Harburg in Hamburg Abschluss: Diplom-Ingenieur
06.2012	Wissenschaftlicher Mitarbeiter an der Technischen Universität Hamburg-Harburg in Hamburg
07.2012 - 09.2012	Entwicklungsingenieur bei Thales Electronic Systems GmbH in Ulm
10.2012 - heute	Wissenschaftlicher Mitarbeiter an der Technischen Universität Hamburg-Harburg in Hamburg